DWARF GALAXY ACCRETION IN THE MILKY WAY: VIEWING DWARF GALAXY ACCRETION THROUGH THE EYES OF LARGE SURVEYS

Christian Rochford Hayes
Kokomo, Indiana

B.S. Astronomy/Astrophysics, Indiana University, 2015

B.S. Physics, Indiana University, 2015

M.S. Astronomy, University of Virginia, 2017

A Dissertation Presented to the Graduate
Faculty of the University of Virginia
in Candidacy for the Degree of
Doctor of Philosophy

Department of Astronomy

University of Virginia
May 2020

Committee Members:

Steven R. Majewski
Nitya J. Kallivayalil
Philip L. Arras
David A. Nichols

Abstract

Large spectroscopic and astrometric surveys, such as APOGEE and *Gaia*, provide us with large multi-dimensional data sets that allow us to study the Milky Way and its system of satellite dwarf galaxies in unprecedented detail. Among their many applications, these new tools afford us potent means by which to look for evidence of the accretion of dwarf galaxies, because the latter are well known to evolve in ways that imprint unique chemical and kinematical signatures in the stars that they contribute to the Milky Way when these satellites are accreted into the Milky Way halo. In this dissertation we report the discovery of a significant accreted population of stars exhibiting unique chemistry (particularly in C+N, Mg, Al, and Ni) and kinematics as probed by APOGEE, a system that is now known as the Gaia-Sausage or Gaia-Enceladus. We detail how this accreted system differentiates itself from the *in situ* population of Milky Way stars at similarly low metallicities that appears to be related to the Milky Way's thick disk. We also show how the chemical abundance profile of this accreted population suggests that it came from a relatively massive dwarf galaxy progenitor, with a size roughly between that of the Small and Large Magellanic Clouds. We also report that the Triangulum-Andromeda Overdensity, a feature in the outskirts of the Milky Way and long debated to be either a tidal stream or a feature of the Galaxy's outer disk, has multi-element chemical abundance patterns consistent with disk origin. TriAnd may have been perturbed out of the disk midplane due to the passage of a dwarf galaxy, possibly Sagittarius. The Sagittarius dwarf galaxy itself, provides a unique laboratory for studying hierarchical mergers, because its accretion is still ongoing and its stellar debris has yet to phase mix throughout the Milky Way halo. We exploit these properties for two separate investigations. First we use the Sagittarius tidal stream to measure the reflex motion of the sun

in a wholly unique way from previous methods, by kinematically identifying the Sagittarius trailing arm in *Gaia* DR2 and comparing its observed proper motion with the most sophisticated models of the Sagittarius stream to constrain the effect of the sun's motion. We also develop a new 6D, positional and kinematical method for tracing the Sagittarius stream according to its motion in its orbital plane. Using APOGEE's precise chemical abundances, we then undertake the most comprehensive survey of abundance gradients along the Sagittarius stream and show how these can be used to reconstruct the metallicity and abundance gradients within the Sagittarius progenitor galaxy. Through these four investigations we demonstrate how modern, large astronomical surveys are opening new windows to the Galaxy's cannibalistic history, making it possible to understand in even greater detail the effects of dwarf galaxy accretion on both their host galaxy and the evolution from satellite to tidally dissolved halo substructure.

Acknowledgements

"I'm honestly surprised I made it this far."

- David Bordenave

First of all, Mom, Dad, Matt, Cory, you all have no idea how much your support has helped along my way through grad school, I really appreciate everything you have done, and this short amount of space is far too little to acknowledge it all. Mom and Dad, you have always been willing to give support and advice, and it has always been reassuring to know that you are supporting me and believe in me. Matt, I've loved sharing the late night calls, music, show, and book recommendations, complaining and commiserating about our similarly stressful grad school experiences. Traveling with the three of you is such an amazing experience and it's left me with so many fond memories, I love connecting with you all and sharing in new experiences. I hope we will have many more trips to come! Cory, I can't thank you enough for the calls and chats when I really should have been at home relaxing instead of working. It's always nice to be thought of and take a mental break from my usual world to talk with you about each of our jobs, day-to-day lives, and futures, even if I don't show it nearly as often as I should. To the whole gang, Matt, Cory, Nathan, Erik, Kerry, Andrew, I love you guys, hopping online and gaming with you all is some of the most fun I have!

David and Bruce, thanks for keeping me sane and giving me many laughs, it's been great to have great friends to shoot the breeze with and share a grad school experience. Robby, it's been fun to room together, kill time, and have someone to bounce ideas off of, whether that its how to predict abundances for exoplanet hosts or how successful of a basketball player you could be if you were 10 feet tall, you definitely know how to keep it exciting. Thanks to all of the Nelly's (semi-)regulars these past few years, Bruce, David, Robby, Yiqing, Mengyao, Caroline, I've enjoyed relaxing and chatting with you all over a beer on a pseudo-weekly frequency. I'm also appreciative of the advice and guidance some of my more "senior" grad students have given during my time here at UVA, so thanks Sandy, Guillermo, and Nick there's no doubt that you helped my early years go smoother than they could have! Though there are too many to name everyone individually, thanks to the rest of my fellow grad students and those in my cohort for the support and camaraderie while I've been here at UVA. Many of my fellow DSBK volunteers are already listed here in one way or another, but thanks to the whole DSBK crew, I've learned so much by working with you all (and had a really fun time along the way); you certainly have improved my grad school experience (and many of my public speaking and organizational skills)!

Of course, many thanks go to my advisor, Steve, who has supported me in a number of ways throughout my years here. I appreciate the independence you've let me have in working on research projects and following my fancy ever since my first year when I eagerly dove into APOGEE data, and never turned back. I've also loved working with you and having the privilege of your encyclopedic knowledge and exceptional intuition from years research. I'm also grateful for your encouragement to become more involved with the APOGEE team and meet/work with your collaborators. You've also been very patient with my slow and repetitive writing style, and always provided useful comments and edits through many revisions. While my writing style may still be wordy, working with you has certainly made me better at forming and supporting my arguments through writing (and particularly at identifying why my readers should care about what I'm saying).

I also appreciate all of the help from my great collaborators, who it has been a pleasure to work with, Sten, Rachael, David, Borja, Matthew, Katia, Verne, Felipe, Diane, Jen and the whole APOGEE team. I have learned a lot from you all and have enjoyed your insights, ideas, and company. I also want to thank my committee for their time. Thanks to the ladies in the front office here at UVA, Whitney, Jackie, and Barbara, especially for answering all of my dumb questions and helping solve any of my bureaucratic problems when I ran across them. There are countless others who have helped me get to where I am today, and although I don't have the space to mention you all, I appreciate everything you've done!

I want to conclude by thanking you, reader, for your interest in my work (no matter how big or small), and for your daring to crack this open and meander through my thoughts and writings from the past five years. Since this is the last thing I have had to write for this dissertation, I am beyond tired of writing it, and will leave you to enjoy (or perhaps just experience) this, the sum of my Ph.D. work.

Table of contents

List of Figures

List of Tables

Chapter 1

Introduction

1.1 Background

1.1.1 The Accretion of Dwarf Galaxies in the Milky Way: Historical Context

Galactic archaeology is the study of our galaxy, the Milky Way (MW), by using it's stars and stellar populations as a record of the Galaxy's past, so that, by examining how the MW appears to us today, we can piece together its history. This helps us answer one of the key questions in modern astronomy: how do galaxies form and evolve.

Studies of the MW have long attempted to divide stars into a variety of structures and stellar populations assumed to share a common history and origin, but the formation and evolution of the MW's constituent components has been a long, complex process, so these assumptions may not be true, since many of the details of the MW's formation and evolution have yet to be resolved. For example, one of the early debates about the MW's formation was between the ideas posed by Eggen et al. (1962)

and Searle & Zinn (1978). Eggen et al. (1962) suggested that the formation mechanism of the MW was via the monolithic "collapse" of a large protogalactic cloud of star forming gas that during the collapse would leave behind stars on eccentric orbits in the MW halo before the gas settled and spun up into a disk. This grand and "organized" collapse model was challenged by the idea put forth by Searle & Zinn (1978) who argued that at least some parts of the halo of the MW formed through the protracted accumulation of "proto-galactic fragments." The latter picture, now referred to as the hierarchical model through minor mergers of dwarf galaxies, is now regarded as the accepted scenario for the growth of various parts of larger galaxies like the MW.

Through more observations and study (reviewed in depth by Gilmore et al. 1989; Majewski 1993b) it became apparent, that in reality, a combination of these processes proffered by Eggen et al. (1962) and Searle & Zinn (1978) likely occurred to form the MW as we see it today, and in modern discussions, this concept has evolved to become a question of how much of the halo was formed *in situ* via a process like ELS versus how much has been accreted. Because major mergers would disrupt the MW's kinematically cold disk and the age of the MW's disk is known to be $\sim 10 - 12$ Gyr, it is generally acknowledged that major mergers have not significantly contributed to the recent growth of the MW (e.g., Toth & Ostriker 1992), and instead, *minor* mergers were key to the MW's later evolution. The concept of accreting dwarf galaxies as a way to grow the MW or its halo spawned several studies of the MW halo and a search for evidence of the accretion of such systems.

Stars were found moving on retrograde orbits or in moving groups in the MW halo (e.g., Innanen & House 1970; Sommer-Larsen & Zhen 1990; Allen et al. 1991; Majewski 1992; Kinman et al. 1994; Majewski et al. 1994b; Norris 1994), which are relatively unlikely to have formed in the MW due to angular momentum conservation arguments, and therefore suggested that some of the material in the MW halo has been accreted. Supporting this idea were spatio-kinematical findings that the MW halo is not fully phase mixed, and is instead littered with substructure, inconsistent with expectations for a smooth phase-space distribution indicative of a classical halo (Majewski et al. 1996; Vivas et al. 2001; Gilmore et al. 2002). However, the 1994 discovery of the Sagittarius dwarf spheroidal galaxy (Sgr dSph), a large and luminous system, rivaling that of the Fornax dSph in mass and at only about 16 kpc from the Galactic center (Ibata et al. 1994), opened up new avenue for studying accreting systems.

Because of it's large size and proximity to the MW, Sgr was immediately understood as a candidate minor merger system that should show strong tidal features (Ibata et al. 1994; Johnston et al. 1999a,b; Ibata et al. 2000). If found, it's tidal streams would provide an example of active accretion into the MW halo, and an opportunity to understand better the evolution of a star system that has populated and will continue to populate the halo with stellar tidal debris in the future. After the concerted efforts of early probes to identify the "Sgr stream" (Mateo et al. 1998; Martínez-Delgado et al. 2001; Vivas et al. 2001; Dinescu et al. 2002), as predicted, the Sgr system was proven to be tidally disrupting. Following these initial probes of the Sgr stream, its full extent was revealed by large area photometric surveys, such as the Sloan Digital Sky Survey (SDSS) and the Two Micron All Sky Survey (2MASS), which showed that the Sgr system has produced a prominent tidal stream that extends completely around the MW with the leading and trailing arms each covering $> 180°$ (Ivezić et al. 2000; Newberg et al. 2002; Majewski et al. 2003).

In addition to mapping the Sgr stream, large area photometric surveys like SDSS and 2MASS also led to a flood of discoveries of tidal streams and other assorted stellar overdensities in the halo and outer disk of the MW (see Grillmair & Carlin 2016, for a summary of known streams/overdensities and their means of discovery as of a few years ago). Like Sgr itself, some of the strikingly coherent and cold streams have been connected to progenitors, such as the globular clusters Pal 5 or NGC 5466 (Odenkirchen et al. 2001; Belokurov et al. 2006), whereas the progenitor systems of other streams like the Orphan, GD-1, AntiCenter Stream, etc. (Grillmair 2006a,b; Grillmair & Dionatos 2006; Grillmair 2009) are still unknown. Even less understood are various broad ring- or cloud-like overdensities seen covering large areas of the MW halo, both at high latitudes as well as around the outer disk, which had neither a coherent stream-like distribution nor an identifiable progenitor. These systems include the Virgo Overdensity, Monoceros Ring, Triangulum-Andromeda overdensity (TriAnd) and Eastern Banded Structure (Vivas et al. 2001; Newberg et al. 2002; Ibata et al. 2003; Majewski et al. 2004; Rocha-Pinto et al. 2004; Grillmair 2006b).

This list of identified "halo overdensities" is ever expanding as deeper and more comprehensive photometric surveys and analysis techniques become available (e.g., Sharma et al. 2010; Li et al. 2017; Shipp et al. 2018; Ibata et al. 2019a), and vividly illustrate that the MW halo is a complex system. Indeed, the preponderance of such substructure is beginning to suggest that the halo is more a collection of kinematical substructures than a coherent structure of its own. Moreover, the identified coherent streams and overdensities represent more recent accretion, and do not even account for the more phase-mixed, older accretion events experienced by the halo.

While the early study of the MW halo and its accretion history was deeply rooted in spatial and kinematical studies, over the past decade or so, technology has made it possible to complement such work with chemical abundance analyses. Chemistry provides a powerful dimension to the exploration of the halo's accretion history, because the chemistry of individual dwarf galaxies tend to be distinct from both the MW as well as each other due to their slow chemical enrichment and stochastic star formation (Wyse & Gilmore 1993; Unavane et al. 1996). Thus chemistry could be used to uncover which constituent populations of the MW could have been accreted, even if such accretion occurred far in the past. Even while typically coming from modest samples of dozens of stars, stellar chemistry has provided a powerful tool to assess the presence of accreted populations. The origin of the MW's thick disk has been debated (and to some extent still is, e.g., Grisoni et al. 2018; Haywood et al. 2018; Mackereth et al. 2018, 2019b; Spitoni et al. 2019; Vincenzo et al. 2019), but several studies have concluded that the MW's thick disk is inconsistent with being accreted from dwarf galaxies on the basis of its chemical abundance patterns, which are indicative of a fast chemical evolution not seen in dwarf galaxies (Venn et al. 2004; Reddy et al. 2006; Ruchti et al. 2011). On the other hand, the halo appears to show chemical patterns distinct from those of the MW's thick disk, but similar to those of dSphs, providing evidence that some of the material in the MW halo has been accreted (Nissen & Schuster 1997, 2010, 2011; Navarro et al. 2011; Ishigaki et al. 2012, 2013; Ramírez et al. 2012; Sheffield et al. 2012; Jackson-Jones et al. 2014; Hawkins et al. 2015).

We now lie at an interesting point in time, where large area spectroscopic and astrometric surveys are available to provide us with statistically robust samples and new diagnostics to apply to the study of the origin and history of stars in both the smooth, phase-mixed halo as well as those in known halo substructures.

1.1.2 Setting the Stage: The State of the Field Prior to this Work

Despite the prior discovery of numerous examples of ongoing MW mergers, the accretion history of our Galaxy and how much this has contributed to the halo, is still uncertain and is only now beginning to be resolved. While the general dynamical processes involved in minor mergers have been long established (e.g., Johnston 1998), how tidal disruption may effect the detailed chemical and star formation histories of progenitors is still poorly understood. With the advent of large spectroscopic and astrometric surveys, it is now possible to obtain the data needed to begin investigating such questions through probes of tidal accretion in various evolutionary stages, e.g., from those that still have coherent spatio-kinematical structure, to those that phase-mixed billions of years ago.

In this dissertation, we take advantage of these novel data sets to begin investigating the MW halo and its accretion history, and specifically, we do this by shedding light on the following questions that have been highlighted by past studies of the MW and its halo.

How much of the MW halo was formed *in situ* versus accreted?

Because of the numerous examples of active accretion that we can see in the halo of the MW today (see Grillmair & Carlin 2016 for a summary of several examples), we know that the stars of the halo were not all formed *in situ*. However the degree to which accretion has contributed to the present-day stellar halo is not well understood, in part, because we don't know how much of the smoother, more phase-mixed halo itself was accreted. Chemical abundance patterns suggest that some of this material in the local halo has been accreted (Nissen & Schuster 1997, 2010, 2011; Navarro et al. 2011; Ramírez et al. 2012; Hawkins et al. 2015), but larger samples pushing to lower metallicities are needed to resolve this question better.

Is there a duality or bimodality in the MW halo?

Many studies over the years have concluded that the MW halo is bimodal with two overlapping structures of distinctly different age, shape, kinematics, chemistry, etc. These analyses find the need for dual "inner" and "outer" halos to explain the properties of field star populations (Hartwick 1987; Sommer-Larsen & Zhen 1990; Allen et al. 1991; Kinman et al. 1994; Norris 1994; Carollo et al. 2007, 2010; Beers et al. 2012; Ishigaki et al. 2012, 2013), or for "old" and "young" halos to explain the MW's globular cluster population (Zinn 1993, 1996; Leaman et al. 2013; VandenBerg et al. 2013; Wagner-Kaiser et al. 2017). In many cases, the analyses of field stars are based on local samples of presumed halo stars. Moreover, some of these claims of duality in the MW halo have been later refuted by critical assessment of potential selection biases or complications in utilized data sets (Gratton et al. 2010; Schönrich et al. 2011; Fermani & Schönrich 2013; Schönrich et al. 2014), making it still unclear whether this duality or bimodality is real, and, if it is, what the origin of each component might be. Some advocates of the dual halo hypothesis suggest that the properties of the outer halo more evidence for the accretion of systems into the MW halo. A potential question remains on how this dual halo structure might fit into the bigger picture of the accretion of multiple systems that is evidently still occurring?

What is the origin of the Galactic anticenter overdensities?

At moderate latitudes away from the MW midplane ($\sim 20-40°$) and large Galactocentric radii ($\sim 15-30$ kpc), several stellar overdensities in the Galactic anticenter have been identified at the boundary between the outer disk and halo. Most prominent among these are three structures that each cover a large area of the sky: the Monoceros Ring (both its northern and southern extensions; Newberg et al. 2002; Yanny et al. 2003), TriAnd (Majewski et al. 2004; Rocha-Pinto et al. 2004), and A13 (Sharma et al. 2010; Li et al. 2017). Because Monoceros and TriAnd were discovered at a time when many tidal streams were found in the MW halo, these structures were thought to be low-latitude tidal debris from dwarf galaxies (Rocha-Pinto et al. 2003; Peñarrubia et al. 2005; Chou et al. 2010, 2011; Sollima et al. 2011; Sheffield et al. 2014). However, growing evidence has led to a competing theory that perturbations to the MW disk from orbiting dwarf galaxies could excite density waves that produce vertical oscillations of the MW midplane at large Galactocentric radii, and that these overdensities are merely concentrations of stars at the crests or troughs of these ripple-like waves (Kazantzidis et al. 2008; Purcell et al. 2011; Gómez et al. 2013, 2016; Xu et al. 2015; Li et al. 2017; Newberg & Xu 2017; Laporte et al. 2018). In either case, these overdensities are related to the interaction of the MW with dwarf galaxies, but how remained to be firmly established.

What did the Sgr progenitor look like before its tidal disruption?

Because Sgr is in a relatively advanced state of its tidal disruption and accretion into the MW halo it's initial structure has been disrupted by it's physical transformation and so that its original properties, e.g., mass and original morphology, are no longer discernible. Adding to the complexity, is that Sgr actively formed stars at the same time that it was being disrupted by the MW. While modelling of the Sgr stream and core can reasonably reproduce the observed properties of both (Helmi 2004; Johnston et al. 2005; Law et al. 2005; Law & Majewski 2010), the models fail to match the dynamically oldest parts of the stream (Hernitschek et al. 2017; Sesar et al. 2017), nor do they strongly constrain the initial mass of the Sgr system, or the morphology of the progenitor (e.g., disk-like or spheroidal), as early studies had hoped (Łokas et al. 2010, 2012; Peñarrubia et al. 2010, 2011; Frinchaboy et al. 2012). Clearly more sophisticated modeling, including gas, stars, and dark matter of both Sgr and the MW, is needed to characterize this complex system. On the other hand, the chemical abundance patterns of Sgr have provided some compelling evidence about the Sgr progenitor, suggesting that it may have been relatively massive (of order the mass of the SMC or LMC; Chou et al. 2010; Gibbons et al. 2017; Mucciarelli et al. 2017; Carlin et al. 2018), and that it had substantial radial metallicity gradients (Law & Majewski 2010), since there are metallicity gradients measured along the Sgr stream (Chou et al. 2007; Keller et al. 2010; Carlin et al. 2012; Shi et al. 2012; Hyde et al. 2015). We are now in a position to understand better, both the kinematics and chemistry of the Sgr system, now that we have access to higher precision data, which can be used to inform and constrain future models of Sgr and help reconstruct its progenitor.

Now that large surveys and high quality positional, kinematical, dynamical and chemical data are becoming available, we can begin to answer many of these questions. Of course this dissertation does not exclusively or entirely answer all of these questions, but in the following chapters we present pieces of these answers by taking advantage of the exponentially growing tool set at hand.

1.2 Tools for Finding Accreting and Accreted Dwarf Galaxies

There are many ways that accreting and accreted dwarf galaxies can make their presence known, with appropriate detection techniques depending on the state of tidal disruption. Obviously, the most straightforward strategy has been to image them directly. After filtering with well defined physical tracers, some accretion substructures become evident as photometric overdensities (e.g., Ibata et al. 1994; Odenkirchen et al. 2001; Majewski et al. 2003; Belokurov et al. 2006; Grillmair 2006a,b; Grillmair & Dionatos 2006, etc.). Meanwhile, large area spectroscopic surveys can be used to identify coherent kinematical features that are signatures of tidal debris. In the case of systems that were accreted long ago, these detection mechanisms are not as effective, because tidal feature will tend to precess, phase-mix, and smear out the photometric and kinematic signatures of their tidal features, until only their dynamical signatures will cluster (such as orbital elements), otherwise blending in with the rest of the MW halo. The star formation and chemical evolution histories in dwarf galaxies are, however, distinct from those of the MW. So, stars from accreted dwarf galaxies can also be identified in the MW halo by their distinctly different chemical patterns, regardless of when they were accreted. Central to all of these methods of finding accretion signatures, is the need to sample large numbers of stars, so that the new era of large surveys has brought us invaluable new tools to undertake this task. The hope is that through systematic exploration of the MW halo to look for these signatures of such past or present accretion (photometric, kinematic, dynamic, and chemical) we can reconstruct the MW's accretion history and recover a census of the accreted entities.

1.2.1 Physical Tracers

As a dwarf galaxy falls into the MW, tidal forces will slowly elongate and strip stars off of the dwarf galaxy. This stripped material will, due to slight differences in orbital energy, stretch out into tidal tails that will grow longer as the smaller galaxy continues its orbit. This will produce an overdensity of stars on the sky, leading to the most obvious tracers of active accretion (i.e., tidal streams that we can see today; see Grillmair & Carlin 2016, for an overview of the detection of several known streams). In addition to their telltale leading/trailing arm distribution, the stars stripped from a dwarf galaxy will continue to move along the orbit of the core of the galaxy, so they can be found kinematically as kinematically cold substructure in the distribution of halo stars. The fact that tidal streams are kinematically cold not only allows us to detect the existence of a stream but to identify individual stellar members whose properties (e.g., age or chemistry) provide additional information on the stream and it's progenitor system.

Unfortunately, distant systems in the halo typically have small proper motions, which require high precision astrometry to measure. Therefore, most kinematical studies of tidal streams have relied on radial velocities to identify members and characterize streams and other overdensities (Crane et al. 2003; Rocha-Pinto et al. 2004; Chou et al. 2007; Belokurov et al. 2014; Sheffield et al. 2014; Price-Whelan et al. 2015), given the relative ease of measuring the radial velocities of even distant stars. While a few studies have employed proper motions for a more holistic 6D measure of the positions and kinematics of relatively nearby systems (e.g., Koposov et al. 2010, 2013; Carlin et al. 2012; Sheffield et al. 2014), this is only now becoming prevalent with the availability of *Gaia* products through its most recent data release (DR2, Gaia Collaboration et al. 2016, 2018a).

The April 2018 release of *Gaia* DR2 revolutionized the use of kinematical and dynamical studies of the MW, because it provided the first high precision and homogeneous measurements of the proper motions and parallaxes (among other measurements) for 1.3 billion stars. *Gaia* DR2 is effectively complete to a *Gaia* G band magnitude of 17, with uncertainties of about 0.2 mas yr^{-1} in proper motion and about 0.1 mas in parallax at the faint end of its sample completeness. The unprecedented precision of *Gaia* DR2's proper motions alone open a great potential to study the kinematics of the MW halo. As examples: (1) Chapter 4 shows how the precise proper motions from *Gaia* DR2 can be used to clearly identify the Sgr stream in the MW halo and trace the changing direction of its motion at different points on the sky, (2) Fritz et al. (2018), Gaia Collaboration et al. (2018b), Kallivayalil et al. (2018), Zivick et al. (2019), and others show how these exquisite proper motions can clearly map the net proper motion of more distant dwarf galaxies around the MW, as well as the internal motion of the LMC and SMC, and (3) van der Marel et al. (2019) demonstrates that *Gaia* DR2 proper motions can even be used to probe the net and internal motions of M31 and M33 galaxies several hundred kiloparsecs away.

The parallaxes from *Gaia* DR2 can be used to measure distances to stars in general, although accurate and reliable distances can only be measured from parallaxes with relative uncertainties below $\sim 20\%$ (Lutz & Kelker 1973; Luri et al. 2018). For brighter stars in *Gaia* DR2 ($G < 15$), where *Gaia* measures its most precise parallaxes, this means it can provide distances out to $\sim 3 - 5$ kpc at its farthest, therefore, at present, *Gaia* can only provide distances to halo stars passing through the solar neighborhood and does not provide a good probe of more distant sources.

These distances have allowed for some exploration of the 6D phase space distribution of inner halo stars (e.g., Helmi et al. 2018). However by combining *Gaia* proper motions with photometric or spectrophotometric distances (such as the `StarHorse` distances; Santiago et al. 2016; Queiroz et al. 2018, 2020; Anders et al. 2019), these 6D phase space measurements can be pushed out to larger distances and probe the kinematics, dynamics and distributions of halo and stream stars in the outer halo (see Chapter 5 for example). Going a step further, many studies are now merging these 6D phase space distributions with chemical abundances measurements to uncover a wealth of new information about the MW's halo, broadening our understanding of its accretion history (Chapter 5; Belokurov et al. 2018; Myeong et al. 2018, 2019; Kruijssen et al. 2019; Mackereth et al. 2019a).

1.2.2 Chemical Tracers

As an alternative and a complement to spatiokinematical data, the chemistry of stars, i.e., their elemental abundances, has long been argued as a way to "tag" stars of a common origin[1]. This technique has previously been applied to identification of distinct populations in the Milky Way (e.g., clarifying the chemical distinctions between the high-alpha/low-alpha populations also referred to as the thick/thin disk; Reddy et al. 2003, 2006; Bensby et al. 2005; Bensby, Feltzing, & Oey 2014; Nidever et al. 2014; Hayden et al. 2015; Weinberg et al. 2019, etc.). But, as discussed below, this concept can be used to distinguish stars born in dwarf galaxies, from those born in the Milky Way, because these systems have different star formation histories, and therefore, different chemical evolution. These differences are recorded in the chemical composition of the stars born in those systems.

The two nucleosynthetic families most commonly used and referenced in stellar

[1]Here we appeal to the so-called "weak" form of chemical tagging, that argues that general populations of stars can be tagged via their similar or coherent chemical abundance patterns, rather than the "strong" form of chemical tagging that attempts to tag stars to their birth star clusters or associations.

chemical studies are the α-elements (O, Ne, Mg, Si, S, Ar, Ca, Ti), which are formed by successive additions of He nuclei or α-particles, as the main fusion mechanism in stars post-hydrogen and helium burning, and the Fe-peak elements (Sc, V, Cr, Mn, Fe, Co, Ni), a clustering of elements around Fe, the element with the highest binding energy and the last element that can produce energy through fusion. These two families of elements are primarily produced and distributed into the interstellar medium (ISM) via different kinds of supernovae (SNe), Type II (or core-collapse SNe), and Type Ia. Type II SNe, the end state of massive stars ($\gtrsim 8$ $M_\odot$), mostly produce α-elements with smaller amounts of Fe-peak elements. Type Ia SNe, on the other hand, almost exclusively produce Fe-peak elements, and are the thermonuclear detonation of a white dwarf (WD) growing past the Chandrasekhar limit (~ 1.4 $M_\odot$), either by accreting material from a companion (the single degenerate pathway) or by merging with another WD (the double degenerate pathway).

The real power of chemical abundance studies lies in the differing time scales for the occurrence of these SNe, and therefore the differing time scales for the production of their differing nucleosynthetic products. Massive stars have lifetimes on the order of 1 Myr (depending on the mass of the progenitor), whereas the canonical time delay for the production of WDs and subsequent Type Ia SNe is about 1 Gyr (although this is a vast oversimplification of a still very active field of research; Maoz 2010; Maoz et al. 2012; Graur et al. 2011; Howell 2011; Meng & Yang 2012; Walcher et al. 2016; Liu & Stancliffe 2018; Heringer et al. 2019). Thus, when a galaxy first begins forming stars, the most massive will die off as Type II SNe that pollute the galaxy's relatively pristine gas with metals that have a Type II SN α-to-Fe abundance ratio.

This abundance ratio is typically denoted in "bracket notation[2]" as [α/Fe], where

$$[\alpha/\mathrm{Fe}]_* \equiv \log_{10}\left(\frac{\mathrm{N}_\alpha}{\mathrm{N}_{\mathrm{Fe}}}\right)_* - \log_{10}\left(\frac{\mathrm{N}_\alpha}{\mathrm{N}_{\mathrm{Fe}}}\right)_\odot$$

where N_α is the number of α-element atoms, and N_{Fe} is the number of Fe atoms (Fe is used as a typical tracer of Fe-peak elements due to the historical ease of its measurement in the optical spectra of stars). These fractions are then normalized to the same fraction in the sun.

The [α/Fe] abundance ratios of the earliest populations of stars in a galaxy will, therefore, match roughly the [α/Fe] of Type II SNe yields, while the total metallicity (i.e., the total amount of elements heavier than H and He) of newly formed stars will increase because more metals (all elements heavier than H and He) are always being produced. Once enough time has gone by for WDs to form from the first generations of stars, the first Type Ia SNe can form and pollute the gas in the galaxy with Fe-peak-rich products that lower the [α/Fe] abundance ratio in future generations of stars (while of course continuing to enrich the metallicity of the galaxy. Figure 1.1 (adopted from Wyse 2016) illustrates a schematic of how this [α/Fe]-[Fe/H] chemical abundance pattern might look in today in three different example galaxies[3] (denoted by the curves marked with circles, boxes, or starbursts, respectively).

One notable feature across each of these three curves is the break or change in slope, referred to as the "α-knee", which corresponds to the metallicity that a galaxy

[2]This notation can also be used with an arbitrary set of elements, e.g., [Fe/H] which is typically used as a measure of the metallicity of a star, or [X/Fe] to report the abundance of an arbitrary element X with respect to Fe.

[3]We do not go in to more detail about the starburst marked curve in this chapter, which shows the effect of having a "top-heavy" initial mass function (IMF) on the chemical abundance pattern of a galaxy. This type of IMF will raise the [α/Fe] plateau of the galaxy because Type II SNe have a mass dependent [α/Fe] yield. This third example provides another way in which we can learn even more about a system from its chemical abundance pattern.

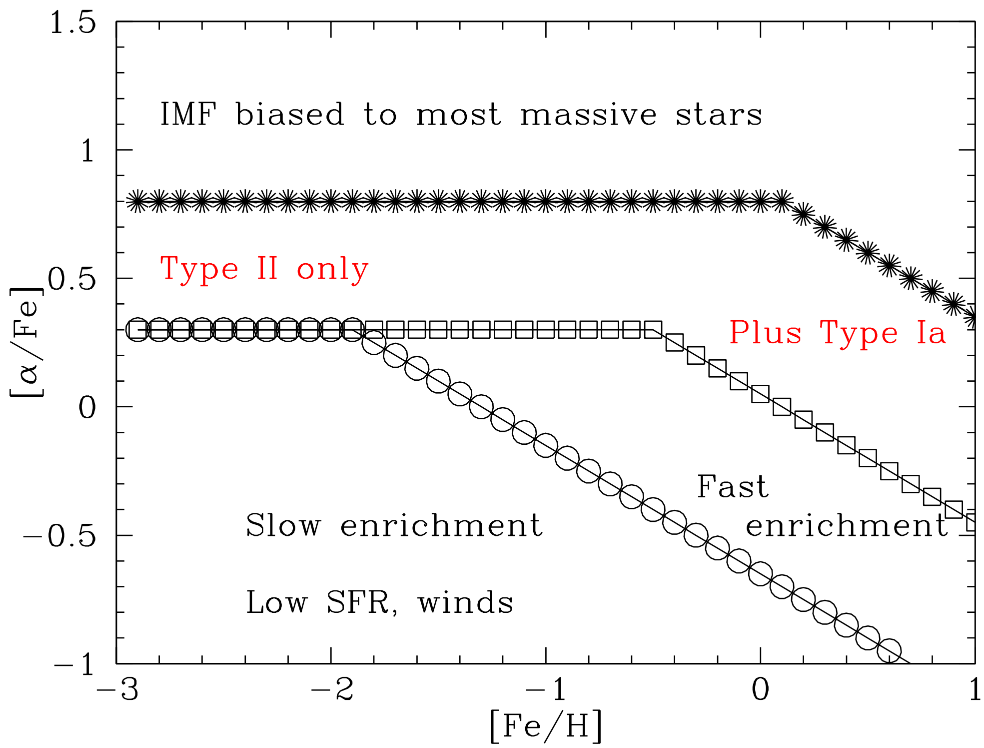

Fig. 1.1.— A schematic (adopted from Figure 2 of Wyse 2016) of the [α/Fe] vs. [Fe/H] chemical abundance pattern for three example galaxies. These three examples illustrate the mean chemical abundance pattern of a galaxy with (1) a fast chemical enrichment due to a high SFR, as would be expected of a MW-like galaxy (curve marked with boxes), (2) a slow chemical enrichment, due to a low SFR or on with significant gas outflows, like those expected in dwarf galaxies (circles), and (3) a "top-heavy" IMF, which raises the Type II SNe [α/Fe] plateau (starbursts). In all cases, evolution proceeds from left to right, and in each case the line-break or change in slopes, i.e., the α-knee, corresponds to the metallicity at which Type Ia SNe begin to occur and contribute Fe-peak rich gas back to the galaxy.

has reached by the time the first Type Ia SNe occur. The metallicity at which the α-knee occurs provides an important diagnostic of the "average" early star formation rate (SFR) in that galaxy, because it is a measure of how much SF and enrichment occurred before Type Ia SNe begin to significantly pollute the galaxy. Because the Type Ia SNe time delay is thought to be driven stellar evolution processes, this time delay will be the same across different galaxies (as seems to be the case across massive galaxies, Walcher et al. 2016), so that all galaxies will hit their α-knee at the same point *in time*. Therefore, the rate at which a galaxy forms stars, or more specifically, how many Type II SNe can pollute the galaxy within this constant time delay, will determine the metallicity of that galaxy's α-knee.

A galaxy with a high star formation rate (SFR) can enrich rapidly through the production of many high mass stars and reach a high metallicity before the first Type Ia SNe occur, like the toy model shown by the circled curve in Figure 1.1. This model is similar to a MW-mass galaxy. Lower-mass galaxies, such as dwarf galaxies, typically have lower SFRs due to their smaller gas reserves, and will create fewer Type II SNe and enrich less before Type Ia SNe are produced; thus, their α-knee will occur at lower metallicities, like that of the boxed curve in Figure 1.1.

Of course, this is a simplification of the chemical evolution of galaxies, and more realistic models may need to account for varying SFRs or SF efficiencies, gas inflows or outflows, mass and metallicity dependent SNe yields, inhomogeneous mixing of gas (producing intrinsic star-to-star scatter), or observational uncertainties, among other concerns. Figure 1.2 (left panel) shows more realistic chemical evolution models for a MW-mass galaxy and a dwarf galaxy, as calculated using the *flexCE* one zone chemical evolution code (Andrews et al. 2017), and what these chemical abundance patterns would look like when sampled by stars that have some intrinsic or extrinsic scatter

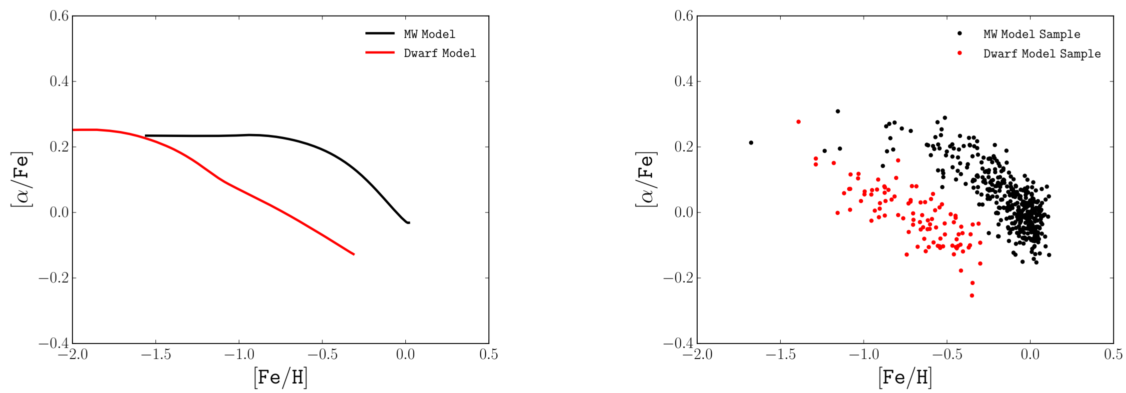

Fig. 1.2.— (Left) [α/Fe] versus [Fe/H] patterns of chemical evolution models calculated from the one-zone chemical evolution code *flexCE* (Andrews et al. 2017) for a MW-mass galaxy (black line) and a Sgr-like dwarf galaxy (red line), illustrating the effect of lower SFRs in dwarf galaxies compared to more massive ones (or more specifically a lower SF efficiency which has the effect of lowering the overall SFR). (Right) The [α/Fe] vs. [Fe/H] distribution of 400 mock "stars" sampled from the MW-mass chemical evolution model (black points) and 100 sampled from the dwarf galaxy chemical evolution model (red points). Both samples are drawn with a random metallicity and [α/Fe] scatter independently drawn from a normal distribution with a standard deviation of $\sigma = 0.05$ dex, to simulate an example of a combination of astrophysical variance and measurement uncertainties akin to those seen in modern spectroscopic surveys like APOGEE.

in their abundance measurements (right panel). In more realistic models like these, the α-knee is less well-defined, particularly when the chemical abundance patterns are sampled stochastically by modest samples of stars (in this case, mock "stars") drawing from the underlying chemical evolution track of the galaxy. However, even the dwarf galaxy model shown here with a relatively fast chemical enrichment rate for such a low mass system (one somewhat like the relatively massive Sgr dSph) can be clearly differentiated from a MW mass galaxy's chemical abundance pattern.

Even simple models like this suggest that we can use chemical abundances to identify stars that were born in dwarf galaxies from those that were born in the MW (Wyse & Gilmore 1993; Unavane et al. 1996). Moreover, the chemical abundances of stars remain essentially unchanged since their birth, so these unique chemical abundance patterns of dwarf galaxies can be traced even if the original galaxy is tidally disrupted and completely accreted into the MW. This "fossilized" information provides a way to trace past accretion events within the well-mixed field star population as well as those that are more visible as extant coherent structures.

Past studies have taken advantage of the chemical differences between the MW and dwarf galaxies to probe the present day metal-poor populations of the MW and identify which, if any, have been accreted. For example, chemical analyses have concluded that the MW's thick disk has abundance patterns inconsistent with those expected for a population accreted from dwarf galaxies (Venn et al. 2004; Reddy et al. 2006; Ruchti et al. 2011), whereas several studies have noted chemical peculiarities in the MW halo that may suggest the past accretion of one or more dwarf galaxies (Nissen & Schuster 1997, 2010, 2011; Navarro et al. 2011; Ishigaki et al. 2012, 2013; Ramírez et al. 2012; Sheffield et al. 2012; Jackson-Jones et al. 2014; Hawkins et al. 2015). However, to begin answering *how much* of the MW halo has been accreted, rather than *whether* any of it was accreted, we need to turn to surveys that can scan large, statistically significant samples of stars and that precisely measure their chemical abundances, preferably in an unbiased way (unlike earlier, smaller studies that were kinematically biased to pick out rare halo stars).

There are now several surveys dedicated to measuring stellar parameters and chemical abundances for hundreds of thousands to millions of stars in and around the MW, such as the Apache Point Observatory Galactic Evolution Experiment (APOGEE, Majewski et al. 2017), the Gaia-ESO Survey (Gilmore et al. 2012), Galactic Archaeology with HERMES (GALAH De Silva et al. 2015), or the Large sky Area Multi-Object fiber Spectroscopic Telescope survey (LAMOST, Zhao et al. 2012).

While results from some of these other surveys are referenced throughout this dissertation, the work here is based primarily on the APOGEE survey, a near infrared (H-band), high-resolution ($R \sim 22,500$) spectroscopic survey of the MW and nearby galaxies in the Local Group (such as the LMC, SMC, dSphs, and even integrated light observations of M31 and M33; Majewski et al. 2017; Zasowski et al. 2013, 2017; Beaton et al. in prep.; Santana et al. in prep.). With it's high-resolution spectra, APOGEE is able to measure precise stellar parameters, and chemical abundances for up to 26 different species, with an internal precision of 0.1 dex or less for several elements (Jönsson et al. in prep.). Another benefit of APOGEE is that, with its SDSS-IV expansion, APOGEE-2, it is an dual-hemisphere survey and its now $\sim$ 500,000 star sample (as of the sixteenth data release of the Sloan Digital Sky Survey, DR16; Ahumada et al. 2020) covers a wide range of Galactic environments, targeting the MW halo (where we have a greater chance of observing halo and stream stars serendipitously), disk, and even individual dwarf galaxies, each with a large sample of stars. APOGEE allows us to delve into both the local and more distant halo to chemically identify and study accreting or previously accreted systems.

1.3 Overview

The goal of the present work is to utilize the deep pool of data available in this age of large surveys to better understand the accretion of dwarf galaxies, their affect on the MW, and their importance in the MW's history and evolution, by studying past and ongoing accretion events. Specifically in this work we (1) search for and characterize past accretion that has helped populate the MW halo (Chapter 2), (2) use chemical analyses to classify an outer disk overdensity previously attributed to an accretion event as a feature of the MW disk and one that indicates that the MWs disk is dynamically perturbed, likely as the result of an interaction with one or more dwarf galaxies (Chapter 3), and (3) examine the present-day accretion of a dwarf galaxy, the Sgr dSph and it's tidal stream. By comparing models of the Sgr stream with new observations from *Gaia* DR2 we are able to make a new and independent measure of the motion of the sun through the MW (Chapters 4). Moreover, with these new *Gaia* proper motions we identify Sgr stream stars across the MW in the APOGEE sample and use dynamical models of the tidal disruption to reconstitute and reconstruct the chemical distribution of the Sgr system's progenitor galaxy (Chapter 5). Together these drive the exploration of the MW's accretion history, add to a dynamical backdrop of a reinvigorated discipline of Galactic astronomy and prompt new questions facing Galactic astronomy (as discussed in the concluding chapter, Chapter 6).

1.3.1 Dissecting the MW Halo

In Chapter 2 we use the stellar chemical abundance patterns provided by APOGEE to identify two significant and chemically distinct populations of low-metallicity stars ([Fe/H] $\lesssim -1$). These two populations are revealed primarily by their different [Mg/Fe] distributions as a function of [Fe/H] and can be relatively cleanly separated in this chemical plane. These two populations appear to be (1) an accreted population residing the Milky Way's inner halo, and (2) an *in situ* population that formed in the MW. In addition to differences in [Mg/Fe], these accreted and *in situ* populations also stand out in other elements probed by APOGEE, particularly in other alpha-elements (O, Si, and Ca), as well as C+N (a combination of light elements), Al (an odd-Z element), and Ni (an Fe-peak element). The accreted population follows halo-like kinematics (velocity dispersion dominated) and is likely what past studies have kinematically identified as the halo. The *in situ* population, in contrast, exhibits a net rotation of $\sim 120 - 150$ km/s, suggesting that it is not only an *in situ* population, but is also likely related to the MW's thick disk, and may be a puffed-up disk or flattened halo that preceded the formation of the thick disk. Examining the chemical abundance profile of the accreted halo population in detail, we find that it is similar to those of massive MW satellites, such as the Large Magellanic Cloud (LMC). This suggests that a (likely massive) dwarf galaxy with a similar star formation history to the early LMC was accreted in the MW's past, and now provides a significant fraction of stars in the inner halo of the MW.

1.3.2 The Origin of the Triangulum-Andromeda Overdensity

Chapter 3 explores the chemistry of the TriAnd overdensity, a stellar overdensity at the outskirts of the MW disk. TriAnd's origin had been previously debated; it was thought to be either (1) a tidal tail of a dwarf galaxy disrupting in or near the plane of the MW disk (Deason et al. 2014; Sheffield et al. 2014), or (2) a peak/trough of midplane oscillations of the MW disk excited by an orbiting dwarf galaxy satellite of the MW (Price-Whelan et al. 2015; Xu et al. 2015; Li et al. 2017). By comparing the chemistry of this system to that of Sgr dSph as well as the outer disk of the Milky Way (MW), we find that TriAnd stars are chemically distinct from Sgr, a prototypical dwarf galaxy of similar metallicity, across several elements. Instead, the TriAnd stars have chemistry similar to the low metallicity stars in the outer disk of the MW, and consistent with an extrapolation of their chemical and metallicity gradients to larger Galactocentric radii. These chemical perspectives suggest that the TriAnd overdensity is associated with the MW disk, and therefore that the disk extends out as far as $\sim$ 25 kpc, albeit perturbed to about 7 kpc below the nominal disk midplane and this radius. This vertical displacement supports a scenario wherein a dwarf galaxy, possibly Sgr itself, provides a repeated gravitational pull on the MW as it plunges past or through the disk, exciting density waves in the MW midplane that traverse across the disk to create overdensities such as TriAnd.

1.3.3 Probing Solar Motion with the Sagittarius Stream

We turn to the Sgr system itself in Chapter 4, one of the most dramatic examples of tidal disruption in the MW that is still on-going. Sgr is an example of a polar orbiting satellite and its debris, therefore, lies in a plane perpendicular to the Galactic plane. Serendipitously, the present-day location of the sun places it nearly at the intersection al line of nodes between these two planes across the sky. Because the Sgr system orbits in this plane with little to no motion perpendicular to it, we can measure the rotational velocity of the Sun around the MW recorded entirely in the reflex motion of the Sgr stream. We take advantage of this convenient orientation and use the best standing model of the Sgr stream to extract this reflex motion from new precise observations of the motion of the trailing arm of the Sgr streams provided by *Gaia* DR2. This gives us a measurement of the rotational velocity of the Sun around the MW in a way completely independent of other methods, which have different systematic errors, yet we find a result consistent with the latest attempts at other methods. As a corollary of this work, we identify a relatively pure sample of Sgr stream giants in the trailing arm of the stream, using a new method of isolating stream stars in the MW halo that inspires the more complete and complex Sgr stream selection methods showcased in Chapter 5, which can be performed with full 6D phase space distributions of MW halo and Sgr stream stars

1.3.4 Measuring Chemical Gradients along the Sagittarius Stream

Chapter 5 shows that with the large sample of precise 6D phase space distributions of halo stars *and* precise chemical abundances from high-resolution spectra, we can clearly identify Sgr stream stars in the MW halo, and use these stars to understand better the initial chemical structure of the the Sgr progenitor. By combining APOGEE with the high precision proper motions measured in *Gaia* DR2 and the spectrophotometric distances from StarHorse (Queiroz et al. 2018, 2020), we are able to trace the 3D spatial distribution and kinematics of the Sgr stream in APOGEE, finding 166 members. While many stars in the core of the Sgr dSph have been previously observed by APOGEE, these stars are most bound metal-rich remnants of the Sgr progenitor. On the other hand, the stars in the Sgr stream stars have been stripped from the outskirts of the original galaxy, and represent older, more metal-poor populations of the progenitor galaxy. We explore these stars to report both newly measured metallicity and chemical abundance gradients along the stream, which can be used to argue for the existence of prior radial gradients within the Sgr progenitor itself before it was tidally disrupted. This is now possible given the homogeneously analyzed and serendipitously observed sample of Sgr stream stars in APOGEE, and affords us an opporutunity to paint a more complete picture of the Sgr progenitor, and motivates the need for more sophisticated modeling of this system in the future.

1.3.5 The Progress and Future of the Field

The work presented in this dissertation, of course, does not live in a vacuum, and there are many results from other studies are presented throughout the following chapters. In Chapter 6 we summarize the findings of this dissertation and put the present body of work in context with other major developments in the field. Together, these provide a framework for new questions moving forward in the study of the MW's halo. Among the other results in parallel to those presented in this work, aimed at understanding the accreted halo of the Milky Way is the discovery that it may have been dominated by a single accretion event referred to as the Gaia Sausage or Gaia-Enceladus even (Belokurov et al. 2018; Helmi et al. 2018). Alongside these developments in our understanding of the MW halo, other studies concurrent to the research presented here have also concluded that TriAnd and another outer disk overdensity, A13, are chemically similar to the MW disk (Bergemann et al. 2018). These results in concert with simulations (e.g., Laporte et al. 2018) and local kinematic observations with *Gaia* DR2 (Antoja et al. 2018; Bland-Hawthorn et al. 2019) support the suggestion 3 that the MW disk has been perturbed, likely by the Sgr galaxy. Our work to map the chemistry of the Sgr stream adds to a greater developing is a full characterization of the kinematics (Yang et al. 2019; Antoja et al. 2020) and chemistry (Carlin et al. 2018; Hasselquist et al. 2019) of the Sgr stream that has been spurred on by the measurements of precise proper motions from *Gaia*, and the large field of view telescopes with high-resolution spectrographs surveying the MW halo.

1.3.6 Contributions

Each of the following chapters (excluding the concluding chapter, Chapter 6) is published as a peer-reviewed journal article (Chapters 2-5 are published in Hayes et al. 2018a,b,c, 2020, respectively), so that these results are publicly available. All of this research relies on large astronomical surveys to some extent, and as referenced throughout this work, there is a monumental contribution from many teams and dedicated individuals that make these surveys run and support the production of their results. In addition to these teams, this work has benefited from the advice, feedback, and assistance of other individuals represented in the author lists of each of these published article. For completeness, the author wishes to acknowledge credit where credit is due and clarify significant contributions from other persons to each of the following chapters.

As an advisor, Steven Majewski, has naturally promoted and supported the development of each of these chapters through continued guidance, feedback, and suggestions. Though innumerable, these contributions have undoubtedly helped shape the direction and message of the research presented in this body of work.

In addition to providing feedback on several manuscripts, and giving invaluable insight on the chemical abundance profiles of dwarf galaxies, Matthew Shetrone also provided an analysis of the detectability of elements at the lowest metallicities probed by APOGEE. This was particularly key to the discussion of Fe-peak elements in Section 2.3.2 that some of the Fe-peak elements (and to some extent, carbon) become undetectable with typical APOGEE S/N, which potentially biases the chemical abundance profiles of these elements at lower metallicities.

The work in Chapter 2 (Hayes et al. 2018a) was published along side a companion paper (Fernández-Alvar et al. 2018) lead by Emma Fernandez-Alvar and Carlos Allende Prieto, and they helped refine the chemical selection of the high-Mg and low-Mg populations addressed in that Chapter.

The targeting of TriAnd in APOGEE was an intentional effort of Rachael Beaton and Adrian Price-Whelan, making possible the research in Chapter 3. The comparison of the chemistry of this population to that of the chemistry of Sgr dSph was enabled by Sten Hasselquist, who provided his selection of Sgr dSph members prior to their publication along with a number of conversations about the reliability of the chemical abundances of cool giants in APOGEE. Sten provided critical feedback that helped refine the kinematic selection of Sgr stream stars in Chapter 5.

Chapter 4, was the product of a collaboration between David Law, Steven Majewski, and the author. David Law provided the array of Sgr stream models needed to compare with the author's observational selection of Sgr stream stars and ultimately measure the solar reflex motion from the Sgr stream.

Finally, the remaining coauthors on these works have all contributed either as architects of APOGEE, or have given valuable feedback on the manuscripts that have now all been accepted and published: Andres Almeida, Borja Anguiano, Giuseppina Battaglia, Timothy Beers, Dmitry Bizyaev, Joel Brownstein, Leticia Carigi, Ricardo Carrera, Roger Cohen, Katia Cunha, J. G. Fernández-Trincado, Peter Frinchaboy, D. Annibal García-Hernández, Doug Geisler, Ivan Lacerna, Richard Lane, Sara Lucatello, Allison Matthews, Szabolcs Mészáros, Dante Minniti, Christian Moni

Bidin, Ricardo Mũnoz, David Nidever, Christian Nitschelm, Audrey Oravetz, Daniel Oravetz, Kaike Pan, Alexandre Roman-Lopes, William Schuster, Verne V. Smith, Jennifer Sobeck, Guy Stringfellow, Baitian Tang, Patricia Tissera, Olga Zamora, along with the above mentioned coauthors.

Chapter 2

Distinct Metal-Poor Populations Seen with APOGEE DR13

Summary

We find two chemically distinct populations separated relatively cleanly in the [Fe/H] - [Mg/Fe] plane, but also distinguished in other chemical planes, among metal-poor stars (primarily with metallicities [Fe/H] < -0.9) observed by the Apache Point Observatory Galactic Evolution Experiment (APOGEE) and analyzed for Data Release 13 (DR13) of the Sloan Digital Sky Survey. These two stellar populations show the most significant differences in their [X/Fe] ratios for the α-elements, C+N, Al, and Ni. In addition to these populations having differing chemistry, the low metallicity high-Mg population (which we denote the HMg population) exhibits a significant net Galactic rotation, whereas the low-Mg population (or LMg population) has halo-like kinematics with little to no net rotation. Based on its properties, the origin of the LMg population is likely as an accreted population of stars. The HMg population shows chemistry (and to an extent kinematics) similar to the thick disk, and is

likely associated with *in situ* formation. The distinction between the LMg and HMg populations mimics the differences between the populations of low- and high-α halo stars found in previous studies, suggesting that these are samples of the same two populations.

2.1 Introduction

A key step to reconstructing the history of the Milky Way's formation and evolution is to identify and characterize its constituent stellar populations. Metal-poor stars probe the early evolution of the Galaxy and give clues to the origin of its first components. Among the Milky Way (MW) components containing a large fraction of metal-poor stars are the thick disk (originally known as Intermediate Pop II stars and later reidentified by Yoshii 1982; Gilmore & Reid 1983) via its metal-poor extension (the metal-weak thick disk, MWTD, Morrison 1993; Chiba & Beers 2000; Beers et al. 2002), globular clusters and dwarf MW satellite galaxies, and the halo, possibly separating into an inner- and outer-halo components (Hartwick 1987; Sommer-Larsen & Zhen 1990; Allen et al. 1991; Kinman et al. 1994; Norris 1994; Carollo et al. 2007, 2010; Beers et al. 2012), but containing sub-populations of globular clusters (Zinn 1993) and fields stars accreted from hierarchical formation, which undoubtedly played a key role in the formation of the halo. A long standing problem is whether and how these different populations may be discriminated from one another by their spatial, kinematical and chemical distributions.

A commonly-used strategy is to rely on kinematical definitions to separate stars into populations (Venn et al. 2004; Reddy et al. 2006; Ruchti et al. 2011; Ishigaki et al. 2012, 2013). Unfortunately, this is fraught with several difficulties, not least that it requires that the necessary kinematical data are in hand and of sufficient quality to provide meaningful discrimination. More problematical than these practical requirements is that the kinematical distributions of these various Galactic components typically overlap, so that it is generally not possible to undertake definitive separations of stars into their respective populations with kinematical information alone. Even resorting to simple statistical prescriptions can be perilous given uncertainties in critical priors used to define and fit distribution functions, such as the number of components to fit (see the discussion in Carollo et al. 2010) and their intrinsic shapes (not necessarily Gaussian) and therefore free parameters.

Nonetheless, studies of the detailed chemistry of kinematically-defined populations have successfully revealed some of the primary chemical characteristics of these metal-poor populations. The chemical properties of the thick disk and at least some subset of the halo, although not always cleanly distinct but showing overlaps, have been shown to exhibit demonstrably different mean chemistry for numerous chemical elements (Nissen & Schuster 1997, 2010, 2011; Ishigaki et al. 2012; Ramírez et al. 2012; Ishigaki et al. 2013). For example, these studies have shown that at least some fraction of halo stars have lower abundances of α-elements (particularly O, Mg, and Si), Na, Ni, Cu, and Zn and higher Eu enrichement than those of the thick disk at metallicities [Fe/H] $\gtrsim -1.5$.

One early study of the detailed chemical abundances of 29 metal-poor stars suggested that there may be two chemical abundance patterns amongst halo stars, one of which differed from the thick disk abundance pattern (Nissen & Schuster 1997). In a subsequent study of an enlarged sample of 94 stars with metallicities $-1.6 <$ [Fe/H] -0.4, Nissen & Schuster (2010) used chemical abundances to resolve two rather distinct and mostly non-overlapping populations of stars with halo-like kinematics in the [Mg/Fe]-[Fe/H] chemical plane, with one population having chemistry consistent with the thick disk and the other distinctly less Mg-enriched. Among differences in Mg and other α-elements (distinguishable as "high and low-α" halo star groupings), these two metal-poor populations were shown to have different abundances in many of the odd-Z and heavier elements listed above (Nissen & Schuster 2010, 2011; Navarro et al. 2011; Ramírez et al. 2012; Sheffield et al. 2012; Jackson-Jones et al. 2014; Hawkins et al. 2015).

Furthermore, using isochrone fits to stellar surface temperatures and gravities, these two [α/Fe] groupings were shown to exhibit different mean ages, with the low-α population being younger (Schuster et al. 2012). From the α-element abundances and kinematics of the two populations, these past studies have suggested that the low-α population has been accreted through the mergers of dwarf spheroidal-like galaxies (an origin also suggested for "young halo" globular clusters; see Zinn 1993), whereas the high-α stars were likely formed *in situ* or have been kicked out from the disk (Sheffield et al. 2012; Johnston 2016). Recent studies have also revealed low-α bulge stars, most of which are thought to be chemically associated with the thin disk (Recio-Blanco et al. 2017). While most of these low-α bulge stars have α-element abundances that seem too high to be associated with the low-α halo population, a few of these "bulge stars" may have chemical abundances more similar to the low-α halo population. It would not be surprising if low-α halo stars were found in the bulge, since the densities of other stellar populations increase toward the center of the Galaxy.

Despite the proven utility of high precision, high resolution spectroscopic measurements of chemical abundances to distinguish chemically distinct populations of metal-poor stars, such work is observationally expensive. Consequently, previous sample sizes have generally been limited to a few hundred metal-poor stars (as in the references above). However, the advent of systematic high resolution surveys, such as the APOGEE survey (Apache Point Observatory Galactic Evolution Experiment; Majewski et al. 2017), the Gaia-ESO Survey (Gilmore et al. 2012), and the GALAH survey (Galactic Archaeology with HERMES; De Silva et al. 2015), brings the opportunity to put these types of studies on a much firmer statistical footing. In this work, we use data from the APOGEE survey to gain a more comprehensive view of the chemical differences between populations of metal-poor stars.

The APOGEE-1 survey (Majewski et al. 2017) observed $\sim 146,000$ stars with good quality ($S/N \geq 100$), high resolution ($R \sim 22,500$), infrared (1.5-1.7μm) spectra from which abundances have been derived for up to 23 elemental species in Data Release 13 (DR13; Albareti et al. 2017), at least for more metal-rich and cool stars (Holtzman et al. 2015). Because metal-poor stars are relatively rare and APOGEE, for the most part, uses no special pre-selection for them, they comprise a relatively small fraction of the APOGEE sample. Nevertheless, the APOGEE-1 sample (according to abundances derived for DR13) includes over 1,000 metal-poor stars having [Fe/H]< -1.0 extending down to [Fe/H] ~ -2.0 (i.e., a sample several times larger than previous studies) and with reliable chemical abundances for as many as 12 elements. Such a large sample of metal-poor stars and a highly dimensional chemical space enables robust searches for chemically distinct metal-poor populations, and allows testing of previous claims with a larger statistical footing. Moreover, because the main APOGEE survey targets are only selected photometrically, APOGEE-based studies are free of kinematical biases and include stars from a much larger volume of the Galaxy than previous studies, especially those restricted to observing nearby stars with measured proper motions (e.g., Reddy et al. 2006; Nissen & Schuster 2010, 2011; Ishigaki et al. 2012, 2013; Bensby, Feltzing, & Oey 2014).

This work differs from the past study of metal-poor field stars with APOGEE by (Hawkins et al. 2015) in the lack of any kinematical selection and use of data driven chemical identification of distinct chemical populations that is supported by independent statistical clustering analyses. In addition, we use APOGEE data from DR13, which, through improvements to the data reduction, stellar parameter, and chemical abundance pipelines has improved APOGEE's chemical abundances and provided a much larger sample of metal-poor stars with accurate chemical abundances compared to that provided by DR12, used by (Hawkins et al. 2015). The DR13 improvements to chemical abundance measurements in particular allow us greater power to statistically discriminate and characterize the population of proposed low-α accreted halo stars noticed in previous studies from the population of metal-poor stars having higher α-element abundances.

We show that the [Mg/Fe]-[Fe/H] chemical plane is an especially powerful and reliable diagnostic for this population analysis, and one readily provided by APOGEE for the majority of stars, while other element ratios, like [Al/Fe] and [(C+N)/Fe] are equally discriminating, if less available for all stars ([(C+N)/Fe] becomes uncertain at the lowest metallicities in our study; see Section 2.3.2 for a discussion of the limitations of the C and N abundances). We provide evidence supporting our new selection criteria in these and other chemical dimensions by presenting the results of multi-dimensional clustering algorithms on the APOGEE-observed metal-poor stars. Moreover, because our sample is kinematically unbiased, we can more reliably explore and characterize the kinematical properties of these chemical groupings; we show that the two primary [Mg/Fe]-based metal-poor groupings have decidedly different kinematical properties that give clues to their origin and relation to the main spatio-kinematical populations of the Galaxy.

In particular, as suggested by previous work, the high-Mg population is relatively kinematically cold and rotating while the low-Mg population has hot kinematics consistent with expectations for an accreted population. Finally, because metal-poor stars characterized by low-α abundance patterns are traditionally attributed to satellite accretion, we compare the detailed chemical properties of our Mg-populations to those in MW satellites.

This chapter is organized as follows. In Section 2.2 we discuss the data and selection criteria employed to create the parent stellar sample used throughout the chapter. In Section 2.3 we first discuss our identification of two populations of metal-poor stars based on their [Mg/Fe]. We then examine the chemical signatures of these populations in other dimensions of APOGEE-observed chemical space, and apply multidimensional clustering algorithms to justify further our characterization of these metal-poor populations. Section 2.3 also presents the kinematical properties of these populations derived from APOGEE radial velocity data. In Section 2.4, we compare our sample of stars and the populations we have defined to those suggested and discussed in previous studies. We also comment on the possible origins of these populations, aided by a comparison of our data to the abundance patterns of MW satellites. We present our conclusions in Section 2.5. A companion paper, Fernández-Alvar et al. (2018), further explores the chemical evolution and star formation histories of the two populations discriminated in this work.

2.2 Data

Using the Sloan 2.5-m telescope at Apache Point Observatory (Gunn et al. 2006) as a part of the third installment of the Sloan Digital Sky Survey (SDSS-III, Eisenstein et al. 2011), APOGEE spectroscopically observed a relatively homogenous sample of $\sim$ 146,000 MW stars to survey its multiple structural components. The details of the APOGEE instrument, survey, data, and calibration are outlined in Majewski et al. (2017) and references therein. Here we present an analysis of the APOGEE data presented in the SDSS Data Release 13 (DR13; Albareti et al. 2017), the first data release of SDSS-IV (Blanton et al. 2017). In this data release, a re-analysis of the spectra presented in SDSS DR12 was performed to improve the quality of derived parameters. Target selection and data reduction for APOGEE are described in detail by Zasowski et al. (2013) and Nidever et al. (2015), respectively, and the APOGEE Stellar Parameter and Chemical Abundances Pipeline (ASPCAP; for a detailed description see García Pérez et al. 2016) was used to determine the stellar parameters and chemical abundances from the best fits to pre-computed libraries of synthetic stellar spectra (e.g., Zamora et al. 2015).

We restrict our analysis to a subsample of stars selected on the basis of a series of APOGEE flags and other constraints. We first removed any stars with the STARFLAGS BAD_PIXELS, VERY_BRIGHT_NEIGHBOR, or LOW_SNR flags set. We also cut any stars with the following ASPCAPFLAGS: METALS_WARN, ROTATION_WARN, METALS_BAD, STAR_BAD, ROTATION_BAD, or SN_BAD. Descriptions of these flags can be found online in the SDSS DR13 bitmask documentation[1].

In addition to trimming the APOGEE data set using quality flags, we also require that the visit-to-visit velocity scatter be small, i.e. $V_{scatter} \leq 1$ km s^{-1}, because a larger velocity scatter may indicate surface activity, the presence of a companion, or other astrophysical complications that may make determined parameters and abundances less reliable. Similarly, we only use stars with velocity uncertainties $V_{err} \leq 0.2$ km s^{-1}, to exclude stars with large velocity uncertainties that may have less reliably derived parameters. We have also restricted our analysis to stars with surface temperatures

[1] `http://www.sdss.org/dr13/algorithms/bitmasks/`

4000 K < T_{eff} < 5500 K (selected before applying the post-calibration corrections to produce the surface temperatures and gravities listed in Table 2.1), given that, as of DR13, ASPCAP is not yet tuned for reliable parameter estimation for cooler stars or those that are warmer and have weaker lines.

Finally, because we will be primarily concerned with magnesium abundances, we only select stars with σ[Mg/Fe] < 0.1 and S/N > 100. However, in considering other elemental abundances throughout the remainder of the chapter, we only examine (but do not remove from the sample) stars with uncertainties on those abundances below 0.1 dex as well. Because globular clusters are known to exhibit high levels of self-enrichment (Gratton et al. 2004), we have excluded those cluster stars that are easily distinguished from field stars and that can be associated with specific globular clusters (based on proximity, radial velocities, and metallicities). The Sagittarius dwarf spheroidal galaxy (Sgr dSph) is the only dSph present in DR13, so in addition to removing globular cluster members, we also removed known Sgr dSph members. While the coolest, most luminous Sgr dSph giants are removed by our T_{eff} > 4000 K requirement, we also removed any stars with the TARGFLAG APOGEE_SGR_DSPH, which was assigned to known Sgr dSph members. After all of these quality cuts and the exclusion of globular cluster and Sgr dSph stars, we are left with 61,742 stars for study using the calibrated ASPCAP stellar parameters and chemical abundances.

2.3 Results and Analysis

2.3.1 Two Populations Seen in [Mg/Fe] Ratios of Metal-Poor Stars

Visual inspection of the elemental abundances observed by APOGEE for metal-poor stars revealed the most apparent and distinct bimodality in the distribution of [Mg/Fe]. We therefore first present and examine the distribution of Mg abundances. This strategy is also motivated by previous studies of metal-poor stars that also found two distinct metal-poor groups based on their [α/Fe] ratios, or specifically their [Mg/Fe] ratios (see Section 2.1).

Figure 2.1 shows the distribution of [Mg/Fe] with [Fe/H] for all stars that made it through the quality criteria discussed in Section 2.2. Most obvious in this plot are the high- and low-[Mg/Fe] tracks between [Fe/H] ~ -0.9 and $+0.4$ nominally corresponding to the thick and thin disks respectively. In the APOGEE DR 13 data, the high-α sequence commonly associated with the thick disk (e.g., Bovy et al. 2016, and references therein) seems to taper off, and there appears to be a gap between the thick disk and another set of stars with not only a lower level of [Mg/Fe], but decreasing [Mg/Fe] with increasing metallicity.

This gap is made more apparent in Figure 2.2, where we plot density contours over our data to demonstrate that there is a true low density valley separating the two sequences of metal-poor stars. The peak-to-valley ratio between the density along the Mg-poor sequence and the density in the valley, tracked by the sloped dashed line in Figure 2.2, gives us an idea of the significance of this second, low-Mg abundance sequence. At a metallicity of [Fe/H] ~ -1.5 the peak-to-valley ratio is about 1.5, increasing to 2.5 at a metallicity of [Fe/H] ~ -1.2, and it is highest at about 3.0

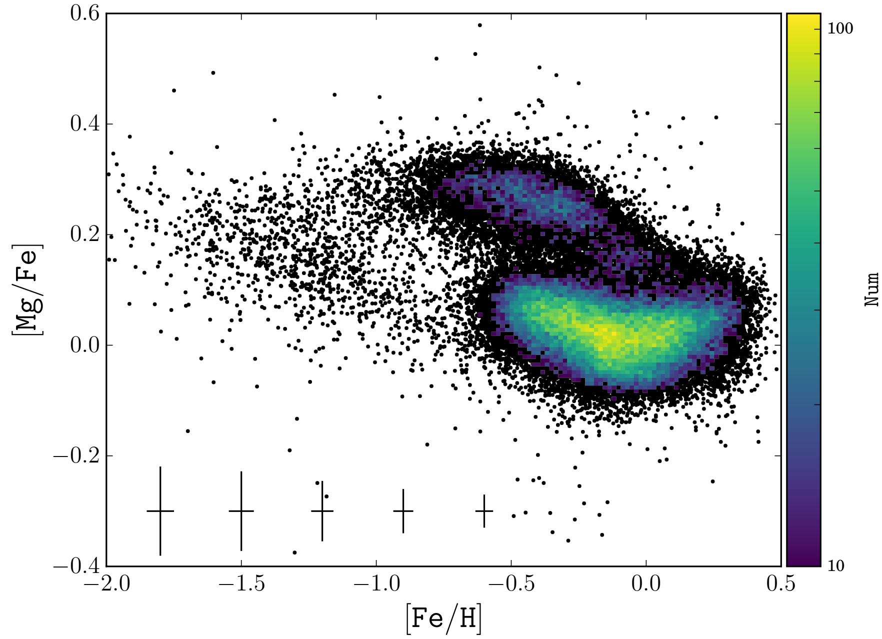

Fig. 2.1.— Distribution of [Mg/Fe] with metallicity for the APOGEE DR 13 stars surviving the quality cuts discussed in Section 2.2. A 2D histogram is plotted for the highly populated portions of this chemical space (corresponding to the chemical domain of the relatively more metal-rich thin and thick disk populations), while individual stars are plotted where APOGEE observed stars are less populous in this plane. The plotted error bars show the median abundance uncertainties in 0.3 dex wide metallicity bins. In addition to the traditional thick disk sequence seen at [Fe/H] > -1.0, a noticeable third sequence of stars appears between the low metallicity end of our sample and [Fe/H] ~ -1.0, with decreasing [Mg/Fe] with increasing metallicity.

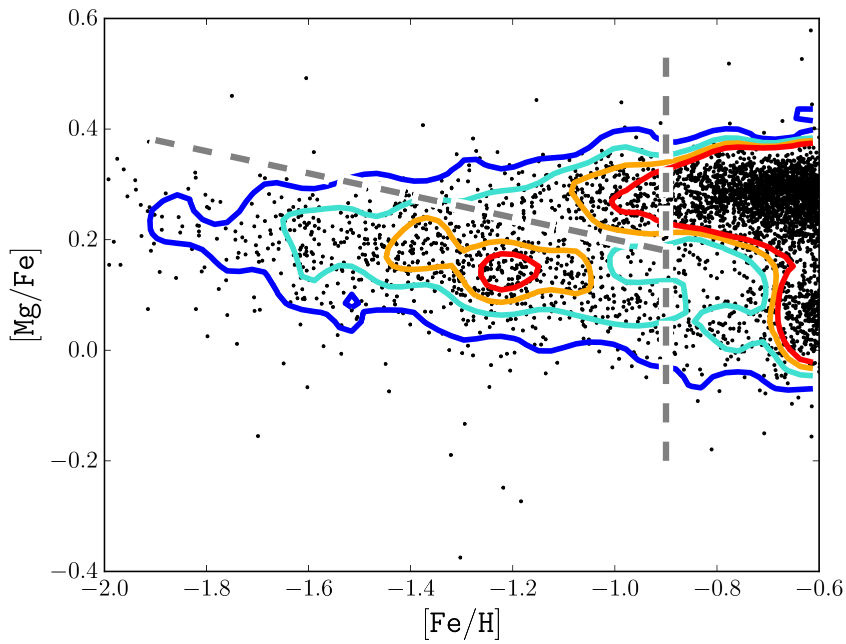

Fig. 2.2.— A magnified portion of the metal-poor region of Figure 2.1, with contours showing the density of stars in the metal-poor regions of Figure 2.1. The contours are at 5, 15, 25 and 35 stars per 0.0039 dex^2. These contours demonstrate that there is a low density valley separating two higher density regions, one with lower [Mg/Fe], and one with higher [Mg/Fe] that appears to be a metal-poor extension of the thick disk locus. The sloping dashed line is adopted to separate the two populations based on their [Mg/Fe] and metallicity in Section 2.3.1.

around a metallicity of -1.0. This indicates that the valley separating these two sequences is more significant at higher metallicities, where the chemical separation between this sequence and the nominal thick disk is larger. It also highlights that at lower metallicities the two low metallicity sequences overlap more, so that it is more difficult to separate them.

Thus, at lower metallicities ([Fe/H] $\lesssim -0.9$) the APOGEE data strongly suggest the existence of two populations of stars chemically differentiated by their [Mg/Fe] patterns. For simplicity we initially separate the two populations along the gap or valley by [Mg/Fe] $= -0.2\times$[Fe/H], as shown by the sloped dashed line in Figure 2.2. We designate the low-[Mg/Fe] population as the Low-Mg (LMg) population and the high-[Mg/Fe] magnesium population as the High-Mg (HMg) population. For this analysis, we initially restrict our analysis to metallicities of [Fe/H] ≤ -0.9, to avoid contaminating the LMg population with stars from the thin disk locus. Note, however, that we show below in Section 2.3.2 that the LMg population extends to slightly higher metallicities as seen by the consideration of [(C+N)/Fe] ratios. Our initial division of the LMg and HMg for [Fe/H] ≤ -0.9 is shown in Figure 2.3. In Table 2.1 we report the relevant properties, stellar parameters, and chemical abundances of the stars categorized into these two populations.

Given that the gap between these populations is not completely devoid of stars, there is some uncertainty in separating them, and there is likely to be some spread of each population across the adopted division, whether due to intrinsic scatter of the true underlying populations or to measurement uncertainties, leading to some low level of cross-contamination that appears to become more significant at lower metallicities ([Fe/H] ~ -1.3) where the sequences begin to merge. This is examined in more detail using the full chemical profiles of these populations and clustering

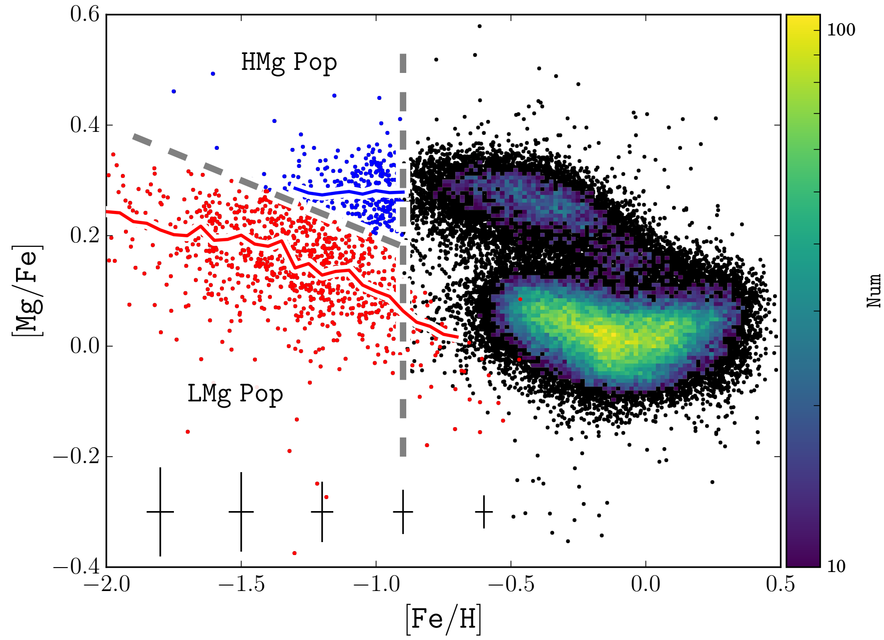

Fig. 2.3.— Same as in Figure 2.1, but with the initial division to separate the relatively Mg-poor population LMg (red) and the Mg-rich population HMg (blue). Stars in the LMg population with metallicities [Fe/H] > −0.9 have been selected based on their [(C+N)/Fe] abundance ratios, since they appear to follow the abundance pattern of the LMg population as discussed in Section 2.3.2. Over-plotted are the roving boxcar medians of 50 nearest neighbors, again color-coded by population

algorithms in Section 2.3.3. Because the HMg population smoothly connects with the thick disk locus, this population is likely the metal-weak extension of the thick disk. The origin of the LMg population is not immediately clear and is examined in more detail in later sections.

2.3.2 Chemical Signatures

While we have identified a potential division in populations with low metallicities in [Mg/Fe]-[Fe/H] space, for it to have astrophysical significance, we expect it should be revealed in additional dimensions, which we now examine. In the following subsections we present and analyze the chemical distributions of our sample in other element planes, restricting our analysis of each element to the stars with uncertainties σ[X/Fe] < 0.1 dex in that element alone.

α-Elements: O, Si, and Ca

We first examine other α-elements measured by APOGEE with high precision: O, Si, and Ca, as well as the ASPCAP global α-element parameter (derived from the initial ASPCAP fit to all α-elements, O, Mg, Si, Ca, S, Ti; see Holtzman et al. 2015), whose abundances relative to Fe are shown in Figure 2.4. Ti is a commonly studied α-element and is measured by APOGEE, however, it is considered unreliable because it is not able to reproduce the [Ti/Fe] bimodality seen in solar neighborhood studies or in other α-element abundances measured by APOGEE (Holtzman et al. 2015). The inconsistency with optically derived Ti abundances may be due to the ASPCAP inclusion of lines affected by NLTE or saturation (Hawkins et al. 2016) in the measurement of Ti, or a high T_{eff} sensitivity of H-band TiI lines (Souto et al. 2016), regardless of the cause, because of this unreliability, we do not analyze Ti here.

Table 2.1. Properties, Parameters, and Population Identification of APOGEE DR13 Metal-Poor Stars

Column	Column Label	Column Description
1	APOGEE	APOGEE Identifier
2	RAdeg	R.A. (decimal degrees)
3	DEdeg	Decl. (decimal degrees)
4	GLON	Galactic Longitude (decimal degrees)
5	GLAT	Galactic Latitude (decimal degrees)
6	Jmag	2MASS J magnitude
7	Hmag	2MASS H magnitude
8	Kmag	2MASS Ks magnitude
9	HRV	Heliocentric radial velocity (km s^{-1})
10	e_HRV	Radial velocity uncertainty (km s^{-1})
11	Teff[a]	Effective surface temperature
12	log g[a]	Surface gravity
13	Vturb	Microturbulent velocity (km s^{-1}
14	Vmacro	Macroturbulent velocity (km s^{-1})
15	[Fe/H]	Log abundance, [Fe/H]
16	e_[Fe/H]	Uncertainty on [Fe/H]
17	[a/Fe]	Log abundance, [α/Fe] (see text for details)
18	e_[a/Fe]	Uncertainty on [α/Fe]
19	[C/Fe]	Log abundance, [C/Fe]
20	e_[C/Fe]	Uncertainty on [C/Fe]
21	[N/Fe]	Log abundance, [N/Fe]
22	e_[N/Fe]	Uncertainty on [N/Fe]
23	[O/Fe]	Log abundance, [O/Fe]
24	e_[O/Fe]	Uncertainty on [O/Fe]
25	[Mg/Fe]	Log abundance, [Mg/Fe]
26	e_[Mg/Fe]	Uncertainty on [Mg/Fe]
27	[Al/Fe]	Log abundance, [Al/Fe]
28	e_[Al/Fe]	Uncertainty on [Al/Fe]
29	[Si/Fe]	Log abundance, [Si/Fe]
30	e_[Si/Fe]	Uncertainty on [Si/Fe]
31	[K/Fe]	Log abundance, [K/Fe]
32	e_[K/Fe]	Uncertainty on [K/Fe]
33	[Ca/Fe]	Log abundance, [Ca/Fe]
34	e_[Ca/Fe]	Uncertainty on [Ca/Fe]
35	[Cr/Fe]	Log abundance, [Cr/Fe]
36	e_[Cr/Fe]	Uncertainty on [Cr/Fe]
37	[Mn/Fe]	Log abundance, [Mn/Fe]
38	e_[Mn/Fe]	Uncertainty on [Mn/Fe]
39	[Ni/Fe]	Log abundance, [Ni/Fe]
40	e_[Ni/Fe]	Uncertainty on [Ni/Fe]
41	[CN/Fe]	Log abundance, [(C+N)/Fe]
42	e_[CN/Fe]	Uncertainty on [(C+N)/Fe]
43	[CNO/Fe]	Log abundance, [(C+N+O)/Fe]
44	e_[CNO/Fe]	Uncertainty on [(C+N+O)/Fe]
45	Pop	Assigned Population (LMg or HMg)

[a]Corrected according to the recommendations in the APOGEE DR13 documentation (`http://www.sdss.org/dr13/irspec/parameters/`) to remove surface temperature and gravity trends found post-calibration

Note. — Table 2.1 is published online in Hayes et al. (2018a). The columns are shown here for guidance regarding its form and content.

Note. — Null table entries are given values of -9999.

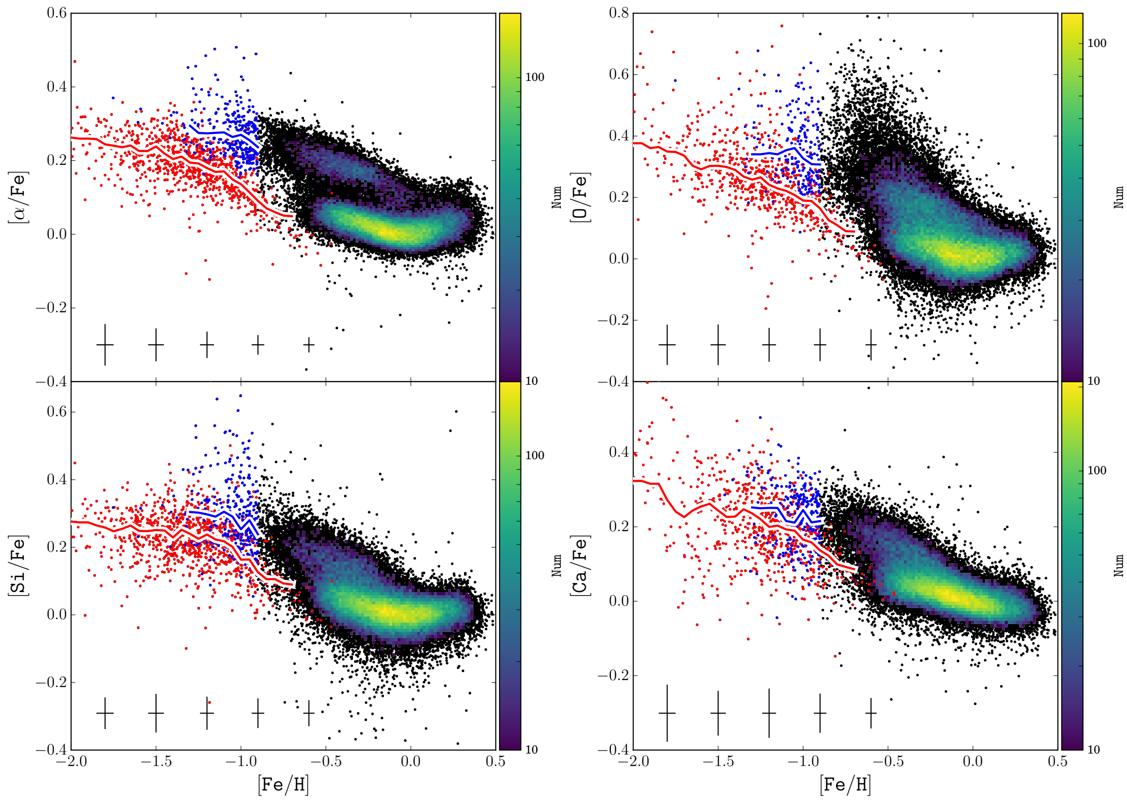

Fig. 2.4.— Distribution of different α-elements with [Fe/H], with a 2D histogram used for the densely populated regions. Stars of the LMg and HMg populations are color-coded the same as in Figure 2.3. Over-plotted are lines of moving medians (using the 50 nearest neighbors), color-coded by population. The separation between the LMg and HMg populations is smaller in these other α-elements than for Mg, but still appears to exist for most of these chemical planes, except potentially that for Ca, where the metal-poor population overlap is greatest.

Reassuringly, we find that the LMg population is consistently lower in O, Si, and Ca abundances and the HMg population is higher, as seen in magnesium, however, the separation between the LMg and HMg populations is not as clean in these other α-elements as it is in magnesium. The potential exception to this is perhaps in the total α, which could be a result of the Mg influence in determining the global α-element abundance by ASPCAP. For the other α-element chemical planes, the separation appears to be largest in O, weaker in Si, and weakest in Ca.

While abundance uncertainties may help obscure differences in α-element abundance trends between the LMg and HMg populations, the typical measurement uncertainties for each of the α-elements are quite similar (at a given metallicity). Thus the larger separation in lighter α-elements than heavier ones seems to be from an astrophysical source rather than due to differences in random uncertainties (although systematic errors could still obscure differences). The size of the separation of the LMg and HMg populations in different α-elements likely arises from the influence of different types of supernovae. For example, the LMg population may have experienced enrichment from a higher fraction Type Ia supernovae. Tsujimoto et al. (1995) have shown that, while Type Ia supernovae have contributed a negligible amount of O and Mg (about 1% each) in the solar neighborhood, they have contributed a larger fraction of Si (17%), Ca (25%), and Fe (57%). They show that these fractions increase in lower mass/metallicity system, such as the LMC, in which Type Ia supernovae still contribute a small fraction of O and Mg (3%), but make up an even larger fraction of the Ca (44%) and Fe (76%). Another possible explanation for the different separations in α-elements is that the two metal-poor populations could have been chemically enriched by supernovae of considerably different progenitor masses or metallicities, which may effect their chemical abundance patterns (see Nomoto et al. 2013).

Light and Odd-Z elements: C, N, Al, and K

Figure 2.5 presents some of the light and odd-Z element patterns, and demonstrates a very distinct separation in aluminum at the level of almost ~ 0.5 dex. The population with lower Mg (the LMg population) is found to be Al-poor, and the higher Mg population (the HMg population) has solar-level to slightly above solar enriched levels of Al, which is consistent with the results from the smaller more metal-rich sample from Hawkins et al. (2015). The gap in Al between the two populations is remarkably large. While it is tempting to use Al as the primary discriminating element for low metallicity populations, we refrain from doing so now for two reasons (1) the typically larger ASPCAP uncertainties on [Al/Fe] ratios, and (2) much smaller sample sizes when selecting stars based on Al abundances rather than Mg abundances because fewer stars have the low uncertainties necessary to make fine chemical distinctions. However, future studies with better aluminum data may find great power in using this element as a discriminator of these two metal-poor populations.

While there is significantly more scatter, we also see some distinction between these two populations in carbon, with the LMg stars typically having lower [C/Fe] (for a given metallicity), although first dredge-up and subsequent mixing for stars at the red giant branch (RGB) bump will bring up CNO-cycle processed material, typically decreasing the surface [C/N] from its natal level through a decrease in ^{12}C and an increase in ^{14}N (Gratton et al. 2000; Karakas & Lattanzio 2014). In the metallicity range where our two populations overlap, we find that their typical [N/Fe] ratios are quite similar. At lower metallicities the N-abundances increase in the LMg stars, however, because these are measured from CN features in APOGEE spectra, which

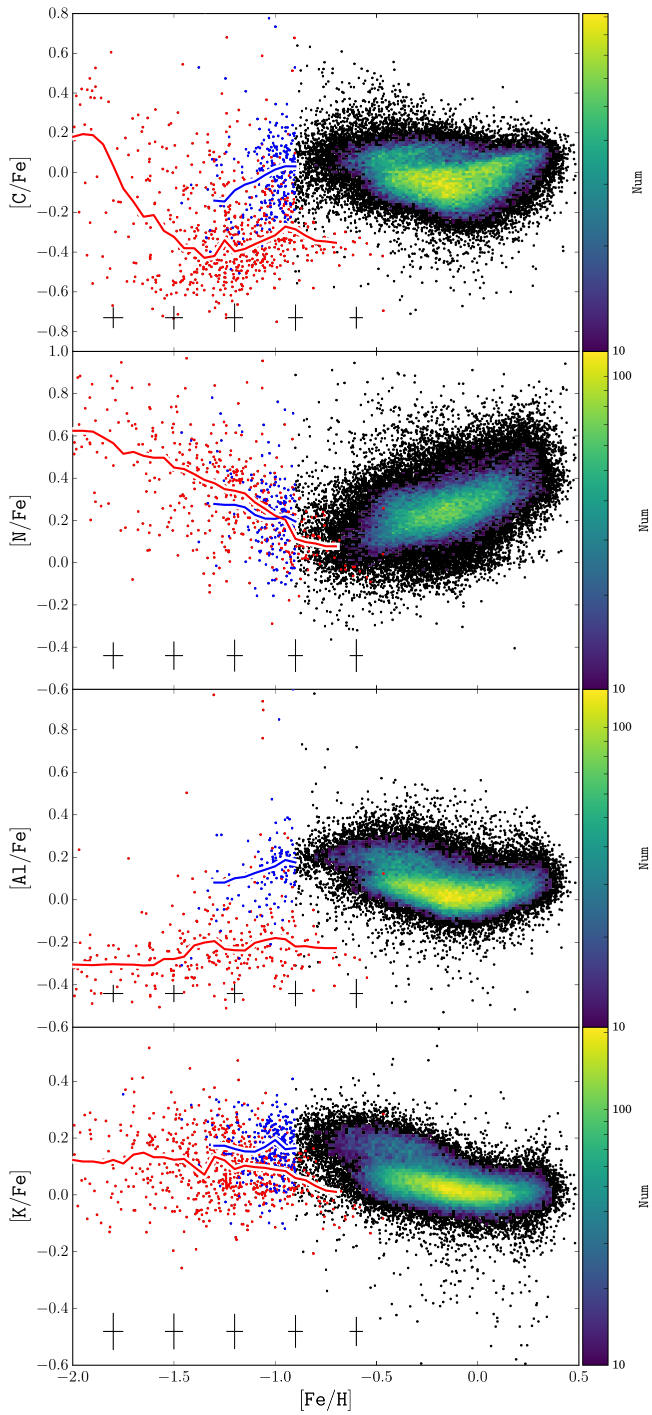

Fig. 2.5.— Same as Figure 2.4, but for the abundance distributions of the light and odd-Z elements C, N, Al, and K. The element here for which the two metal-poor populations stand out most distinctly from one another is Al, where the LMg population appears Al-poor and the HMg population has approximately solar Al levels.

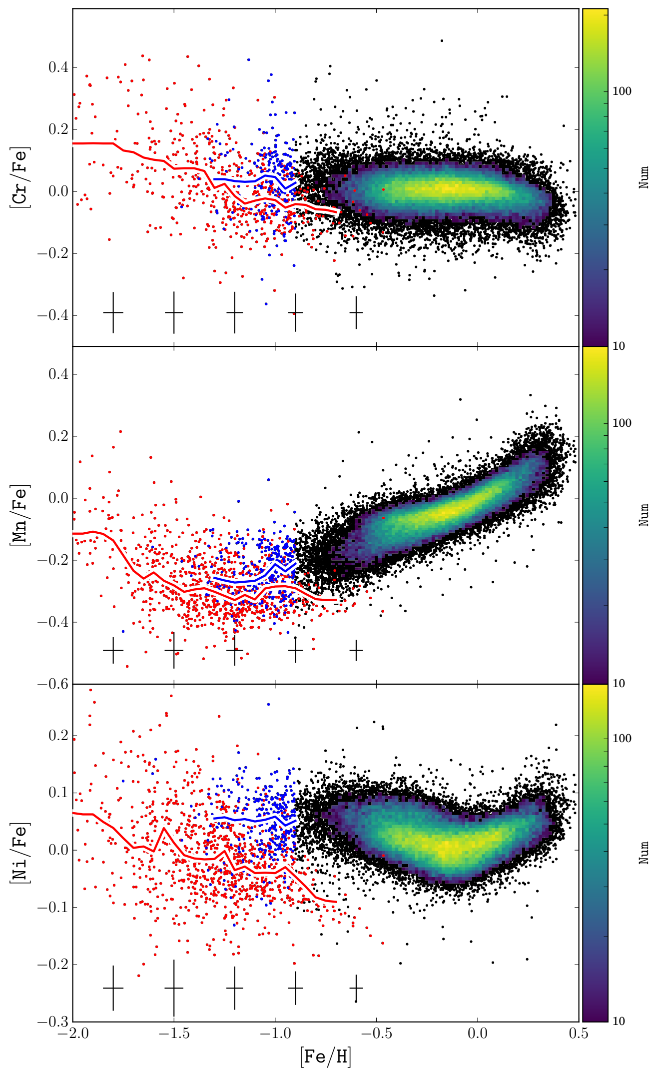

Fig. 2.6.— Same as Figure 2.4, but for the abundance distributions of the iron peak elements Cr, Mn, and Ni. Here we see some significant separation of the LMg and HMg populations in Ni, in a fashion similar to that seen in some of the α-elements.

are weak and can disappear for very metal-poor stars (Holtzman et al. 2015), these [N/Fe] ratios are very uncertain (and instead many are upper limits). Note that unlike other chemical abundances from APOGEE, which are calibrated to remove abundance trends with temperature seen in cluster stars (Holtzman et al. 2015), C and N are not calibrated in this way because dredge-up and mixing in giants intrinsically produces trends with temperature. The data exhibit only a slight difference in the median [K/Fe] ratios between the LMg and HMg populations, which is diluted by the large scatter in both populations, such that their [K/Fe] distributions appear similar.

Iron Peak Elements: Cr, Mn, and Ni

Figure 2.6 presents the distributions of heavier, iron-peak elements. The most significant separation between these two populations is in Ni, which, although less pronounced than for Al, is similar in appearance to some of the α-element abundance separations (as shown in Figure 2.4). For Ni we see a slight overlap of the two populations, but most HMg stars have higher Ni abundances than the LMg stars, again consistent with the findings of Hawkins et al. (2015). Like K, the distributions of Cr and Mn abundances for the two populations mostly overlap, although the median of these distributions show slight differences, with the LMg population having lower [Cr/Fe] and [Mn/Fe] ratios. The Cr and Mn distributions appear to be flat or decreasing with decreasing metallicity above [Fe/H] $\gtrsim -1.4$, but at lower metallicities the LMg population appears to begin increasing in Cr and Mn with decreasing metallicity.

For Cr and Mn, as well as for Ni and possibly C, at low metallicities there is a slight increase in [X/Fe] ratios with decreasing metallicity. The likely reason for this trend is that, at low metallicities, the lines used to measure these elements become increasingly weaker, so much so that they should be undetectable at the typical S/N of our selection criteria. Thus, the measurements presented at the lowest metallicities would instead be upper limits. We would then expect to see an increasing [X/Fe] trend with decreasing metallicity because of two effects. (1) When measuring upper limits, ASPCAP is effectively fitting the noise present in spectra, so for a set of stars with a range in temperature, we expect the derived upper limits to be temperature dependent. Hotter stars have intrinsically weaker lines, so when fitting the same noise level, higher abundances will be derived for these stars than for cool stars, which should have stronger lines for a given abundance. This has the effect of artificially increasing the median abundance ratio at low metallicities where these upper limits appear. (2) We also expect lower abundance ratios to have higher reported uncertainties, and thus more likely to result in a star being cut out at these low metallicities by our maximal uncertainty criterion. By tending to remove stars with lower and less certain abundances, we artificially drive up the median abundance ratios at the lowest metallicities (as we approach [Fe/H] ~ -2.0), and we expect this to affect especially elements like Cr, Mn, Ni and possibly C.

These effects should primarily impact Cr, which has the weakest lines of the four elements mentioned above, the abundances reported are more likely to represent upper limits below metallicities of around [Fe/H] ~ -1.5 or -1.6. Cr would then be followed by Mn and Ni, which would both return upper limits at even lower metallicities. On the other hand, for carbon it would be more surprising if overestimated line strengths are responsible for the up turn at low metallicities, because there are so many carbon features throughout the APOGEE spectra that are used to derive [C/Fe]. More of the [C/Fe] ratio measurements, therefore, may be real even at lower metallicities. Moreover, stars with high [C/Fe] ratios are not unexpected given the existence of carbon-enhanced metal-poor (CEMP) stars with [C/Fe] $> +1.0$ (see Beers & Christlieb 2005; Frebel & Norris 2015, and references therein), so the trends seen in [C/Fe] may well be real.

Combined Light Elements: (C+N) and (C+N+O)

As mentioned above, first dredge-up and mixing at the RGB bump can effect the surface abundances of (primarily) carbon and nitrogen (with small changes possible for oxygen; Gratton et al. 2000; Karakas & Lattanzio 2014; Martig et al. 2016), so that these abundances no longer reflect their natal values. However, the total abundance of carbon, nitrogen, and oxygen (as represented by [(C+N+O)/Fe]) should remain unchanged by the dredge-up, and since the birth oxygen abundance is nearly conserved in low-mass stars, the surface [(C+N)/Fe] is also essentially unchanged (Gratton et al. 2000; Martig et al. 2016). Figure 2.7 shows that most of the stars in the LMg and HMg populations exhibit different C+N and C+N+O abundances, and they are quite distinct. In both of these abundances, the HMg exhibits a scatter around solar [(C+N)/Fe] and [(C+N+O)/Fe] of $+0.2$ dex. For the same metallicity, the LMg shows lower C+N and C+N+O abundances than the HMg, which provides another example of a chemical space where the LMg and HMg populations appear to separate reasonably.

The LMg stars exhibit decreasing C+N and C+N+O abundances with increasing metallicity in addition to having a decreasing scatter with increasing metallicity. The higher scatter at lower metallicities is most likely due to less reliable abundance measurements from weaker lines (primarily poor N abundances from weak CN lines) in metal-poor stars, but the concentration in LMg abundance ratios especially narrows for [Fe/H] $\gtrsim -1.3$. This tight trend then continues to metallicities higher than our initial examination cutoff at [Fe/H] = -0.9, and we can see a (C+N)-poor group of "LMg-extension" stars that reaches to [Fe/H] ~ -0.5. These stars appear to follow the chemical abundance pattern set by the metal-poor LMg stars, but have [(C+N)/Fe] (and to some extent even [(C+N+O)/Fe]) ratios that deviate significantly from the canonical thin and thick disk populations, which have [(C+N)/Fe] ratios nearly at or greater than solar. Therefore, we assign these stars to the LMg population. We do so explicitly by examining the [Fe/H] > -0.9 stars with subsolar [(C+N)/Fe] and assigning a conservative, by-eye linear expression for the upper [(C+N)/Fe] envelope of this distribution (given numerically by [(C+N)/Fe] = -0.4 [Fe/H] -0.46). We then define stars with [(C+N)/Fe] under this envelope as potential LMg stars, but note that this is a conservative selection, again to avoid thin disk contamination. These more metal-rich LMg stars are also shown in previous figures, where they appear to follow other LMg population trends, and support that these stars are members of this population.

2.3.3 Exploring Multi-Dimensional Chemical Space

As demonstrated, the two metal-poor populations we have identified via their [Mg/Fe] distributions in the APOGEE database are also quite well discriminated in other elemental ratios, such as [Al/Fe] and [(C+N)/Fe]. While we have examined stellar abundances of different elements one by one, these stars live in a highly multi-dimensional chemical space that can be sliced in many different ways to search for distinct stellar populations. For example, the [Ni/Fe] versus [Al/Fe]-plane for stars attributed to the LMg and HMg populations in Figure 2.8, shows a striking separation. This is similar to the separation reported by Nissen & Schuster (2010), who examined [Ni/Fe] versus [Na/Fe] for stars between [Fe/H] = -1.6 and -0.4, and found two populations (which

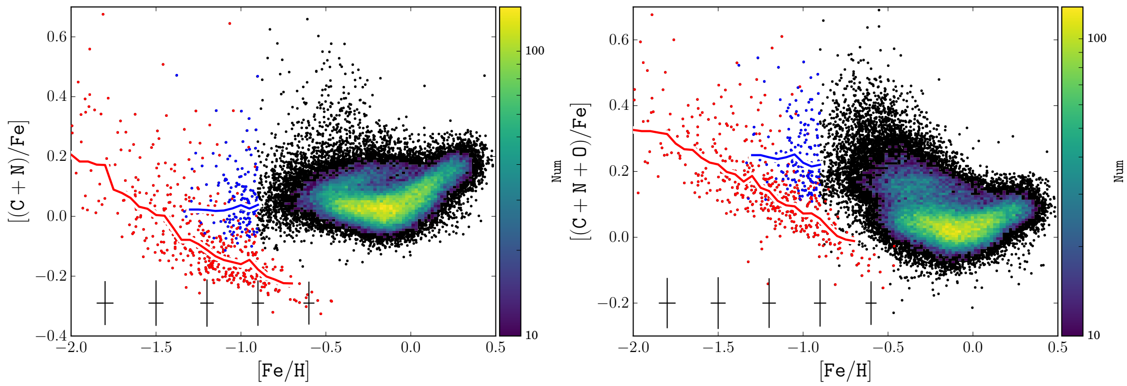

Fig. 2.7.— Same as Figure 2.4, but for the combinations of C, N, and O. There is a relatively high degree of separation of the LMg and HMg populations in both C+N and C+N+O, as well as distinct trends within each population, i.e., the decreasing [(C+N)/Fe] and [(C+N+O)/Fe] ratios with increasing metallicity in the LMg population, and nearly constant ratios in the HMg population.

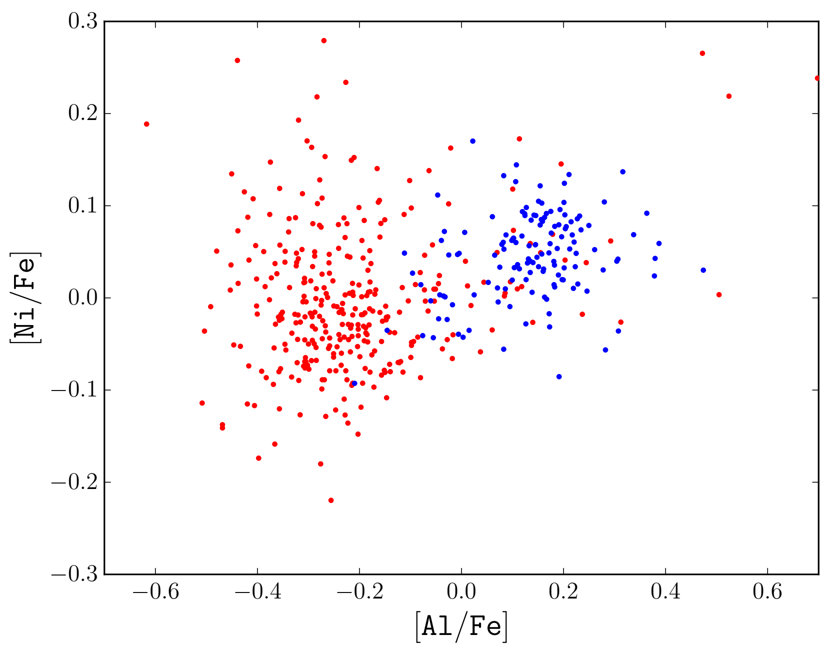

Fig. 2.8.— [Ni/Fe] vs. [Al/Fe] for metal-poor stars ([Fe/H] < -0.9) in the LMg (red) and HMg (blue) populations shown in Figure 2.3. This slice of chemical space is one example where these two populations cluster with good separation, and demonstrate how incorporating different chemical information provides opportunities for further refining the definitions of populations.

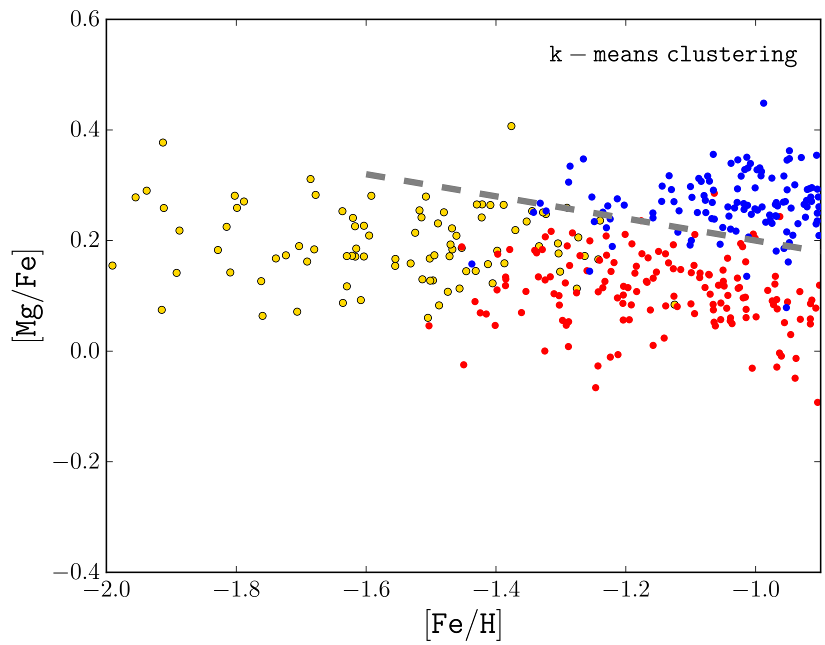

Fig. 2.9.— [Mg/Fe] vs. [Fe/H] projection of the 11-D chemical space probed, where we have performed clustering analyses on stars with well defined chemical abundances, as described in the text. Stars are color-coded by cluster assignment according to the k-means clustering algorithm, two of which (colored red and blue) are very similar to the two populations that we defined by eye in Figure 2.3.

they also selected based on the [Mg/Fe]-[Fe/H]) like those examined here. This perhaps should be expected, because Na and Al are produced through the NeNa and MgAl cycles, which are linked and operate under similar temperature ranges (Arnould et al. 1999); thus Na and Al abundances should be roughly correlated.

But again, Figure 2.8, like all preceding figures are just two-dimensional slices through chemical space, when we have many more dimensions that we can utilize simultaneously. While it is difficult to visualize higher dimensionalities, we can use tools such as clustering algorithms to search this space to provide statistically rigorous tests of our proposed separations.

To conduct such a multidimensional probe and to quantify how well the two populations and their differences are captured by our simple selection in [Mg/Fe] vs. [Fe/H], we utilize two clustering algorithms to independently and objectively look for these populations. The multi-dimensional space we search is that of metallicity ([Fe/H]), [(C+N)/Fe] (which should be more representative of birth abundances than C or N separately due to the effects of first dredge-up, as discussed earlier), and [X/Fe] for O, Mg, Al, Si, K, Ca, Cr, Mn, and Ni, i.e., those elements with good data that were previously examined.

First, we use an algorithm to perform k-means clustering (MacQueen 1967) to search for clusters in the aforementioned 11-dimensional chemical space for all stars with uncertainties under 0.1 dex and [Fe/H] ≤ -0.9 (so that the populations noted in this work are not lost to the much more populous thin and thick disk chemical distributions). We performed a silhouette analysis (Rousseeuw 1987) to determine the optimal number of clusters (k) to represent the data, finding that three clusters best describe the data. The resulting assignment of stars for the three clusters are shown in the [Mg/Fe] - [Fe/H] plane in the left panel of Figure 2.9 color-coded according to their cluster assignment by the k-means algorithm.

Of the three clusters identified, two seem to separate primarily in metallicity from the third cluster of stars typically having [Fe/H] $\lesssim -1.4$ and entirely representing the lowest metallicity stars. This third cluster may reflect the fact that at metallicities below [Fe/H] ~ -1.5 the LMg and HMg populations blend together into one chemically indistinguishable group. Alternatively this third group may be a spurious bifurcation of one of the other two clusters (presumably the cluster corresponding to the LMg), either as an artifact of the k-means algorithm or due to low statistics creating a small gap in an otherwise continuous sequence. Whether there may be an astrophysical reason for this *distinct*, metal poor population should be reconsidered if it persists despite more data or improved techniques applied to this problem.

The remaining two k-means clusters are located at higher metallicities, where the LMg and HMg are more distinct. How these clusters relate to the populations defined by our visual inspection of only the two-dimensional [Mg/Fe]-[Fe/H] plane is shown by the over-plotted dividing line we initially used to separate the LMg and HMg populations in Figures 2.2 and 2.3. As may be seen, our adopted dividing line appears to properly separate most of the stars assigned to either of the more metal-rich clusters defined independently by the k-means algorithm.

Apart from this metal-poor cluster, we note that the k-means clustering has produced one relatively low- and one relatively high-Mg clusters. Specifically, we find that of the stars below and above the line in Figure 2.9 respectively, 90% (146/163) of the LMg population stars are assigned to the low-Mg k-means cluster and 95% (103/108) of the HMg stars are assigned to the high-Mg k-means cluster. Thus, the k-means algorithm identifies clusters relatively consistent (at least at the higher metallicity range of our sample) with the two populations we specified using our by-eye division based on only two chemical dimensions. This suggests that [Mg/Fe] and metallicity alone are a robust discriminator of the two groups of relatively metal-poor stars. We also note that most of the cross-contamination occurs around our dividing line, and somewhat at the metal-poor end of the high-Mg or HMg population distribution, where the third, metal-poor cluster dominates.

The other clustering algorithm that we try is DBSCAN (Ester et al. 1996), a two parameter density-based clustering algorithm that builds clusters by chaining together data points that have a minimum of N neighbors within a multi-dimensional sphere of radius ϵ. Together, these parameters determine a minimum "density" and the algorithm identifies clusters present in the data with that density. Because this algorithm is density based, it will tend to exclude data on the outskirts of clusters, and can be fairly sensitive to the choice of input parameters (which effectively define the desired densities of output clusters). Nevertheless, DBSCAN also delivers results consistent with our by-eye selection in finding two clusters (with input parameters of $N = 17$ and $\epsilon = 0.21$ dex).

Of the stars assigned to the two DBSCAN clusters 94% (119/127) of the low Mg abundance cluster stars would be properly associated with the LMg population according to the by-eye definition, and 91% (64/70) of the stars assigned to the high Mg abundance cluster would be identified as HMg population stars. The remaining 163 stars lie in less densely populated regions of chemical space than the cores of the clusters and are thus unassigned to either of these clusters. Because of this, as was the case with the k-means clustering analysis, the two clusters found by DBSCAN that seem to correspond to the LMg and HMg populations are predominately populated at the higher metallicities of this sample ([Fe/H] $\gtrsim -1.5$), leaving the lower metallicity stars unassigned. While our adopted values of the DBSCAN N and ϵ parameters are not definitive (and indeed alternative pairings produce similar clusters as those shown in Figure 2.9), DBSCAN clustering analysis reveals that there is a density threshold that produces two distinct clusters with a manner of separation that is consistent with our initial separation in the [Mg/Fe]-[Fe/H] plane.

In summary, we find that the k-means and DBSCAN algorithms reaffirm our by-eye discrimination, and identify very similar clusters to those we identify as the LMg and HMg populations at the metallicities where we see the largest differences in chemical distributions. This is an objective affirmation that these populations are real, and that our method to separate them in a single projection of the [Mg/Fe]-[Fe/H] plane properly assigns 90% or more of stars to the correct population as compared to the results of clustering algorithms. While for simplicity we proceed with the use of a strict two-dimensional, Mg-based division of the two metal-poor populations, there will naturally be a small degree of cross-contamination (as we saw with the comparison to the k-means and DBSCAN results), due to some intrinsic overlap of these populations, the projection of a multi-dimensional distribution into two dimensions, and uncertainties blurring the intrinsic distribution of these populations. In the future, when truly large samples of multi-dimensional data are available for metal-poor stars, purer discrimination will be possible by looking at multiple chemical dimensions.

2.3.4 Kinematical Nature of the LMg and HMg Populations

While these two populations appear chemically distinct, they would be even more astronomically significant if they additionally exhibit different kinematics, which we can examine using the radial velocities of stars measured by APOGEE. We convert these radial velocity into the Galactic Standard of Rest system assuming a solar motion of $(V_r, V_\phi, V_z)_\odot = (14, 250, 7)$ km s^{-1} (Schönrich et al. 2010; Schönrich 2012).

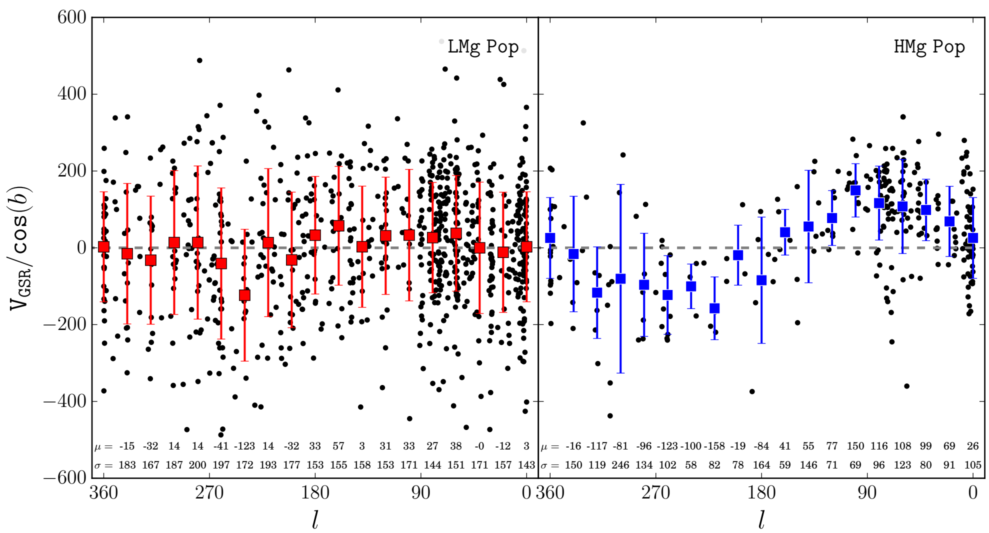

Fig. 2.10.— $V_{GSR}/\cos(b)$ vs. Galactic longitude for the LMg population (left) and the HMg population (right). The colored symbols represent the mean and population standard deviation calculated for 20° bins (the $l = 0° = 360°$ bin is repeated on either end), after applying a 3σ cut to remove stars with potentially errant velocities. The means and standard deviations of each bin are shown at the center of the bin at the bottom of the plot. Here we can see that the LMg population has an overall halo-like distribution of velocities, i.e. a large dispersion with little to no systemic rotation. The HMg population, on the other hand, appears to have a significant rotation with a much smaller dispersion.

Majewski et al. (2012) have shown the utility of the Galactic longitude-$V_{\rm GSR}/\cos(b)$ diagram for revealing stellar populations kinematically using only radial velocity data. $V_{\rm GSR}/\cos(b)$ is a proxy for the planar velocity of a star projected onto our line of sight, but breaks down at high Galactic latitudes (Majewski et al. 2012), so in this examination we only use stars with $|b| < 62^\circ$ (to include the stars in the APOGEE fields centered at $b = 60^\circ$).

Figure 2.10 shows that the distribution of $V_{\rm GSR}/\cos(b)$ vs. Galactic longitude for the LMg population has a large velocity dispersion (roughly 150-200 km s^{-1}, drawn from Figure 2.10) with very little to no net rotation, typical of that expected for a halo population. The HMg population, on the other hand, has a modest velocity dispersion of about 80-120 km s^{-1} around a significant trend of net rotation at the level of about 120-150 km s^{-1} (taken from the amplitude of the sinusoidal velocity variation displayed in ther right panel of Figure 2.10); the latter is consistent with the rotational velocity for the thick disk, at least at lower metallicities (Chiba & Beers 2000; Lee et al. 2011; Adibekyan et al. 2013; Allende Prieto et al. 2016). This is perhaps unsurprising, since chemically, the HMg population looks like an extension of the thick disk. Included in the HMg population are a few stars that have radial velocities more typical of halo-like kinematics, which may be halo stars with chemistry similar to the thick disk, or contamination from the LMg population.

Because the LMg population spans a wider range in metallicity than the HMg population and one would expect more stellar contribution from the halo (rather than the disk) towards lower metallicities, it is of interest to confirm that the above kinematical signatures persist even at the higher metallicity end of our samples. To do so, we examine $V_{GSR}/\cos(b)$ vs. Galactic longitude only for stars with metallicities [Fe/H] > -1.1 in each of these populations (Figure 2.11). Acknowledging the much smaller net samples, we still find that even the more metal-rich stars of the LMg exhibit halo-like motions, which further justifies that the LMg population is a coherent and distinct population from the dynamically colder HMg population.

2.4 Discussion

2.4.1 Relation to High-α and Low-α Halo Stars

Our analysis of the APOGEE database has focused on a very specific examination of a large sample of metal-poor stars making use of the clear separation seen in the [Mg/Fe]-[Fe/H] plane, a separation also validated in other chemical dimensions, like [Al/Fe]-[Fe/H] and [(C+N)/Fe]-[Fe/H], as well as in the overall 11-D chemical space (see Section 2.3.3). Previous studies of smaller samples of stars have demonstrated a split of halo stars into high- and low-α groups (Nissen & Schuster 2010, 2011; Navarro et al. 2011; Ramírez et al. 2012; Schuster et al. 2012; Sheffield et al. 2012; Jackson-Jones et al. 2014; Hawkins et al. 2015). These groups appear generally to correspond well with our HMg and LMg populations, as we now demonstrate.

In a study of the abundances of α-elements (Mg, Si, Ca, Ti), Na, Cr, and Ni for 94 kinematically and metallicity selected dwarf stars, Nissen & Schuster (2010) found two populations of stars with halo-like kinematics (total space velocities, $V_{\mathrm{tot}} > 180$ km s^{-1}) separated in the [Mg/Fe]-[Fe/H] plane. The population of halo stars with lower [Mg/Fe] also separated from the higher [Mg/Fe] ratio population in other α-elements (although to a lesser extent; Nissen & Schuster 2010; Ramírez et al. 2012; Hawkins et al. 2015), and other elements, such as (C+N), Na, Al, Ni, Cu, Zn, Y, and Ba, whereas little to no distinction was seen for other elements such as Cr and Mn (Nissen & Schuster 2010, 2011; Hawkins et al. 2015).

Figure 2.12 compares the chemistry of the APOGEE DR13 sample of this study to the stellar abundances presented in Nissen & Schuster (2010, 2011). We find general agreement for most elements, with perhaps small offsets between the two data sets in a few cases. The largest differences may be seen in the distribution of [Ca/Fe] ratios of the two populations seen here, which is likely due to the different methods of spectroscopic analysis employed by Nissen & Schuster (2010, 2011) and APOGEE. Nissen & Schuster (2010, 2011) measured abundances relative to two bright thick disk stars to achieve a high internal precision, but may be subject to systematic offsets compared to chemical abundance measurements using different methods, such as APOGEE's automated spectroscopic analysis. This difference in method of analysis, along with the use of differing spectral lines, model atmospheres, etc. may lead to the offsets seen in [Ca/Fe] ratios as well as those in other elements.

In addition to the chemical similarities between the low- and high-α halo stars and our HMg and LMg populations, there are kinematical similarities linking these groups of stars. Both the thick disk and high-α halo stars have (on average) higher rotational velocities than the low-α halo stars (Nissen & Schuster 2010), analogous to the kinematical differences seen between the HMg and the LMg populations here (see Figure 2.10). Thus, kinematics affirm that the low-α halo stars are members of the same population as the LMg population stars identified here, and that the high-α halo stars are part of the HMg population. While the LMg/low-α halo stars and HMg/high-α halo stars seem to be samples of the same respective populations, we maintain the usage of the names LMg and HMg to more explicitly reflect their selection through Mg abundances, the α-element that most easily distinguishes these populations.

It is interesting that there is such good agreement between the samples of stars in our work and Nissen & Schuster (2010, 2011), given the vastly different volumes sampled by each work. APOGEE surveys a large volume, allowing it to reach into the bulge or out into the halo. In contrast, Nissen & Schuster (2010, 2011) studied a sample of stars from the solar neighborhood, extending only as far as ~ 335 pc. The fact that both studies find similar distributions of stars suggests that they come from parent populations that, in terms of their distribution, do not vary significantly with position in the Galaxy. By concluding that the populations studied here are the same or related to those revealed by the high- and low-α halo stars (initially seen by Nissen & Schuster 2010), APOGEE uses its large statistical sampling to bring more clarity and significance to these two distinct populations.

2.4.2 Comparison to Milky Way Satellites

One possible origin for metal-poor stars in the MW is through the accretion of smaller, dwarf spheroidal (dSph) systems. As noted in the past (Venn et al. 2004; Tolstoy et al. 2009) dSph stars typically have lower α-element abundances than most MW stars at the same metallicities. However, at lower metallicities ([Fe/H] $\lesssim -1.5$) there is more overlap in [X/Fe] between the chemistry of MW and dSph stars. This suggests that, at least at higher metallicities, dSph stars from lower mass dwarf galaxies like those common around the Milky Way, are unlikely to contribute significantly to either the LMg or HMg populations. This does not, however, rule out the possibility that satellite galaxies could have contributed stars to our halo with different chemistry or that dSphs could have contributed stars at lower metallicities where the agreement is better.

The sample of dSph stars examined in some of these past studies come from multiple dSph galaxies. While this gives us an idea of the general spread of abundances across dSph satellites, it does not provide a picture of the chemical evolution within a given satellite. If we want to assess the dSph populations that are more likely to have been contributed to the MW, we should focus on the chemical evolution in more massive satellites, because previous studies (Bullock & Johnston 2005; Font et al. 2006) have found that satellites accreted earlier in the history of a galaxy are expected to be, on average, more massive. This is likely to have an impact on the chemistry of these satellites, because we might expect more massive satellites to have experienced more enrichment before Type Ia supernovae began to contribute their yields to the interstellar medium (e.g., due to higher star formation rates, higher star formation efficiency, better retention of supernovae products, etc.). This would have the effect of pushing the [α/Fe]-knee of these satellites to higher metallicities leading to potentially higher [α/Fe] ratios than less massive satellites for a given metallicity, and resulting in better agreement with the metal-poor stars seen in the MW at a given metallicity.

Although a few of these more massive satellites were somewhat represented in past studies, we wish to compare the APOGEE sample to a larger set of abundances from one of them, — the Fornax dSph — by examining the red giant abundances measured from high-resolution spectra by Letarte et al. (2010) and Lemasle et al. (2014). We also compare our APOGEE sample to the chemical abundances of Large Magellanic Cloud (LMC) red giants derived from high-resolution spectra by Van der Swaelmen et al. (2013) and of Sagittarius (Sgr) dSph and M54 stars measured from medium-resolution spectra by Mucciarelli et al. (2017). We show the of Mg and Ca abundance distributions for each of these systems in comparison to our APOGEE sample in Figure 2.13. These two chemical elements show trends where chemical abundance pattern differences appear to show up most distinguished either amongst

Milky Way populations or between satellites and the Milky Way.

The top panels of Figure 2.13 show that Fornax stars exhibit [Mg/Fe] ratios on the low side of the LMg population's chemical abundance pattern, except at the lowest metallicities where the agreement is better. On the other hand, the Fornax Ca abundances do not agree well with most of the stars observed by APOGEE and instead [Ca/Fe] ratios of Fornax stars are on average lower than those of both the LMg and HMg populations at all metallicities. In the distribution of heavy elements, we find that the differences between Fornax and LMg stars in Ni abundances are similar to that in Mg ([Ni/Fe] is slightly lower in Fornax by about a tenth of a dex on average), whereas their Cr abundance distributions differ more significantly like Ca ([Cr/Fe] is lower in Fornax by a couple tenths of a dex on average).

In contrast to Fornax, giants from the more massive LMC (shown in Figure 2.13) typically have higher [X/Fe] ratios. At metallicities [Fe/H] $\lesssim -1.0$, there is better agreement between the LMC giants and our LMg stars amongst their α-element and Fe-peak abundances, e.g., the distributions of [Mg/Fe] and [Ca/Fe] ratios shown in the middle panels of Figure 2.13. This may suggest that the metal-poor stars in our LMg population and the LMC have had analogous star formation histories, and ones that differ from both lower mass dSph satellites, and some of the more massive dSphs, such as Fornax. At higher metallicities [Fe/H] $\gtrsim -1.0$, the LMC giants look like a chemical extension of the LMg stars.

Unfortunately, one of the most massive dSphs and therefore interesting satellites to compare with our Mg populations, the Sgr dSph, has been observed by APOGEE, but has been mostly excluded from our own sample by the stellar surface temperature restriction $T_{\rm eff} > 4000$ K. So that we maintain as self-consistent a sample as possible, the latter requirement removes the coolest and brightest red giants from our sample, which have been analyzed by ASPCAP using a different grid of model atmospheres. These infrared-bright stars, however are the only type of red giants that APOGEE has accessed and have data available to analyze in Sgr (e.g., Majewski et al. 2013; Hasselquist et al. 2017) because of the large distances to this dSph. For the same reason, but also because these younger stars are the dominant red giant population in the system, most other chemical abundance studies of the Sgr dSph also typically observe Sgr's more metal-rich stars (e.g., Sbordone et al. 2007; Hasselquist et al. 2017). Nevertheless, while this younger, more metal-rich Sgr dSph population is not directly comparable to our more metal-poor populations, it has been noted to resemble a chemical extension of the low-α metal-poor stars in the MW (Hasselquist et al. 2017) – i.e., our LMg population.

A new study of the Sgr dSph, by Mucciarelli et al. (2017) appears to bear out this suggestion. Using abundances of α-elements measured from medium-resolution spectra, these authors show that both Sgr dSph and M54 stars (located at the center of the Sgr dSph) have similar α-element chemical abundance patterns to LMC stars. As may be seen in the bottom panels of Figure 2.13, and as is the case of LMC stars, there is an overlap in Mg and Ca abundances of the Mucciarelli et al. (2017) Sgr dSph and M54 stars with the LMg population (and to a smaller extent, the HMg population).

2.4.3 Potential Origins

As discussed above, the present dSph satellites of the MW typically have α-element abundances that are too low to explain the origin of most MW stars observed by APOGEE (and even the halo stars shown in Venn et al. 2004; Tolstoy et al. 2009), at metallicities [Fe/H] $\gtrsim -1.5$, where we are interested in exploring the origin of the

LMg and HMg populations. This is demonstrated in our comparison with dSph stars in past studies and in our comparison with Fornax in Figure 2.13. The one possible exception is the Sgr dSph, for which the dominant population looks like a possible metal-rich extension of the LMg population (Sbordone et al. 2007; Carretta et al. 2010; Hasselquist et al. 2017).

Even if Sgr dSph stars may look more chemically similar to the LMg (as is being revealed by larger samples that push to lower metallicities, see Mucciarelli et al. 2017), it seems unlikely that this particular satellite could have contributed the majority of the LMg stars. This is evidenced by the full sky coverage of the LMg population with halo-like kinematics, whereas the Sgr dSph and its tidal tails are confined roughly to a plane in the sky (Majewski et al. 2003; Law & Majewski 2010). Thus the majority of the LMg population (and HMg population, which has still higher α-element abundances) does not seem to be accounted for by the accretion of dSph satellites like most of those around the MW now, particularly at higher metallicities, [Fe/H] $\gtrsim -1.5$.

As mentioned above, ΛCDM predictions, however, suggest that galaxies accreted earlier in the history of our Galaxy will tend to be more massive, resulting in higher [α/Fe] ratios than those being accreted today, for stars of the same metallicity (Font et al. 2006; Lee et al. 2015). Additionally, cosmological hydrodynamical simulations including chemical evolution have reported complex scenarios where some of the accreted satellites could continue star formation activity in a bursty mode, producing stellar populations with a variety of levels of α-element enrichment (e.g., Font et al. 2006; Tissera et al. 2012). The variation in the assembly histories of MW-mass galaxies has been shown theoretically to then shape the chemical patterns of their stellar halos (Font et al. 2006; Tissera et al. 2013).

Fernández-Alvar et al. (2017a), using APOGEE data combined with distances, found that the innermost regions of the Galactic halo are dominated by stars with higher [α/Fe] ratios, but that dominance shifts to stars with lower [α/Fe] ratios at larger distances, at least for the moderately metal-poor regime probed by APOGEE (i.e., stars with [Fe/H] $\gtrsim -2$). This [α/Fe] variation supports the idea that more massive satellites with faster enrichment or star formation, and thus higher [α/Fe] ratios, may have been accreted earlier in the history of the MW to help form the inner regions of the halo.

The lower [α/Fe] ratios of our LMg population compared to the metal-poor end of the thick disk, yet higher [α/Fe] ratios than current MW dSph satellites may then be evidence that these stars have been accreted from more massive dwarf systems early in the history of the MW. Alternatively the LMg population may have originated from regions in the early MW halo with star formation similar to what would be expected in more massive dwarf galaxies. It is interesting that the LMg population, a potentially accreted population, is a significant fraction of the metal-poor stars observed by APOGEE, at least between metallicities of about -1.5 and -0.9.

Fishlock et al. (2017) recently presented a study that examined neutron capture element abundances in stars selected from (Nissen & Schuster 2010). They found that in terms of light and heavy s-process elements (*ls* and *hs* respectively) the low-α halo stars have higher [*hs*/*ls*], which affirms results from Nissen & Schuster (2011), who found similar differences in [Ba/Y] (Ba is an *hs*- and Y an *ls*-element). Fishlock et al. (2017) also found differences between these two populations in terms of their ratios of Y to Eu (an r-process element) and ratios of other s-process elements to Eu. This is significant because the low [Y/Eu] ratios exhibited by the low-α halo stars, along with high [Ba/Y] ratios, are signatures seen in dSph stars, so that these neutron capture element patterns further support the accretion origin for the equivalent of our LMg population.

These conclusions are in agreement with those that have been drawn for the origin of low-α halo stars (Nissen & Schuster 2010; Sheffield et al. 2012; Hawkins et al. 2015), with which the LMg population seems to be associated. In addition to exhibiting lower abundances of α and other elements (Nissen & Schuster 2010, 2011; Sheffield et al. 2012; Hawkins et al. 2015), low-α halo stars have been shown to have ages typically 2-3 Gyr younger than high-α halo and thick disk stars at any given metallicity, as well as larger orbital radii and distances from the Galactic mid-plane (Schuster et al. 2012). Additionally, Schuster et al. (2012) found that the low-α halo stars they observed had larger eccentricities, clumped at values greater than 0.85 (i.e., $0.85 \lesssim e \lesssim 1.0$), whereas the observed high-α halo stars exhibit a greater spread in eccentricities ($0.4 \lesssim e \lesssim 1.0$). The results of these and various other studies lend further support to the hypothesis that the low-α halo stars have been accreted.

In contrast to the likely accretion origin for the LMg, the HMg populations's apparent net rotation and chemical similarity to the thick disk suggest an *in situ* formation similar or related to that of the thick disk. If so, the HMg population might simply be a metal-poor extension of the thick disk, and the two may share an origin, whether through (1) dissipative collapse (Majewski 1993b), (2) radial migration (Sellwood & Binney 2002, note, however, that several recent simulations suggest that radial migration does not sufficiently heat the disk of the Galaxy — cf. Minchev et al. 2012; Vera-Ciro et al. 2014), or (3) by being "kicked out" or heated from initially colder orbits (possibly in the bulge or the colder disk) into more halo-like orbits by multibody encounters or the accretion of satellites (possibly even those that contributed the accreted halo stars; Quinn et al. 1993; Walker et al. 1996; Nissen &

Schuster 2010; Schuster et al. 2012; Sheffield et al. 2012; Johnston 2016).

Another possibility, proposed by Hawkins et al. (2015), based on the chemical similarities between high-α halo stars and the thick disk, is that there may be a smooth transition between what they call the "canonical halo" and the thick disk, both of which they suggest formed *in situ*. The HMg population might then represent an intermediate, transitional stage between these two populations. Because the HMg population has chemical abundance patterns similar to the thick disk, but with a lower apparent net rotation than the thick disk, it may be related to the MWTD reported by Chiba & Beers (2000) and Beers et al. (2002). If these two populations are the same, or are related, this would further support an *in situ* formation of the HMg population, as was proffered as the potential origin of the MWTD.

The bifurcation of properties in metal-poor stars is reminiscent of the classic bimodality in Horizontal Branch (HB) types of the "Younger Halo" and "Old Halo" globular clusters between metalliticities $-1.8 <$ [Fe/H] < -0.8, which were thought to have been accreted from satellites and formed *in situ* respectively (Zinn 1993, 1996)[2]. While these globular cluster populations are no longer thought to be distinct in age alone (due to complications in the differences between HB types; Gratton et al. 2010), recent studies have found that there are two distinct age-metallicity relations amongst globular clusters (VandenBerg et al. 2013; Leaman et al. 2013; Wagner-Kaiser et al. 2017) that cover similar age ranges, with the more metal-poor branch being about 2 Gyr younger than the metal-rich branch for a given metallicity. In this paradigm, the more metal-poor and distant clusters are thought to have been accreted, whereas the more metal-rich clusters with more disk-like kinematics would have formed *in situ*.

[2]At lower metallicities, [Fe/H] < -1.8, Zinn (1996) identifies a third group of metal-poor globular clusters that are spatially and kinematically distinct from the other two globular cluster populations, similar to the three-part division we found in metal-poor stars with the k-means clustering algorithm (Section 2.3.3).

With this picture of dual origins for globular clusters, it appears that both globular clusters and field stars separate consistently into *in situ* and accreted populations.

Putting the HMg and LMg populations within the context of prior studies of the thick disk and halo of the MW would benefit from the addition of full kinematics and spatial information for the APOGEE sample. With the Gaia satellite about to deliver parallaxes and proper motions for stars at these magnitudes, this will soon be a reality.

2.5 Conclusions

We detect evidence for two distinct populations of metal-poor stars observed by APOGEE, discriminated by their [Mg/Fe]. We study the chemistry and kinematics of these populations, and find multiple differences in their properties. The separation between these populations in [Mg/Fe] is more pronounced for metallicities [Fe/H] $\gtrsim -1.5$. While these populations are also distinguished by the patterns of other α-elements, their distinctiveness is less apparent for heavier α-elements such as Ca. This variation in chemical separation may reflect some of the finer details of the differing nucleosynthetic processes forming these two populations such as the differential production and contribution of α-elements in Type Ia supernovae or in Type II supernovae of different masses or metallicities (Tsujimoto et al. 1995; Nomoto et al. 2013). In addition to the α-element differences, the LMg and HMg populations are distinct in their C+N, Al, and Ni abundances relative to Fe. While our selection of the two populations used a by-eye discrimination in [Mg/Fe]-[Fe/H] space, we have also used two different clustering algorithms to search for distinct groupings in an 11-dimensional APOGEE chemical space. Both of these methods generally reproduce our original selection and identify essentially the same two populations apparent in the [Mg/Fe]-[Fe/H] plane.

We show that the LMg population exhibits halo-like kinematics, with little rotation and a large velocity dispersion of about 150-200 km s^{-1}. The HMg population appears to be kinematically colder, with a rotational velocity $\sim$ 120-150 km s^{-1} and smaller velocity dispersion around 80-120 km s^{-1}. This HMg population, however, includes some stars with radial velocities more consistent with halo-like orbits, similar to those found in other studies such as Nissen & Schuster (2010), and may reflect a chemical overlap between the LMg and HMg populations or a history tied to the formation of the thick disk (given the similarity between the chemistries of the HMg population and the thick disk).

Previous studies have also reported the detection of α-element abundance differences in metal-poor stars, with some making selections specifically in Mg, as performed here (Nissen & Schuster 2010; Navarro et al. 2011; Ishigaki et al. 2012; Sheffield et al. 2012; Jackson-Jones et al. 2014; Hawkins et al. 2015), albeit with fewer stars. The advantage of our study is that we rely on a large sample of stars that have homogeneously determined abundances for many chemical species. In addition, our sample is much larger in size, even at low metallicities, [Fe/H] < -1.0, where we have more than 1000 stars, which more than doubles the sample in Jackson-Jones et al. (2014), the largest of these studies. Our analysis is of a sample that is free from kinematical biases, and probes a larger volume of the MW. Finally, both by visual inspection and through the results of more sophisticated clustering algorithms, we are able to identify and separate the two distinct populations noted in past studies with greater statistical significance and reliability than before.

From the chemistry and kinematics of these two populations, we conclude that our LMg population is likely an accreted population of halo stars, formed in conditions similar to those in early dwarf galaxy satellites. Examining the elemental abundance patterns of dSph stars (from Venn et al. 2004; Letarte et al. 2010; Lemasle et al. 2014), we find that our LMg population stars have generally higher [α/Fe] ratios for stars with metallicities [Fe/H] $\gtrsim -1.5$. Thus it appears that if these stars (at least the more metal-rich LMg stars) were accreted earlier in the history of the MW, they were likely accreted from more massive satellites than present dSphs (Font et al. 2006).

Our HMg population, from its chemistry and its slow but significant net rotation, appears to contain mostly stars in the metal-poor end of the thick disk and/or may be related to the potentially distinct component of the MW, the MWTD (Chiba & Beers 2000; Beers et al. 2002). Within this population, there are also stars that may have halo-like kinematics but chemistry similar to thick disk stars. This would be consistent with the similarities between the Nissen & Schuster (2010, 2011) thick disk and halo high-α stars, who suggest that the high-α halo stars (or equivalently our HMg stars with halo kinematics) may also be part of the dissipative component that also formed the thick disk. This is similar to the picture presented by Sheffield et al. (2012) who suggested that these stars could be *in situ* stars formed in such a dissipative collapse, or could be stars from the thick disk that were kicked into halo orbits. The HMg population may then represent a combination of these possibilities.

Measuring more properties of the stars in these two populations may help us further distinguish them, provide more clues to their origins, and/or identify more sub-populations. The origin of Eu in the low-α halo stars (LMg population) seen by Fishlock et al. (2017) is still not understood, and its relative abundance to s-process elements cannot be accounted for by the slow enrichment and low mass (1-3 $M_{\odot}$) AGB pollution Fishlock et al. (2017) authors use to explain the differences in *ls* and *hs* abundances in these stars. Thus, as they suggest, further study of these populations with more r-process elements and larger samples may provide a better picture of the chemical evolution of metal-poor stars.

Expanded three-dimensional velocities would greatly expand our ability to study the kinematics and dynamics of the stars in these populations, but will require proper motions. As suggested by Navarro et al. (2011) and Schuster et al. (2012), the three-dimensional motions of stars in the low-α halo population provide evidence for accretion, so space motions would allow us to perform similar analysis with the populations seen in APOGEE. Additionally, full space motions may help separate populations that have distinct kinematics but similar chemistry. The physical distribution of the MW stars in our defined populations will be aided by incorporating accurate distance measurements (an initial study of the distribution of metal-poor stars in APOGEE is given in Fernández-Alvar et al. 2017a). Finally, the companion paper by Fernández-Alvar et al. (2018), further explores the chemical evolution of the two distinct metal-poor LMg and HMg populations identified in APOGEE.

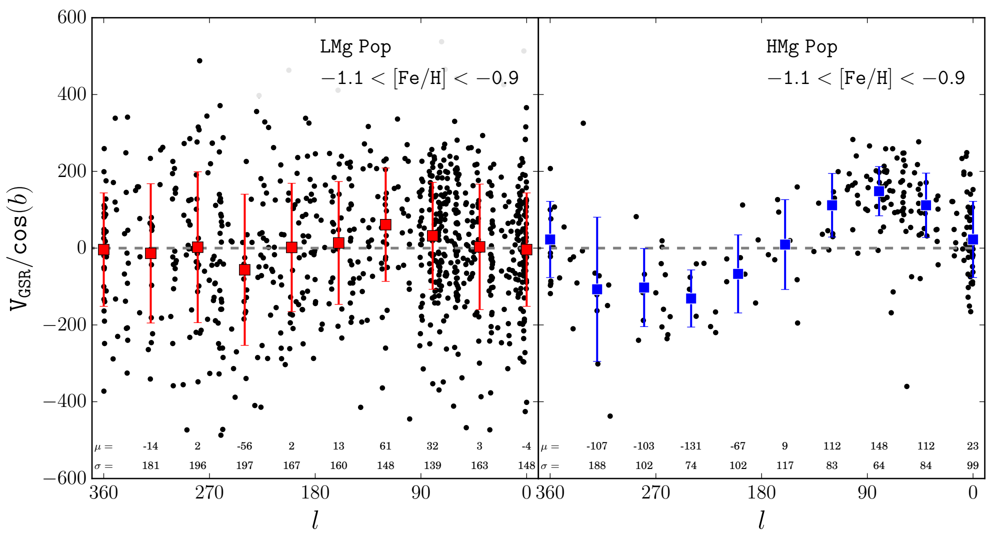

Fig. 2.11.— Same as Figure 2.10, with data binned into 40° bins, for LMg and HMg stars with $-1.1 < [\mathrm{Fe/H}] < -0.9$. The more metal-rich ends of these populations follow the same kinematical trends as the subsamples covering the larger metallicity range shown in Figure 2.10.

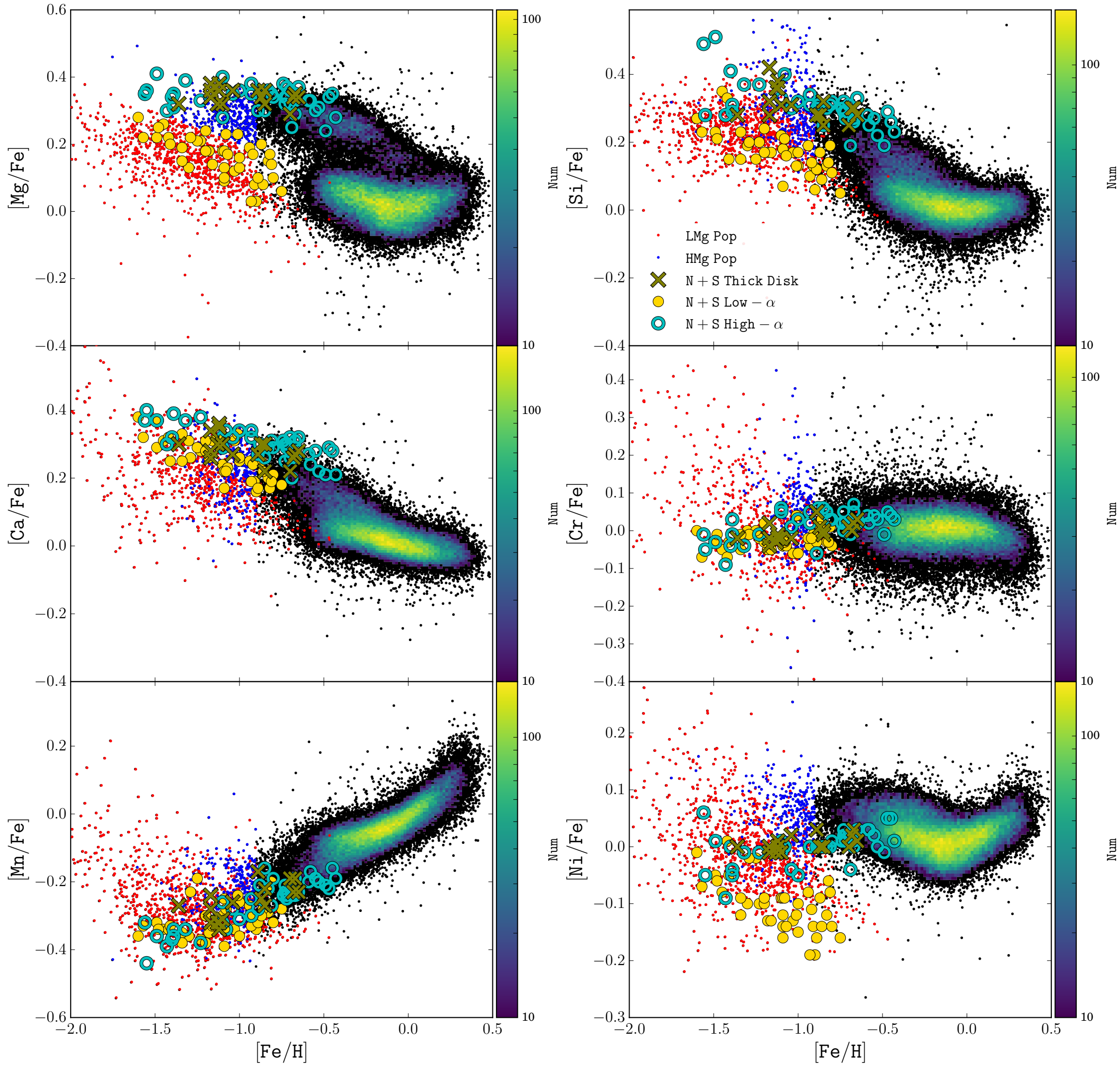

Fig. 2.12.— Distribution of [X/Fe] with [Fe/H] for Mg, Si, Ca, Cr, Mn, and Ni with 2D histogram of the densely distributed stars as done in Figure 2.1. Stars of LMg and HMg populations are color-coded the same as in Figure 2.3. Over-plotted are data from Nissen & Schuster (2010, 2011) color-coded to identify kinematically selected thick disk stars (olive green crosses), and their chemically selected high-α (cyan open circles) and low-α (yellow filled circles) halo stars.

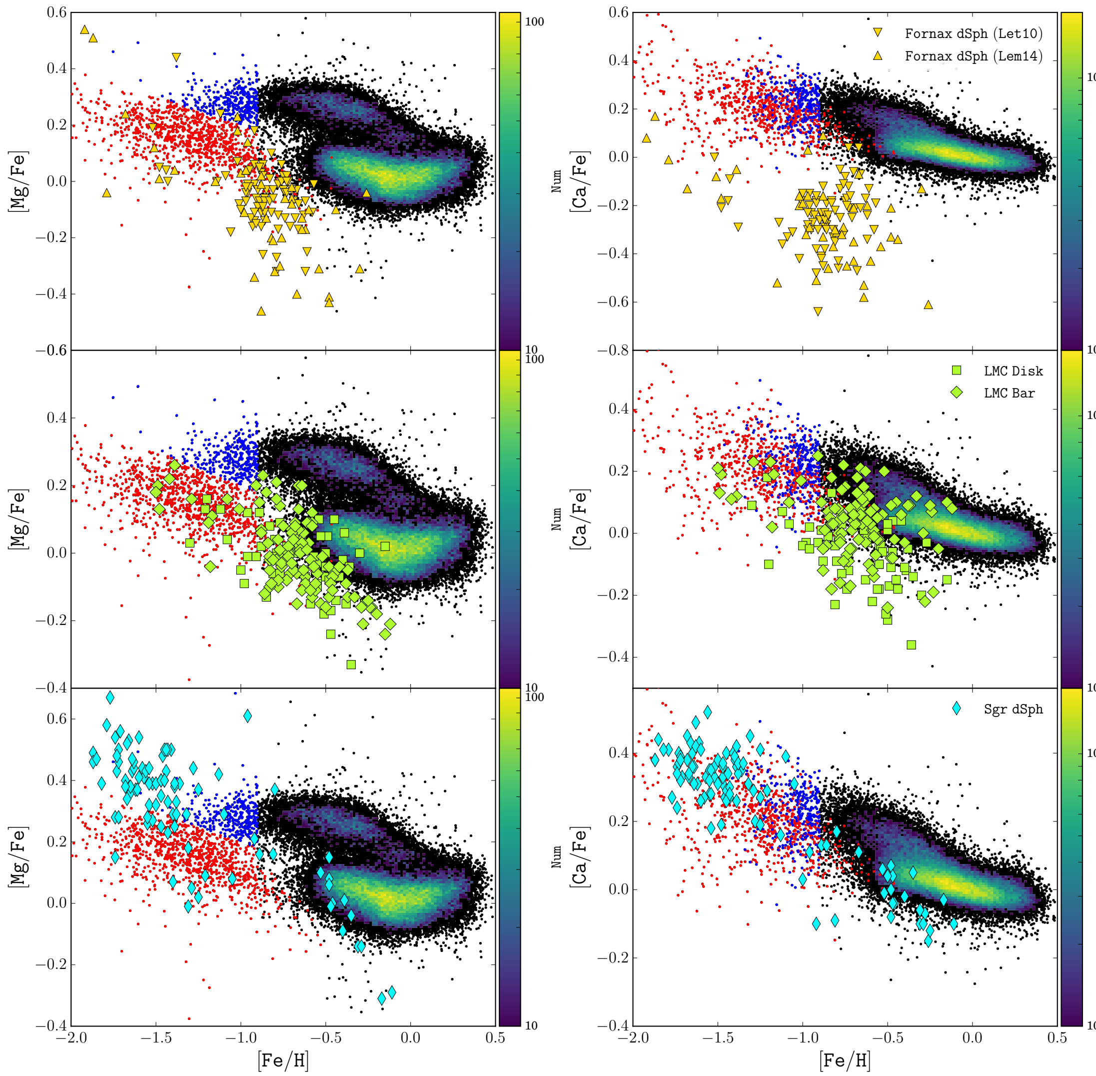

Fig. 2.13.— Distribution of [X/Fe] with metallicity for Mg (left) and Ca (right). Stars of the LMg and HMg populations are color-coded the same as in Figure 2.3. Over-plotted are abundances of (Top) Fornax dSph stars reported by Letarte et al. (2010, yellow downward triangles) and Lemasle et al. (2014, yellow upward triangles), (Middle) LMC disk (green squares) and bar (green wide diamonds) stars from Van der Swaelmen et al. (2013), and (Bottom) Sgr dSph and M54 stars (cyan narrow diamonds) reported by Mucciarelli et al. (2017).

Chapter 3

Disk-Like Chemistry of the Triangulum-Andromeda Overdensity

Summary

The nature of the Triangulum-Andromeda (TriAnd) system has been debated since the discovery of this distant, low-latitude Milky Way (MW) overdensity more than a decade ago. Explanations for its origin are either as a halo substructure from the disruption of a dwarf galaxy or a distant extension of the Galactic disk. We test these hypotheses using chemical abundances of a dozen TriAnd members from the Sloan Digital Sky Survey's 14th Data Release of Apache Point Observatory Galactic Evolution Experiment (APOGEE) data to compare to APOGEE abundances of stars with similar metallicity from both the Sagittarius (Sgr) dSph, and the outer MW disk. We find that TriAnd stars are chemically distinct from Sgr across a variety of elements, (C+N), Mg, K, Ca, Mn, and Ni, with a separation in [X/Fe] of about

0.1 to 0.4 dex depending on the element. Instead, the TriAnd stars, with a median metallicity of about −0.8, exhibit chemical abundance ratios similar to those of the lowest metallicity ([Fe/H] ~ -0.7) stars in the outer Galactic disk, and are consistent with expectations of extrapolated chemical gradients in the outer disk of the MW. These results suggest that TriAnd is associated with the MW disk, and, therefore, that the disk extends to this overdensity — i.e., past a Galactocentric radius of 24 kpc — albeit vertically perturbed about 7 kpc below the nominal disk midplane in this region of the Galaxy.

3.1 Introduction

Several overdensities discovered towards the outer disk of the Milky Way (MW) have origins that are still not understood, including "Triangulum-Andromeda" (TriAnd, Majewski et al. 2004; Rocha-Pinto et al. 2004), which is a low-latitude, distant (~ 20 kpc), and kinematically cold ($\sigma_{\rm LOS} \sim 25$ km s^{-1}) cloud of stars (Sheffield et al. 2014). Theories to explain TriAnd's observed properties include that it (1) could be tidal debris from a disrupted dwarf galaxy (Deason et al. 2014; Sheffield et al. 2014), or (2) represents part of an extended and perturbed MW disk, perhaps a trough in a series of midplane oscillations (Price-Whelan et al. 2015; Xu et al. 2015; Li et al. 2017). Recent simulations have illustrated that large, non-axisymmetric, vertical oscillations can be excited in the outer disk due to the interaction of the Sagittarius dwarf spheroidal galaxy (Sgr dSph) with the MW; reproducing structures reminiscent of TriAnd (and other overdensities; Laporte et al. 2018). These differing origin scenarios should impart different chemical signatures to TriAnd stars. For example, if TriAnd is the result of a perturbation to the outer Galactic disk, its chemical abundance patterns should resemble that of known outer disk stars, whereas tidal debris should share the chemistry seen in dwarf galaxies.

To date, chemical studies of TriAnd have reached differing conclusions about its origin. The first high-resolution spectroscopic study of TriAnd stars by Chou et al. (2011) focused on the elements Ti, Y, and La, and found TriAnd had some chemical differences from MW disk stars in the solar neighborhood, and suggested a dwarf galaxy origin. On the other hand, recent study of O, Na, Mg, Ti, Ba, and Eu abundance ratios in TriAnd stars indicate that it is chemically consistent with the MW disk rather than a dwarf galaxy (Bergemann et al. 2018). Further chemical study of TriAnd to resolve such discrepancies is clearly warranted.

The Apache Point Observatory Galactic Evolution Experiment (APOGEE, Majewski et al. 2017) provides such an opportunity. APOGEE is a high-resolution ($R \sim 22,500$) spectroscopic survey of Galactic stellar populations with H-band sensitivity well-suited to the exploration of highly extinguished low-latitude targets, such as the TriAnd overdensity and the outer disk. Selecting from the ∼263,000 stars observed with the SDSS 2.5-m telescope (Gunn et al. 2006) and analyzed by APOGEE in the 14th Data Release (DR14, Abolfathi et al. 2018) of the Sloan Digital Sky Survey-IV (SDSS-IV, Blanton et al. 2017), we use the abundances of six APOGEE-measured elements to compare TriAnd red giants to outer disk and Sgr dSph stars, and demonstrate that the TriAnd chemistry is more consistent with an extrapolation of outer MW disk chemical gradients than the abundance patterns of a prototypical dwarf galaxy of similar enrichment.

3.2 Data

Details of the APOGEE survey and data reduction pipeline can be found in Majewski et al. (2017) and Nidever et al. (2015), respectively. Here we use the SDSS-IV DR14 calibrated stellar parameters and chemical abundances derived from the APOGEE Stellar Parameter and Chemical Abundance Pipeline (ASPCAP; García Pérez et al. 2016). To insure that we are considering the most reliably determined stellar parameters, we remove stars flagged[1] with the STARFLAGS BAD_PIXELS, VERY_BRIGHT_NEIGHBOR, or LOW_SNR set, or any stars with the ASPCAPFLAGS, ROTATION_WARN or STAR_BAD. We also restrict analysis to stars with small visit-to-visit velocity scatter, $V_{\rm scatter} \leq 1$ km s^{-1}, low velocity uncertainty, $V_{\rm err} \leq 0.2$ km s^{-1}, and S/N > 80, to remove stars whose ASPCAP-analyzed spectra may be of lower quality. Finally, we focus on stars in effective temperature ranges, between 3700 K and 5500 K, where stellar parameters and chemical abundances are reliably and consistently determined.

In this high-quality sample, we have 12 M giants that were identified by Sheffield et al. (2014) as TriAnd members from their photometry and cold kinematics ($\sigma \sim 25$ km s^{-1}) and were deliberately targeted in APOGEE-2 (Zasowski et al. 2017). The APOGEE-measured properties of these TriAnd stars are given in Table 3.1. Several studies have suggested that TriAnd may separate into two features, TriAnd1 and TriAnd2, that coincide on the sky but lie at photometrically determined heliocentric distances $\sim$ 20 kpc and $\sim$ 28 kpc, respectively (Martin et al. 2007). However, since these features were shown to overlap considerably in spectrophotometric distance, radial velocity, and metallicity (Sheffield et al. 2014), and we only have two stars classified as TriAnd2 members, we treat them here as a single overdensity. For a comparison, we use Sgr dSph because this dwarf galaxy is sufficiently enriched to have a considerable M giant population, like TriAnd. To do so, we use a set of 69 Sgr dSph members confirmed by Hasselquist et al. (2017) and satisfy our quality criteria.

We also compile a representative comparison sample of outer disk stars from

[1] A description of these flags can be found in the online SDSS DR14 bitmask documentation (`http://www.sdss.org/dr14/algorithms/bitmasks/`)

Table 3.1. Properties of TriAnd Stars

Column	Column Label	Column Description
1	APOGEE	APOGEE Star ID
2	RAdeg	Right Ascension (decimal degrees)
3	DEdeg	Declination (decimal degrees)
4	GLON	Galactic Longitude (decimal degrees)
5	GLAT	Galactic Latitude (decimal degrees)
6	Jmag	2MASS J magnitude
7	Hmag	2MASS H magnitude
8	Kmag	2MASS Ks magnitude
9	Dist	Heliocentric distance (kpc)
10	e_Dist	Uncertainty in distance (kpc)
11	HRV	Heliocentric radial velocity (km s^{-1})
12	e_HRV	Radial velocity uncertainty (km s^{-1})
13	Teff	Effective surface temperature (K)
14	e_Teff	Uncertainty in $T_{\rm eff}$ (K)
15	logg	Surface gravity
16	e_logg	Uncertainty in $\log g$
17	Vturb	Microturbulent velocity (km/s)
18	Vmacro	Macroturbulent velocity (km/s)
19	[Fe/H]	Log abundance, [Fe/H]
20	e_[Fe/H]	Uncertainty in [Fe/H]
21	[CN/H]	Log abundance, [(C+N)/Fe]
22	e_[CN/H]	Uncertainty in [(C+N)/Fe]
23	[Mg/Fe]	Log abundance, [Mg/Fe]
24	e_[Mg/Fe]	Uncertainty on [Mg/Fe]
25	[K/Fe]	Log abundance, [K/Fe]
26	e_[K/Fe]	Uncertainty on [K/Fe]
27	[Ca/Fe]	Log abundance, [Ca/Fe]
28	e_[Ca/Fe]	Uncertainty on [Ca/Fe]
29	[Mn/Fe]	Log abundance, [Mn/Fe]
30	e_[Mn/Fe]	Uncertainty on [Mn/Fe]
31	[Ni/Fe]	Log abundance, [Ni/Fe]
32	e_[Ni/Fe]	Uncertainty on [Ni/Fe]

Note. — Table 3.1 is published online in Hayes et al. (2018b). The columns are shown here for guidance regarding its form and content.

Note. — Null entries are given values of -9999.

APOGEE. To do so, we use spectrophotometric distances calculated by Queiroz et al. (2018) using DR14 ASPCAP stellar parameters and their Bayesian `StarHorse` code. Because not all of these distances are reliable, we only use stars that are not flagged with HIGH_EXTINCTION_WARN, NUMMODELS_BAD, or EXTINCTION_BAD_BRIGHT2MASS, which may have erroneous distance estimates due to poor extinction corrections or lack available stellar models to determine a reliable distance. Because we will determine metallicity and chemical gradients in the outer disk to compare to the chemistry of TriAnd stars, we also want stars with relatively accurate `StarHorse` distances, and remove stars with $\sigma_d > 0.5$ kpc on their posterior distance distribution. These distances are converted to Galactocentric coordinates assuming $R_{\mathrm{GC},\odot} = 8$ kpc, and the Galactic distribution of these APOGEE stars is shown in Figure 3.1, along with the TriAnd stars with `StarHorse` distances. Finally, we form our "outer disk sample" from this high-quality set of MW stars by selecting those with cylindrical Galactocentric radii $R_{\mathrm{GC}} > 9$ kpc and midplane distances $|Z| < 1.0$ kpc.

3.3 Results and Analysis

Using the reliable spectrophotometric distances from `StarHorse`, our TriAnd sample (with median distance uncertainties of 2 kpc) is centered at a median distance of $\sim$18 kpc with a 1σ spread of 4 kpc. This is consistent with past distances found for TriAnd, e.g., the 18.2 kpc distance (Sheffield et al. 2014) used to select the "TriAnd1" members that dominate our sample here. This puts the TriAnd sample at a median Galactocentric radius of $\sim$24 kpc (1-σ_{R} spread of 4 kpc) and below the disk by $\sim$7 kpc (1-σ_{Z} spread of 1 kpc).

While a few of the TriAnd stars do not have reliable spectrophotometric distances from `StarHorse`, they were selected by Sheffield et al. (2014) in color-magnitude to fall along the red giant branches of 8 Gyr/10 Gyr $-0.8/-1.0$ metallicity isochrones at heliocentric distances around 18.2 kpc/27.5 kpc for TriAnd1/TriAnd2. Figure 3.2 shows that TriAnd stars have effective temperatures and surface gravities of cool red giants, supporting the isochrone-based distances used by Sheffield et al. (2014).

As shown below, we can perform a more robust analysis by comparing to a large sample of outer disk stars spanning a considerable range of Galactocentric radii. To achieve this, we have not restricted the outer disk sample to cover the T_{eff} and $\log g$ range of the TriAnd and Sgr dSph samples. However, to ensure that this does not affect our chemical abundance comparison, we examined the abundance distributions of relevant chemical elements for outer disk stars warmer and cooler than 4250 K to verify that there were no significant differences in their abundance patterns at a level that affects our conclusions about TriAnd. Because our TriAnd and Sgr dSph samples cover nearly the same stellar parameter space, their comparison should be even more robustly reliable.

Despite its large size (21,868 stars), our APOGEE-based disk sample (targeted to minimize selection biases; Zasowski et al. 2013, 2017) does not extend to the distance of the TriAnd stars and has few stars beyond $R_{\mathrm{GC}} > 15$ kpc. However, if the abundances of Galactic disk stars follow relatively well-behaved radial metallicity and chemical gradients, we can extrapolate those trends to establish the abundances expected for the disk at the distance of TriAnd. To illustrate this, Figure 3.3 shows the [Mg/Fe]-[Fe/H] plane for outer disk stars with [Mg/Fe] and [Fe/H] uncertainties less than 0.1 dex, subdivided into samples lying within 1 kpc wide annuli spanning Galactocentric radii from $R_{\mathrm{GC}} = 9$ kpc to 15 kpc. Within each annulus we calculate the median abundance of the outer disk sample, and can see that there are clear trends in both [Fe/H] and [Mg/Fe] with Galactocentric radius.

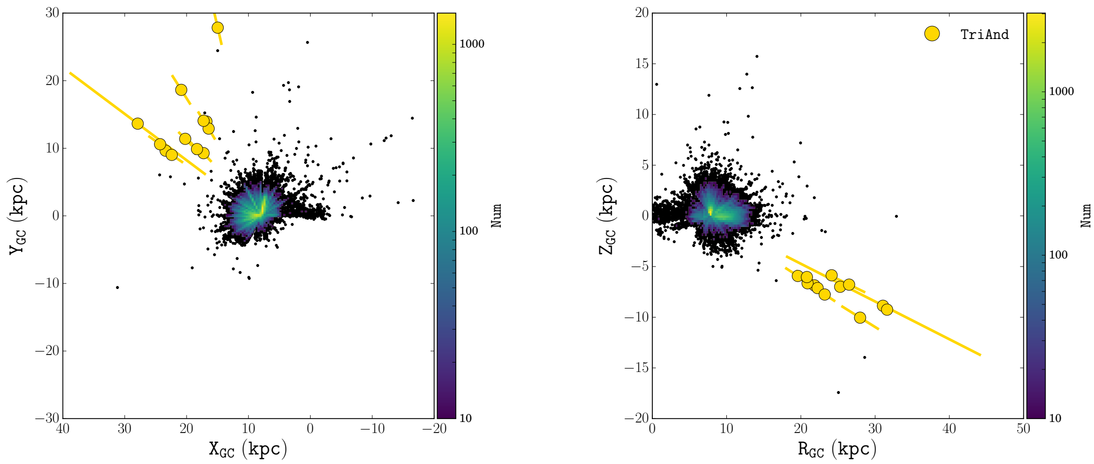

Fig. 3.1.— Spatial distribution of the high-quality APOGEE stars (before outer disk selection, black points) and TriAnd stars (gold circles), showing the reported 1σ distance uncertainty for the TriAnd stars. (left) Stellar distribution projected onto the Galactic plane. (right) Distribution azimuthally collapsed onto the cylindrical $R_{\rm GC}$-$Z_{\rm GC}$ plane.

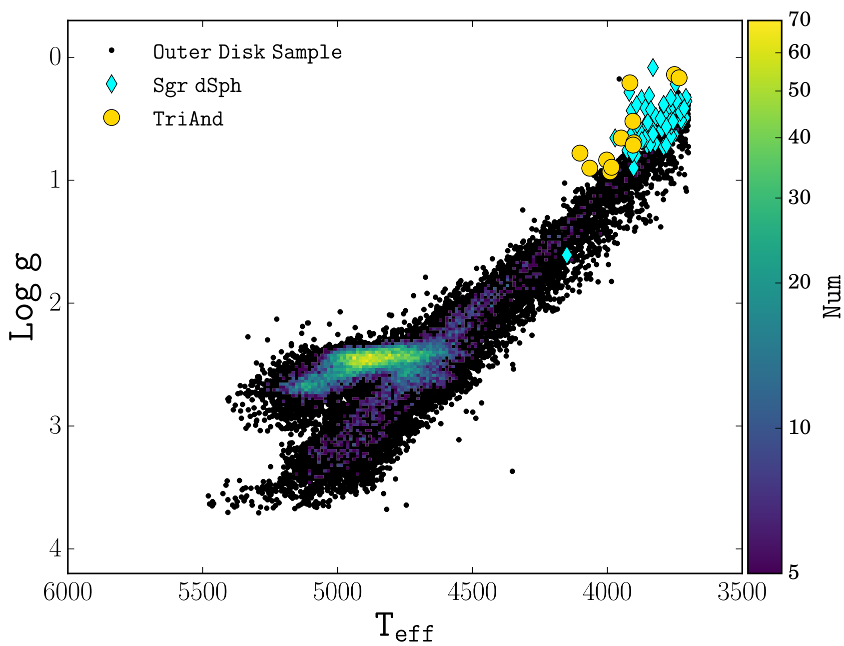

Fig. 3.2.— Spectroscopic HR diagram of APOGEE-derived $\log g$ versus $T_{\rm eff}$ for the outer disk (black points with a 2D histogram where densely populated), TriAnd (gold circles), and Sgr dSph (cyan diamonds) samples.

Figure 3.3 strikingly demonstrates that the [Mg/Fe]-[Fe/H] distribution for TriAnd stars occupies a region of this parameter space consistent with a metal-poor extrapolation of the outer disk trend to larger radius. Moreover, the TriAnd stars are enhanced in [Mg/Fe] relative to Sgr dSph stars of similar metallicity.

APOGEE enables similar comparisons of these samples in multiple chemical dimensions. Figure 3.4 presents the chemical abundance distributions of the TriAnd, outer disk, and Sgr dSph samples (showing only stars with both σ[X/Fe] and σ[Fe/H] < 0.1 dex) for a set of elements are formed in a variety of nucleosynthetic processes: the α-elements Mg and Ca, the odd-Z element K, the iron-peak elements Mn and Ni, and the sum of C and N (surface abundances of C and N are altered during dredge-up and mixing in red giants, but their sum is effectively conserved; see Martig et al. 2016, and references therein). This subset of APOGEE-measured elements were specifically chosen because they do not exhibit different abundance trends in warm and cool outer disk stars, and are measured with low uncertainties.

In these other chemical planes, as in Figure 3.3, the TriAnd stars tend to overlap and extend the sequence of the outer disk stars at metallicities of [Fe/H] $\sim$$-0.7$. Moreover, the radial gradient of the outer disk, as measured by the median chemistry in 1 kpc annular rings (also as in Figure 3.3), approaches the chemical abundances of TriAnd stars at increasing radii. We can extrapolate these trends to the distance of TriAnd to estimate the expected abundances for outer disk stars at that location. While the shape of the [X/Fe]-[Fe/H] distribution of the outer disk sample is complex within each annulus, as seen in Figure 3.3, the median chemistry of the distributions varies roughly linearly with Galactocentric radius. Thus, we fit the annular median abundances linearly in Galactocentric radius to find a metallicity gradient of $\partial[\mathrm{Fe/H}]/\partial R_{\mathrm{GC}} = -0.051 \pm 0.005$ dex kpc^{-1} and $\partial[\mathrm{X/Fe}]/\partial R_{\mathrm{GC}}$ gradients for

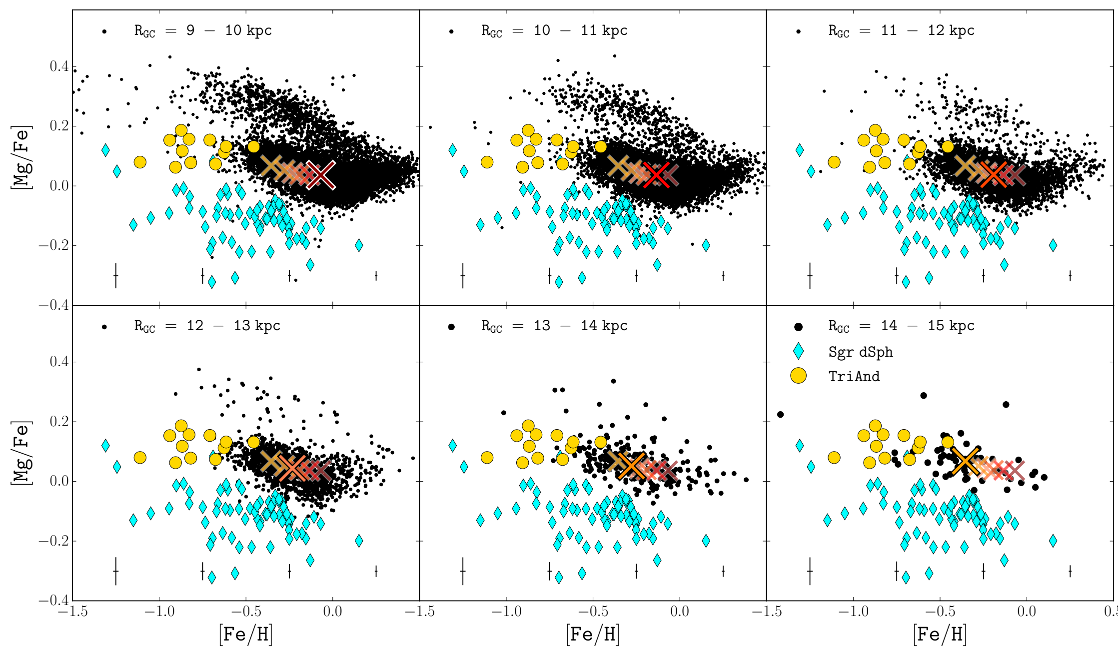

Fig. 3.3.— The [Mg/Fe]-[Fe/H] distributions in 1 kpc wide Galactocentric annular bins for the outer disk (black points, with increasing Galactocentric radius from the top left to the bottom right), TriAnd (gold circles) and Sgr dSph (cyan diamonds) samples. The median in each outer disk annulus has been marked with a cross, colored chromatically from dark red to orange for the innermost to the outermost annuli, with the medians in other annuli shown as smaller crosses of their respective colors. The plotted error bars show the median internal abundance uncertainties in 0.5 dex wide metallicity bins.

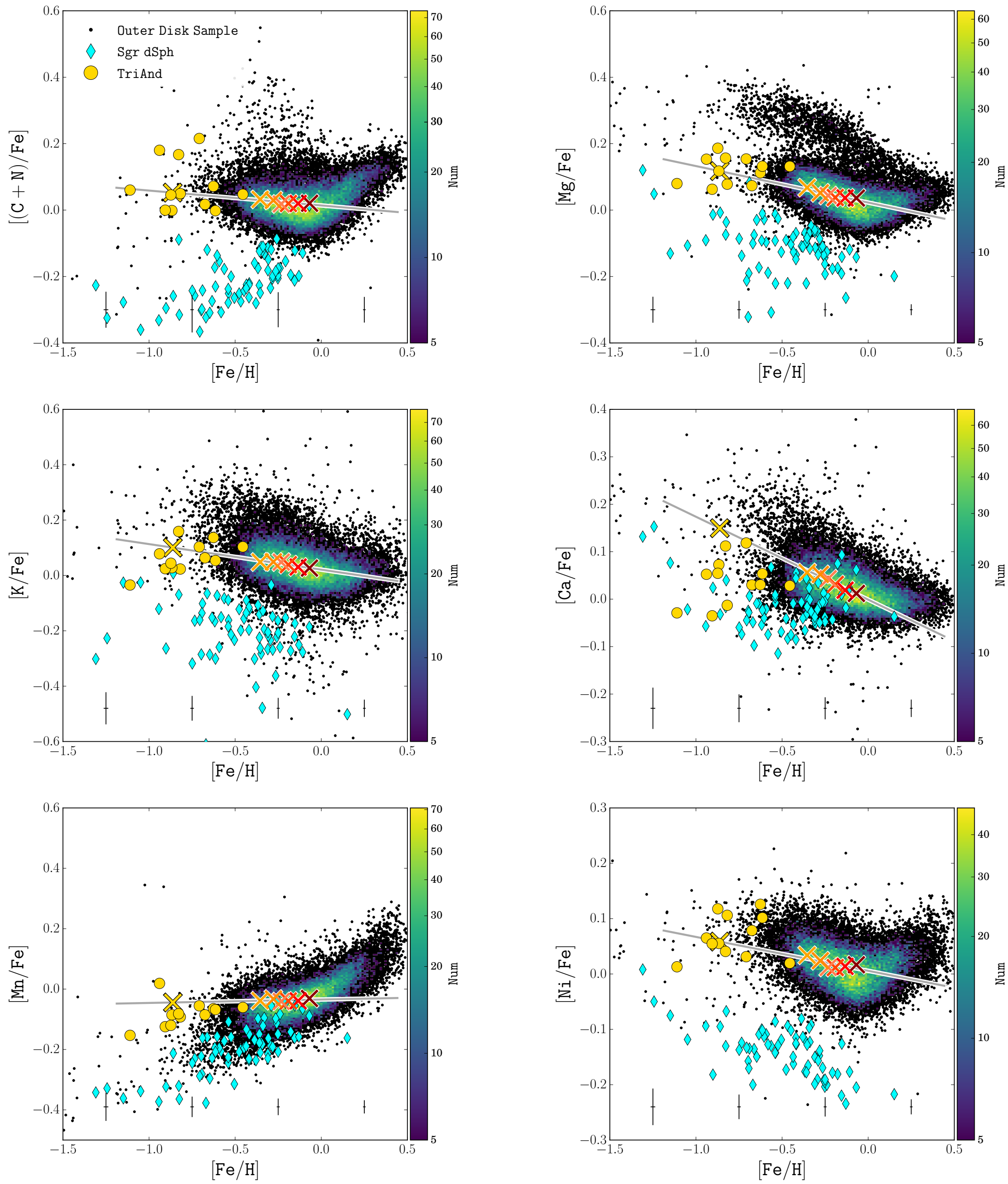

Fig. 3.4.— [X/Fe] (for (C+N), Mg, K, Ca, Mn, and Ni) versus [Fe/H] for the outer disk, TriAnd, and Sgr dSph samples (with colors and symbols as in Figure 3.2). The medians of the outer disk sample in 1 kpc wide Galactocentric annuli are plotted as crosses, colored according to Galactocentric radius, as in Figure 3.3. Linear parametric fits to [X/Fe]-[Fe/H] medians from $R_{\rm GC}$ of 9 kpc to 15 kpc as a function of $R_{\rm GC}$ are shown (gray lines) and extrapolated out to 30 kpc, with $R_{\rm GC} = 24$ kpc (the median Galactocentric radius of our TriAnd sample) marked as a gold cross. Typical uncertainties are shown as in Figure 3.3.

((C+N), Mg, K, Ca, Mn, Ni) = ($0.002 \pm 0.001,\ 0.006 \pm 0.001,\ 0.005 \pm 0.001,\ 0.009 \pm 0.001,\ -0.001 \pm 0.001,\ 0.003 \pm 0.002$) dex kpc^{-1}.

3.4 Discussion

Figure 3.4 demonstrates that, when extrapolated to the distance of TriAnd, the outer disk chemistry generally matches that of the TriAnd stars, which suggests that they are associated. For [Ca/Fe] the predicted median disk chemistry lies at the edge of the TriAnd distribution, which appears to indicate that a *linear* extrapolation of the disk Ca gradient may not be appropriate. We note that the flattening of the [Ca/Fe] trend in the outer disk at the largest radii seems astrophysically significant, and in comparison with the nearly constant gradient in the lower mass alpha-element, Mg, may be reflecting radial or time variations in the initial mass function or star formation history of the disk.

In contrast to the agreement with radial extrapolations of outer disk chemistry, the abundance patterns of the TriAnd stars are distinct from those of Sgr dSph stars, despite their similar metallicities. If the Sgr dSph is representative of the chemistry of relatively enriched tidal debris falling into the MW, then the chemical differences between TriAnd and Sgr dSph supports the notion that TriAnd is not tidal debris, at least from this type of dwarf galaxy. Another example of a relatively enriched dwarf galaxy is the Large Magellanic Cloud (LMC). While the α-element abundances of the LMC overlap some with the metal-poor stars in the thin disk (and thus with TriAnd), the LMC exhibits low Ni abundances, with [Ni/Fe] ~ -0.2 (Van der Swaelmen et al. 2013), about 0.3 dex lower than the [Ni/Fe] ratios found here in TriAnd stars. Thus, the LMC provides another example of a dwarf galaxy with distinct chemistry from TriAnd.

What about other potentially major accretion sources? Studies of metal-poor stars have uncovered two chemically distinct populations in the MW (e.g., Nissen & Schuster 2010; Hawkins et al. 2015; Hayes et al. 2018a). These two populations are (using the definitions from Hayes et al. 2018a; Fernández-Alvar et al. 2018) a "low-magnesium" halo population, thought to be accreted satellite galaxy debris, and a "high-magnesium" population, which continues the chemical trends of the thick disk and has the chemistry expected of the classical halo. The [X/Fe] ratios of TriAnd stars in (C+N), K, Mn, and Ni are 0.2-0.4 dex higher than the population of MW field stars thought to be accreted halo stars, and are also differentiated from the more classical halo population (and thick disk), which have high α-element abundances.

The results here are in agreement with those of Bergemann et al. (2018), who argue for an association of TriAnd with the MW disk based on O, Na, Mg, Ti, Ba, and Eu abundances of eight TriAnd stars[2] compared to MW, Fornax dSph, and Sgr dSph star samples. However, our conclusions are at odds with those reached by Chou et al. (2011), who proposed that TriAnd is more likely to be debris from a disrupted dwarf galaxy.

Chou et al. (2011) found a *mean* [Ti/Fe] ratio in their TriAnd sample of six stars (none of which overlap the Bergemann et al. sample or ours) about 0.2 dex lower than in Sgr dSph stars, and significantly lower than for their sample of MW stars from the solar neighborhood. These findings led to the original conclusion that TriAnd enriched slower than either population, consistent with expectations for a slowly enriching dwarf galaxy. However, this conclusion was largely drawn because half (three) of the stars in the Chou et al. TriAnd sample had [Ti/Fe] $\sim$ 0.5 dex lower than their MW comparison sample despite (a) the remainder of their sample having

[2]We have two stars in common with Bergemann et al., and the derived properties agree between the two studies within uncertainties and offsets of a typical size observed between APOGEE and optical studies (Jönsson et al. 2018).

[Ti/Fe] ratios consistent with the MW disk sample, and (b) Chou et al. finding their TriAnd sample to have s-process abundances in La and Y consistent with their MW disk trend. Unfortunately Ti abundances cannot be reliably measured by ASPCAP currently (Hawkins et al. 2016; Souto et al. 2016), and we cannot study TriAnd Ti abundances here.

Given the disk-like α-element abundances found for TriAnd stars by Bergemann et al. (2018, including disk-like Ti abundances), and those found for our TriAnd sample here, it seems that the lower [Ti/Fe] ratios found by Chou et al. (2011) may not be representative of the α-element abundances of TriAnd as a whole. Instead, the apparently considerably lower [Ti/Fe] in three Chou et al. (2011) stars relative to the disk may be due to a variety of causes, including random measurement errors, systematic offsets between their TriAnd [Ti/Fe] and their adopted disk chemistries from the literature, or small number statistics drawing from a TriAnd population with a potentially large intrinsic scatter in Ti abundances. Reconsidering that the Y, La and half of the Ti abundances in the Chou et al. sample are consistent with MW disk abundance patterns, their results could be reinterpreted as supporting a disk origin.

In summary, we find that TriAnd is chemically distinct from the Sgr dSph, having [X/Fe] $\sim 0.1 - 0.4$ dex higher in (C+N), Mg, K, Ca, Mn, and Ni, and is also distinct from the LMC in its Ni abundances, having [Ni/Fe] ~ 0.3 dex higher than the LMC stars observed by Van der Swaelmen et al. (2013). On the other hand, while our TriAnd stars are typically more metal-poor ([Fe/H] ~ -0.8) than most outer disk stars sampled by APOGEE, TriAnd does appear to overlap in chemical space with the lowest metallicity stars ([Fe/H] ~ -0.7) known to lie in the outer regions of the disk. Moreover, linear extrapolation of each of the chemical gradients measured in the

APOGEE outer disk sample to the Galactocentric radii of the TriAnd stars predicts abundances similar to those found in our TriAnd sample. These results support the proposition that TriAnd is associated with the outer disk of the MW and, if so, its large distance from the midplane ($\sim$ 7 kpc) may be the result of a perturbation to the MW disk (as in Laporte et al. 2018).

If the TriAnd overdensity is indeed a feature of the MW disk, then that would imply that the disk extends to radii $\gtrsim$ 24 kpc (i.e., the Galactocentric radius of our TriAnd sample), as suggested by Lopez-Corredoira et al. (2018). By inference, this greater MW disk would extend through the radii occupied by other Galactic anticenter overdensities (such as the Monoceros Ring) and lend greater weight to the notion that they, too, are parts of the MW disk.

Chapter 4

Constraining the Solar Galactic Reflex Velocity Using Gaia Observations of the Sagittarius Stream

Summary

Because of its particular orientation around the Galaxy — i.e., in a plane nearly perpendicular to the Galactic plane and containing both the Sun and Galactic center — the Sagittarius (Sgr) stream provides a powerful means by which to measure the solar reflex velocity, and thereby infer the velocity of the Local Standard of Rest (LSR), in a way that is independent of assumptions about the solar Galactocentric distance. Moreover, the solar reflex velocity with respect to the stream is projected almost entirely into the proper motion component of Sgr stream stars perpendicular to the Sgr plane, which makes the inferred velocity relatively immune to most Sgr

model assumptions. Using *Gaia* DR2 proper motions of ∼2,000 stars identified to be Sgr stream candidates in concert with the Law & Majewski (2010) Sgr N-body models (which provide a good match to the *Gaia* observations) we constrain the solar reflex velocity induced by its orbital motion around the Galaxy to be $\Theta_{\odot} = 253 \pm 6$ km s^{-1}. Assuming a solar peculiar motion in the direction of orbital rotation of 12 km s^{-1}, and an LSR velocity of 12 km s^{-1} with respect to the local circular speed, the implied circular speed of the Milky Way at the solar circle is 229 ± 6 km s^{-1}.

4.1 Introduction

It has been over thirty years since the International Astronomical Union addressed disparities in derived values of the solar Galactocentric distance, R_0, and the Galactic circular rotation velocity at the Sun, Θ_0, of ±1 kpc and ±20 km s^{-1} respectively by recommending the adoption of $R_0 = 8.5$ kpc and $\Theta_0 = 220$ km s^{-1} "in cases where standardization on a common set of galactic parameters is desirable."[1] Despite continued work to establish these parameters, it seems that the dispersions in determinations have not significantly diminished.

Recent estimates of Θ_0 span a wide range, $218 - 254$ km s^{-1}, including those from radio interferometric proper motion measures of star forming regions (Bovy et al. 2009; Reid et al. 2009) and Sgr A* (Reid & Brunthaler 2004), as well as explorations of stellar kinematics from the APOGEE (Bovy et al. 2012) and SEGUE surveys (Schönrich 2012), or the kinematics of Cepheids (Kawata et al. 2018); however the latest of these studies have tended toward the middle of that range.

One source of uncertainty is that there is a degeneracy between the inferred Θ_0 and inferred R_0, for most measurement methods. Assessments are further compli-

[1] The 1985 recommendation of IAU Commission 33, https://www.iau.org/static/resolutions/IAU1985_French.pdf.

cated by the fact that the Sun has a peculiar motion with respect to the Local Standard of Rest (LSR), while the LSR may itself be moving with respect to a simple circular orbit around the Galaxy. Thus Θ_0 is typically entangled with the Θ-directional components of the solar peculiar motion and LSR motion. The latter are often simplified to the Galactic Cartesian counterparts $V_{\odot,pec}$ and $V_{LSR,pec}$, respectively (since these velocities are often measured using an ensemble of nearby stars), so that, in cylindrical coordinates, the net revolutionary component of the Sun's motion is $\Theta_\odot = \Theta_0 + V_{LSR,pec} + V_{\odot,pec}$. Values of $V_{\odot,pec}$ hover around 12 km s^{-1}, and Bovy et al. (2012) claim that $V_{LSR,pec}$ may also be as high as 12 km s^{-1}.

In this chapter we focus on a new measurement of $\Theta_\odot$. Majewski et al. (2006) demonstrated that the Sgr stream provides an effective means to measure $\Theta_\odot$ (from which $\Theta_{\rm LSR} = \Theta_0 + V_{LSR,pec}$ and Θ_0 can be inferred), independent of the assumed R_0 or the precise shape of the Galactic mass distribution, and that avoids having to observe sources in the heavily crowded and dust-extinguished Galactic Center. The method exploits the favorable orientation of the Sgr stream, which is in a nearly polar orbit that intersects the Galactic plane virtually along the line between the Sun and the Galactic Center. In this orientation, the Sgr plane provides a non-rotating reference against which the solar motion may be measured, with almost all of the reflex motion imprinted on the proper motions of Sgr stars perpendicular to the stream. At the time of Majewski et al. (2006), the proper motions for known Sgr stream stars were not good enough to apply the method rigorously. However, exploiting proper motions of ∼1-2 mas yr^{-1} accuracy for ∼1-2 dozen spectroscopically-confirmed Sgr stream stars in four fields along the Sgr trailing arm, Carlin et al. (2012) found that their proper motions were best reproduced by models similar to the Law & Majewski (2010, "LM10" hereafter) Sgr destruction models but utilizing an LSR velocity of 264 ± 23

km s^{-1}.

The second data release from the ESA-*Gaia* mission (*Gaia* DR2; Gaia Collaboration et al. 2018a) now provides the opportunity make this measurement with a significantly larger sample of stars having proper motions an order of magnitude more precise.

4.2 Sagittarius Stream in *Gaia*

Red giants are ideal tracers of the Sgr stream, because they can be seen to large distances. Thus we initially selected stars from the 2MASS catalogue (Skrutskie et al. 2006) with J, H, and K_s magnitudes between 10 and 13.5, covering a range of colors and magnitudes where giant stars trace the Sgr stream (e.g., Majewski et al. 2003). Such stars were selected in a series of rectangular regions (selected to cover Sgr longitudes $|B_\odot| \lesssim 20°$) on the sky around the trailing arm of the Sgr stream, which collectively span right ascensions from $\alpha = 320°$ to $75°$ and declinations $-40° < \delta < +40°$, which corresponds to about $90°$ of the Sgr stream trailing arm. The selected stars were then cross-matched with the *Gaia* DR2 source catalog (Gaia Collaboration et al. 2018a) using the CDS X-match service[2] adopting a $1''$ positional tolerance.

While *Gaia* DR2 does not measure parallaxes to a precision sufficient to reach the distances of the Sgr stream, we can still identify and remove nearby Milky Way (MW) contamination using *Gaia* DR2 parallaxes. Stars with relative parallax uncertainties $\sigma_\pi/\pi \leq 0.2$ can provide relatively reliable distance measurements, and almost all such stars in our sample have $1/\pi < 10$ kpc, considerably closer than the trailing arm of the Sgr stream (which ranges from about 20−40 kpc at different stream longitudes;

[2]`http://cdsxmatch.u-strasbg.fr/xmatch`

Majewski et al. 2003; Koposov et al. 2012). We therefore remove all of these stars from our sample, and, although it seems counter-intuitive, we keep the stars with poor parallaxes, $\sigma_\pi/\pi > 0.2$, which are primarily distant stars that we refer to as our "distant *Gaia* sample". To reduce the MW contamination in this distant *Gaia* sample further, we also removed stars at $\alpha > 50°$ and within 25° of the Galactic plane because these sky regions lie near the MW disk where contamination washes out the signature of the Sgr trailing arm.

The signature of the Sgr trailing arm is apparent as an arcing overdensity in the *Gaia* DR2 proper motion vector point diagram (PMVPD) for our distant *Gaia* sample (Fig. 4.1, lower left panel), so we trimmed in the PMVPD around the overdensity using -4 mas yr^{-1} $< \mu_\alpha \cos\delta <$ 2 mas yr^{-1} and -6 mas yr^{-1} $< \mu_\delta <$ 1 mas yr^{-1}. When restricting to these low proper motions, the stars in the Sgr trailing arm stand out with proper motion position angles (ϕ_μ) that are coherent and nearly linear with right ascension (Fig. 4.1, top left panel). The small scatter around this linear trend in ϕ_μ arises because the Sgr stream is kinematically cold, and provides an opportunity to greatly refine our selection of Sgr trailing arm candidates. However, elevated MW contamination at some α makes a simple linear fit to the data challenging, even with σ-clipping to reduce the noise. To avoid this problem, we apply the DBSCAN clustering algorithm (a density-based clustering algorithm that builds clusters of a given density; Ester et al. 1996) to the proper motion cut stars between $-20° < \alpha < 20°$, where the Sgr trailing arm feature is most free of MW contamination. This allows us to select the Sgr trailing arm feature in a reproducible manner, and use it to extract the feature at right ascensions where the contamination is more considerable.

Setting DBSCAN input parameters $\epsilon = 5$ and $N = 100$, with no normalization of ϕ_μ or α, the DBSCAN algorithm appears clearly to identify a cluster associated

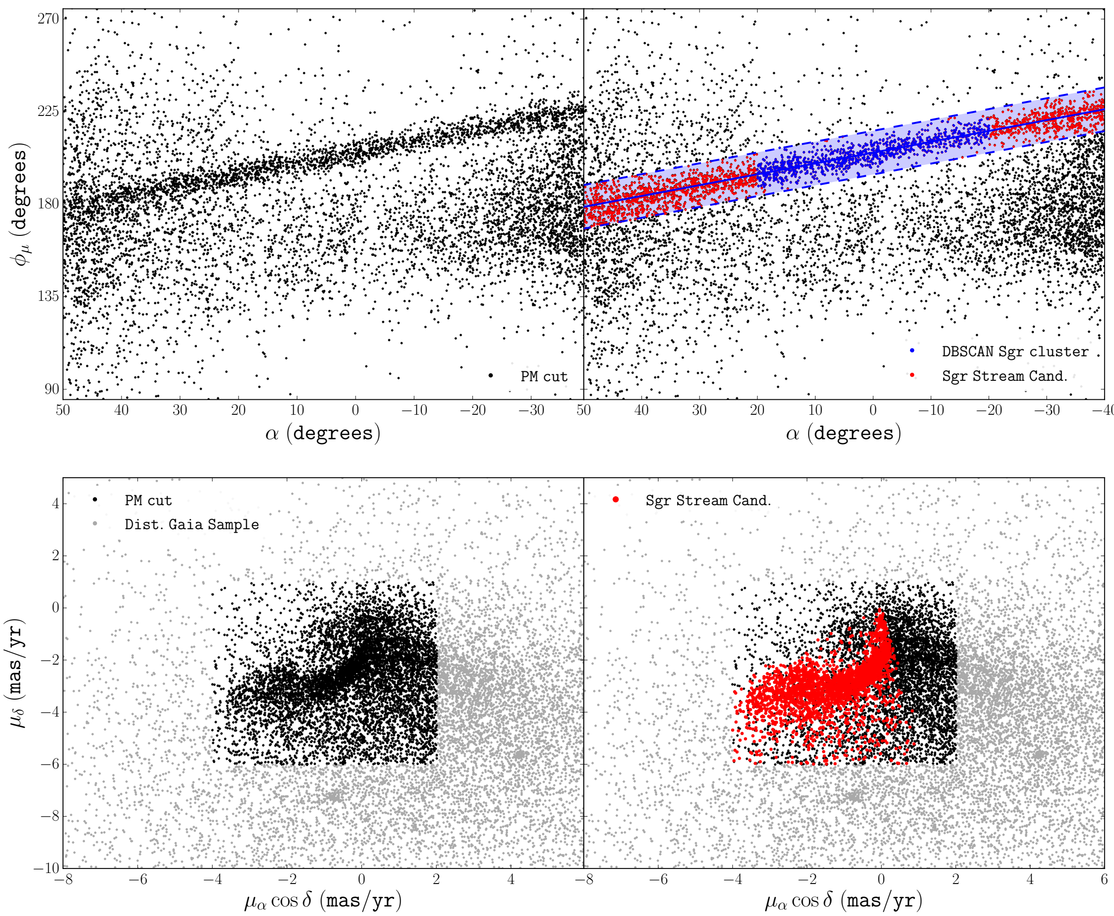

Fig. 4.1.— (Bottom) Proper motion vector point diagrams showing (bottom left) the distribution of proper motions in our distant *Gaia* sample (grey points), the restricted proper motion selection we use (black points), and the final Sgr trailing arm candidates (red points, bottom right). (Top) Proper motion position angle (ϕ_μ) as a function of right ascension (α), demonstrating (top left) the distinct, narrow, linear distribution of Sgr trailing arm stars, and (top right) the criteria for selecting our final sample of Sgr trailing arm candidates. The overplotted solid blue line (top right) is the linear fit to the DBSCAN selected "Sgr cluster" (blue points), and the shaded blue region bounded by dashed blue lines is the 3σ dispersion around this fit. The Sgr trailing arm candidates include the stars within the latter region (blue points) and those within 3σ of the extrapolation of this fit to the plot boundaries (red points).

with the Sgr trailing arm feature (blue points in the top right panel of Fig. 4.1). We fit a line to this DBSCAN-identified cluster and calculated the dispersion (σ) in the residuals to this fit. We extend this Sgr stream candidate selection outside the $-20° < \alpha < 20°$ range by extrapolating the fitted line and select stars within 3σ using this calculated dispersion. To measure of the remnant contamination, in the same parameter space we count the number of stars in a region of the same shape/size just above and below our Sgr stream selection, which we average and compare to the number of selected stream candidates to estimate a contamination of about 16%. This selection therefore includes the DBSCAN selected stars (blue) and the extended sample (red) shown in the right panels of Figure 4.1.

Finally, we trim the selected stars to Sgr orbital longitudes $\Lambda_{\odot} = 30 - 115°$ (so that the selection box cuts at right angles across the stream) and reject stars with proper motion errors in $\mu_{\alpha} \cos\delta$ or μ_{δ} greater than 0.2 mas yr^{-1}. This results in a final sample of 1,963 candidate Sgr Stream stars, with an estimated contamination of 16%.

The bottom right panel of Figure 4.1 shows that the arcing overdensity seen by eye in the PMVPD is due to the Sgr trailing arm as traced by these candidates. However, as seen in the top panels of Figure 4.1, there is still a higher level of contamination at either end of the α-range of our sample, particularly at $\alpha \gtrsim 30°$. Moreover, in the μ_{δ} distribution of our Sgr trailing arm candidates there appears to be a tail toward values below ~ -4 mas yr^{-1}. This low density, low μ_{δ} tail is not found in the Sgr stream models discussed below and is likely remnant MW contamination.

4.3 Sagittarius Stream N-body Models

If the Sgr stream were on a perfectly polar orbit in the Galactic $X-Z$ plane[3] with no orbital precession along the stream, any systematic motion of the stream out of its orbital plane would be entirely due to the Sun's own reflex motion, which could then be measured directly from the data. In reality, Sgr is not on a purely polar orbit, the orbital plane is not precisely aligned with the Galactic $X-Z$ axis, and the observed tidal streams precess slightly with increasing distance from the Sgr core. Therefore, we must compare the observations against N-body models that properly incorporate these various effects.

We do so using the LM10 model, which is well fit to the observed run of Sgr stream angular positions, radial velocities, and distances throughout the $\Lambda_{\odot} = 30 - 115°$ range of the trailing arm. Despite the inability of this model to reproduce some key features of the broader Sgr−Milky Way system (particularly, the bifurcation of the stream and the large apocentric distance for the trailing arm at $\Lambda_{\odot} \sim 180°$) it nonetheless remains the best-constrained model at the orbital longitudes considered here. Indeed, this particular section of the stream is easy to fit *regardless* of the assumptions made about the depth and detailed shape of the Galactic gravitational potential (in contrast to the leading arm for which a triaxial halo is necessary to fit both the angular positions and radial velocities simultaneously; Law et al. 2009). As discussed by LM10 (see also discussion by Law et al. 2005), the dynamically young trailing arm has little power to constrain the shape of the Galactic dark matter halo and can be equally well fit in an oblate, spherical, prolate, or triaxial potential, and regardless of the exact distance to the Sgr core, the distance to the Galactic center,

[3]We adopt the left-handed Galactocentric Cartesian coordinate system: X is positive towards the Galactic Anticenter, Y is positive towards the Galactic disk rotation at the location of the Sun, and Z is positive towards the North Galactic Pole.

or the overall normalization of the depth of the Galactic gravitational potential via the local circular speed Θ_0.

The insensitivity to various factors is exactly what makes the trailing arm ideal for this study: for these stars a single and interesting model parameter, Θ_0, is strongly coupled to a single observational parameter, one dimension of their proper motion. In previous studies, for widely varying values of Θ_0, the tangential velocity of the Sgr core along its orbit — hitherto largely unconstrained given the uncertainties of past proper motion studies — could be dialed to optimize the match of the implied radial velocities along the trailing stream to available observations. Now, with the new proper motion constraints available from Gaia, we can discriminate between models having different values of Θ_0 and constrain the solar reflex velocity.

Carlin et al. (2012) reproduced the LM10 analysis (which assumed $\Theta_0 = 220$ km s^{-1}), but for a range of different values of $\Theta_0 = 190 - 310$ km s^{-1} (sampled every 30 km s^{-1}, along with two 'best-fit' cases where $\Theta_0 = 232$ km s^{-1} and 264 km s^{-1}). Because the dark matter halo contributes minimally within the solar circle, these models were realized by scaling the Galactic bulge/disk mass jointly to produce the desired local circular speed. The details of these models are discussed in LM10 and Carlin et al. (2012), and in brief, assume a three-component Galactic mass distribution consisting of a Hernquist spheroid, Miyamoto-Nagai disk, and a triaxial logarithmic dark matter halo with minor/major axis ratio $(c/a)_\Phi = 0.72$, intermediate/major axis ratio $(b/a)_\Phi = 0.99$, and the minor axis pointing towards $(l, b) = (7^\circ, 0^\circ)$. The Sgr dwarf within this Galactic gravitational potential is constrained to lie at $(l, b) = (5.6^\circ, -14.2^\circ)$, a distance of 28 kpc, and a heliocentric radial velocity $v_{\rm hel} = 142.1$ km s^{-1}, with leading and trailing arms that match observed trends of angular position and radial velocity along orbital longitude of the stream. Each model assumed that the solar peculiar motion with respect to the local circular speed was given by $(U, V, W) = (-9, 12, 7)$ km s^{-1} in a left-handed coordinate frame (Cox 2000), for a range in solar reflex velocities of $\Theta_\odot = 202 - 322$ km s^{-1}.

4.4 Discussion

As illustrated in Figure 4.2, the LM10 model (middle column) continues to be a good match to observations of the Sgr stream in the $\Lambda_\odot = 30 - 115°$ range of the trailing tail, despite the fact that no proper motions were used to constrain the model. This is perhaps unsurprising given that LM10 tuned the other four dimensions of phase space to reproduce all observational data available at the time. We note, however, that the run of proper motions in the declination direction is not quite a perfect match to the *Gaia* observations; furthermore, versions of the LM10 model in potentials with slower or faster circular speeds (left and right columns respectively) result in linear shifts of the model in μ_δ while remaining almost unchanged in $\mu_\alpha \cos\delta$ and heliocentric radial velocity.

This situation arises because of another fortuitous orientation of the Sgr stream with respect to *celestial* coordinates. In N-body models where the Milky Way circular speed is larger, the proper motion of model stars in the direction perpendicular to the Sgr plane is larger due to the greater solar reflex motion. Since the model Sgr dwarf must be made to move faster along its orbit to compensate for the deeper gravitational potential, these model stars also have faster motion within the Sgr plane. In the trailing stream, the vector addition of these components is such that the net change in proper motion for stream stars between different models happens to be almost entirely along μ_δ.

As we show in Figure 4.3 (left-hand panel), the difference between the (2σ-clipped)

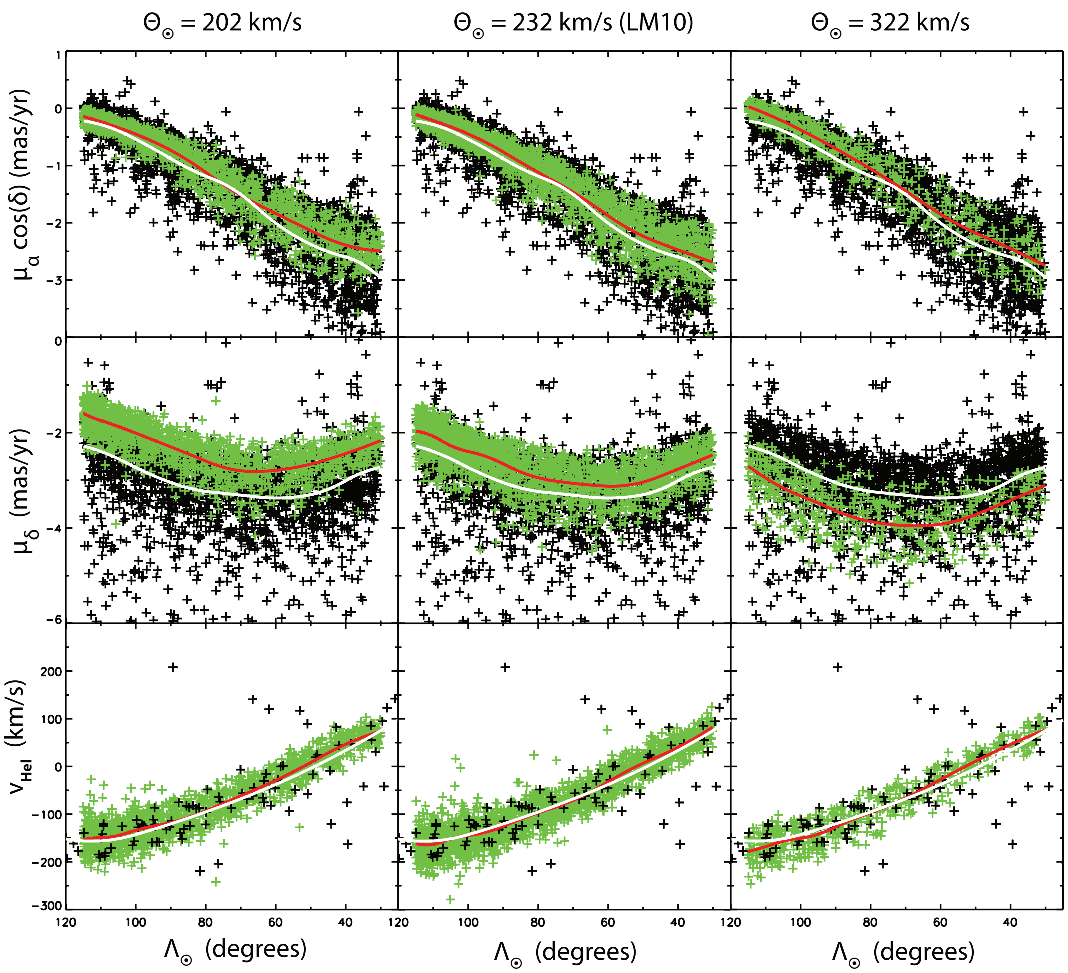

Fig. 4.2.— Sgr stream models with different solar reflex velocities compared to observational data as a function of stream longitude $\Lambda_{\odot}$. The middle column shows the LM10 model, while the left-/right-hand columns show models with slower/faster reflex velocities respectively. Top row: proper motion along α. Middle row: proper motion along δ. Bottom row: heliocentric radial velocity. In the top two rows black points represent the *Gaia* observations, while in the bottom row black points represent M-giant observations from Majewski et al. (2004). Green points represent N-body simulated tidal debris. Solid white/red lines in all panels represent 2σ-clipped spline model fits to the observed/simulated data respectively to guide the eye.

mean proper motion of the N-body models versus the observed stream is nearly constant with $\Lambda_\odot$, such that the model with reflex velocity $\Theta_\odot = 202$ km s^{-1} is systematically offset by about +0.5 mas yr^{-1} (purple curve), wheras the model with $\Theta_\odot = 322$ km s^{-1} is offset by about -0.6 mas yr^{-1} (red curve). The consistency of these systematic differences suggests that we can average these offsets over orbital longitude to obtain a single value $\langle \Delta\mu_\delta \rangle$ describing the N-body model stream offset from the *Gaia* proper motions for different $\Theta_\odot$ (Fig. 4.3, right-hand panel). This relation is well described by a simple linear fit to within observational uncertainty. By taking this fit (and the 1σ uncertainties thereon) we solve for the $\langle \Delta\mu_\delta \rangle = 0$ km s^{-1} crossing point and determine that this occurs at $\Theta_\odot = 253 \pm 5$ km s^{-1}. Limiting our analysis to the DBSCAN selection α-range where contamination is minimal, $\Lambda_\odot \sim 52 - 80$, we find $\Theta_\odot = 247 \pm 9$ km s^{-1}, a slightly lower value, but one that is more uncertain because the sample is three times smaller. Because this result has a larger uncertainty and results in less than a 1σ difference, we proceed with $\Theta_\odot$ derived from the full sample.

An estimate of the possible systematic uncertainty in this measurement can be obtained by comparing the proper motion of the Sgr core in these N-body models with the *Gaia* observations. Because the models adopted an orbital pole defined by the path of the tidal streams (Majewski et al. 2003), varying $\Theta_\odot$ in these models describes a linear relation in the PMVPD for the Sgr core (see Figure 2.8 of Law & Majewski 2016) according to the speed of Sgr along its orbit perpendicular to the line of sight (dialed up and down to compensate for the altered Galactic potential following from changes in Θ_0). The observed *Gaia* proper motion of the Sgr core $((\mu_\alpha \cos\delta, \mu_\delta) = (-2.692, -1.359)$ mas/yr; Gaia Collaboration et al. 2018b) lies slightly off this relation by about 0.15 mas yr^{-1}, but is most consistent with a choice of $\Theta_\odot = 256$ km s^{-1}. We therefore adopt 3 km s^{-1} (the difference between this value and the value derived from fitting the trailing stream) as our systematic uncertainty; by combining systematic and random uncertainty terms our final estimate of the solar reflex velocity is $\Theta_\odot = 253 \pm 6$ km s^{-1}.

This measurement is consistent with both the values of $\Theta_\odot = 242^{+10}_{-3}$ km s^{-1} obtained by Bovy et al. (2012)[4] and $\Theta_\odot = 256 \pm 17$ km s^{-1} obtained by Carlin et al. (2012, using all observable constraints applied to their highest-purity fields) to within 1σ. Meanwhile, combining the proper motion of Sgr A* in the Galactic Plane, $\mu_l = 6.379 \pm 0.026$ mas yr^{-1} (Reid & Brunthaler 2004), with the recent, high precision measure of $R_0 = 8.122 \pm 0.031$ kpc from Gravity Collaboration et al. (2018) yields a value of $\Theta_\odot = 245.6 \pm 1.4$ km s^{-1}. Combining the uncertainties on this R_0 dependent measure of $\Theta_\odot$ and the $\Theta_\odot$ reported here, there is a 1.2σ difference between the two results, which is still a reasonable agreement. While the reflex motion measured with respect to Sgr A* nominally provides higher precision, our estimate is an important, *independent* probe using a method that does not depend on the Galactocentric radius of the Sun. If we assume that $V_{\odot,pec} = 12$ km s^{-1} and likewise follow Bovy et al. (2012) in assuming that $V_{LSR,pec} = 12$ km s^{-1}, then our results imply a local Milky Way circular velocity of $\Theta_0 = 229 \pm 6$ km s^{-1}.

We note that the overall 6 km s^{-1} uncertainty in our estimate of the solar reflex velocity is driven primarily by the large intrinsic width of the stream. In both the observations and N-body models the 1σ width of the μ_δ distribution is about 0.5 mas yr^{-1}; with ten longitude bins each containing about 200 stars, this translates to an uncertainty of about 11 μas/yr in the mean. Similar efforts using dynamically colder streams may be able to obtain more precise results, and such generalizations of our method to arbitrary streams appear promising (Malhan & Ibata 2017).

[4] $V_{\phi,\odot}$ in their notation.

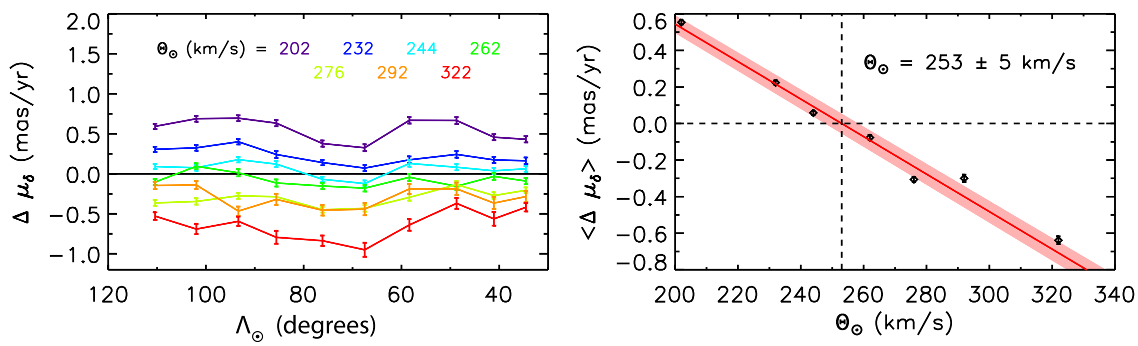

Fig. 4.3.— (Left) Difference in μ_δ proper motion between the observations and the seven N-body models (colored lines) in ten bins (each containing the same number of stars) along orbital longitude $\Lambda_\odot$. Error bars represent the 1σ uncertainty in the mean for each bin. (Right) Mean difference in μ_δ averaged over all longitude bins as a function of solar reflex velocity $\Theta_\odot$ (black points with 1σ error bars). The solid red line and shaded red region represent the best first order polynomial fit and associated 1σ uncertainty. The zero-crossing point is located at $\Theta_\odot = 253 \pm 5$ km s^{-1}.

Chapter 5

Metallicity and α-element Abundance Gradients along the Sagittarius Stream as Seen by APOGEE

Summary

Using 3D positions and kinematics of stars relative to the Sagittarius (Sgr) orbital plane and angular momentum, we identify 166 Sgr stream members observed by the Apache Point Observatory Galactic Evolution Experiment (APOGEE) that also have *Gaia* DR2 astrometry. This sample of 63/103 stars in the Sgr trailing/leading arm are combined with an APOGEE sample of 710 members of the Sgr dwarf spheroidal core (385 of them newly presented here) to establish differences of 0.6 dex in median metallicity and 0.1 dex in [α/Fe] between our Sgr core and dynamically older stream samples. Mild chemical gradients are found internally along each arm, but these steepen when anchored by core stars. With a model of Sgr tidal disruption providing estimated dynamical ages (i.e., stripping times) for each stream star, we find a mean metallicity gradient of 0.12 ± 0.03 dex/Gyr for stars stripped from Sgr over time. For the first time, an [α/Fe] gradient is also measured within the stream, at 0.02 ± 0.01 dex/Gyr using magnesium abundances and 0.04 ± 0.01 dex/Gyr using silicon, which imply that the Sgr progenitor had significant radial abundance gradients. We discuss the magnitude of those inferred gradients and their implication for the nature of the Sgr progenitor within the context of the current family of Milky Way satellite galaxies, and suggest that more sophisticated Sgr models are needed to properly interpret the growing chemodynamical detail we have on the Sgr system.

5.1 Introduction

The Sagittarius (Sgr) dwarf spheroidal (dSph) galaxy and its tidal stream provide a nearby and vivid example of a tidally disrupting dwarf galaxy (Ibata et al. 1994; Majewski et al. 2003) and the hierarchical growth of large galaxies through minor mergers. Because Sgr is in a quite advanced stage of tidal stripping, yet its stars are not yet fully mixed with those of the Milky Way (MW), the system has become a remarkably versatile tool for exploring a great variety of astrophysical problems.

Numerous studies have exploited the extensive tidal debris structure as a sensitive probe of the MW, its dark matter content, and its dynamics. For example, because Sgr's tidal arms wrap through a large extent of the MW halo and trace the past and future orbit of the core, they can constrain the 3D shape of the MW's dark matter halo (Helmi 2004; Johnston et al. 2005; Law et al. 2005; Law & Majewski 2010; Deg, & Widrow 2013; Ibata et al. 2013; Vera-Ciro, & Helmi 2013). Moreover, the alignment of Sgr's orbit is nearly perpendicular to the MW disk and crosses the disk midplane relatively near the Sun-Galactic Center axis; this fortuitous configuration means that the solar rotational velocity can also be gauged directly via the reflex solar motion imprinted in the velocities/proper motions of stars in the stream (Majewski et al. 2006; Law & Majewski 2010; Carlin et al. 2012; Hayes et al. 2018c). Sgr has also been identified as a possible culprit for dynamical perturbations observed in the MW disk, and as such provides a case study on the potential effects of minor mergers on the evolution of the stellar and HI disks (Ibata & Razoumov 1998; Gómez et al. 2013; Laporte et al. 2018, 2019).

Obviously, the Sgr system also lends uniquely accessible and detailed insights into the tidal disruption and dynamical evolution of dwarf galaxy satellites. This includes not only clues into potential morphological and dynamical changes in dwarf galaxies induced by the encounters with larger galaxies like the MW (Łokas et al. 2010; Peñarrubia et al. 2010, 2011; Frinchaboy et al. 2012; Łokas et al. 2012; Majewski et al. 2013), but also effects on their star formation histories and the chemical evolution of their stellar populations. The latter have clearly been shaped by the interplay between episodic star formation incited by gravitational shocking at orbital pericenter and the stripping of gas (Siegel et al. 2007; Tepper-García, & Bland-Hawthorn 2018).

A particularly important lesson learned from studies of the Sgr system is that any assessment of the chemical and star formation histories and distribution functions of Sgr or another tidally disrupted system will be incomplete and biased without properly accounting for the stellar populations lost via tidal stripping (Chou et al. 2010; Carlin et al. 2018, ; see also earlier discussions of this phenomenon in Majewski et al. 2002; Muñoz et al. 2006). This is because tidal stripping preferentially acts on the least bound stars in a dwarf, and those stars tend to be older and less chemically evolved stars in the system.

The discovery of large mean metallicity differences at the level of Δ[Fe/H] $\sim$ 0.4-0.6 dex between samples of stars in the Sgr core and the (lower metallicity) Sgr stream (Chou et al. 2007; Monaco et al. 2007) provided early suggestions of the possible metallicity gradients along the Sgr stream. If such chemical gradients do indeed exist along the Sgr stream, they may be the preserved remnants of chemical gradients that existed within the Sgr progenitor galaxy.

N-body modeling of Sgr's tidal stripping was implemented by Law & Majewski (2010, hereafter LM10), who used a prescription for assigning metallicities to model particles based on their initial energy in the bound progenitor, which naturally yielded a radial gradient in mean metallicity in the simulated dwarf. Based on this modeling, LM10 found that the observed metallicity differences between stream and core implied a mean radial metallicity variation as large as 2.0 dex before Sgr's tidal disruption, exceeding that seen in any other dwarf galaxy.

Since these first identifications of significant metallicity differences between the Sgr stream and core, further studies have measured the metallicity of Sgr stream stars and reported metallicity gradients (Keller et al. 2010; Carlin et al. 2012; Shi et al. 2012; Hyde et al. 2015) along the Sgr stream. However, the sampling and measurement of gradients was not consistent across studies, which complicates their comparison. Specifically, some authors report metallicity gradients from the Sgr core through each tidal arm (such that the high end of the gradient is anchored by the metallicity of the core) and find metallicity gradients of about 2.4-2.7 $\times 10^{-3}$ dex deg^{-1} along the trailing arm (Keller et al. 2010; Hyde et al. 2015). Other studies measure only the internal metallicity gradients within each arm (excluding the metallicity of the Sgr dSph core), which produces much flatter gradients, around 1.4-1.8 $\times$ 10^{-3} dex deg^{-1} along the trailing arm and about 1.5 $\times$ 10^{-3} dex deg^{-1} along the leading arm (Carlin et al. 2012; Shi et al. 2012).

Because a large fraction (75% at high latitudes) of the MW halo M giants belong to the Sgr stream (Majewski et al. 2003), some studies have employed a color selection to exclusively study the relatively metal-rich M giants in the stream, since they are subject to less contamination than samples of the more common K giants (Chou et al. 2007; Monaco et al. 2007; Keller et al. 2010; Carlin et al. 2018). However, M giants are only produced by higher metallicity populations, so these samples would have an implicit metallicity bias, and could skew some of these past measurements of metallicity gradients.

Because of the observational demands required by high-resolution spectroscopy, few detailed chemical abundance studies of stream stars have been performed, and only measured abundances for relatively small samples (Monaco et al. 2007; Chou et al. 2010; Keller et al. 2010; Carlin et al. 2018). However, such studies have attempted to explore the α-element abundances of Sgr stream stars, and typically report similar α-element abundance levels to stars in the Sgr core Monaco et al. (2007); Chou et al. (2010); Carlin et al. (2018), or equivalently suggest no significant α-element gradients along the stream (Keller et al. 2010).

The Apache Point Observatory Galactic Evolution Experiment (APOGEE; Majewski et al. 2017) provides a unique opportunity to study the detailed chemistry of the Sgr stream. APOGEE is a high-resolution ($R \sim 22,500$), H-band (1.5-1.7 μm) spectroscopic survey that primarily targets red giant stars and samples a relatively large area of the sky. While the APOGEE survey imposes a blue color limit to prioritize observations of red giants and minimize contamination from warmer main sequence dwarfs, this limit, $(J-K)_0 \geq 0.3$ in halo fields ($|b| \gtrsim 16^\circ$, where most of the Sgr stream lies) and $(J-K)_0 \geq 0.5$ otherwise, is still liberal enough to provide relatively unbiased metallicity coverage for red giant branch stars (RGB; Zasowski et al. 2013, 2017). In addition, the dual-hemisphere coverage of APOGEE-2 allows us to sample nearly continuously along large sections of both arms of the Sgr stream.

Observations of Sgr dSph core members were first reported in APOGEE by Majewski et al. (2013) using the Sloan Digital Sky Survey (SDSS) Data Release 12 (DR12 Alam et al. 2015), and the membership was expanded by Hasselquist et al. (2017) using SDSS DR13 (Albareti et al. 2017; Holtzman et al. 2018), both taking advantage of the intentional APOGEE targeting of the Sgr core. While a few APOGEE fields were placed intentionally along the Sgr stream, Hasselquist et al. (2019) demonstrated that both the trailing and leading arm of the Sgr stream are relatively well-sampled *serendipitously* by the random targeting employed by the APOGEE survey.

Hasselquist et al. (2019) used chemical tagging to identify 35 relatively metal-rich, [Fe/H] $\gtrsim -1.2$, Sgr stream stars in the APOGEE data presented in SDSS DR14 (Abolfathi et al. 2018; Holtzman et al. 2018), which only included APOGEE data in the Northern Hemisphere. However, the chemical tagging method that was used to identify these Sgr stars is limited to these higher metallicities, because it relies on the fact that the chemical abundance profile of Sgr is distinct from the MW at these metallicities (Hasselquist et al. 2017, 2019).

At lower metallicities, the chemical abundance profile of Sgr begins to merge with that of the accreted MW halo (Hayes et al. 2018a; Hasselquist et al. 2019), so to push to lower metallicities we must use other means to identify Sgr members. Fortunately, the Sgr system, including the Sgr stream, possesses a relatively unique orbit that enables Sgr stream members to be readily identified *kinematically* from surveys of the MW. The Sgr stream is also sufficiently close that *Gaia* DR2 proper motions (Gaia Collaboration et al. 2018a), APOGEE radial velocities, and spectrophotometric distances can be measured to such a precision that complete 6-D phase space information can be obtained for large samples of candidate stars. Because a selection of the Sgr stream candidates from the 6-D phase space distribution of APOGEE-observed stars is relatively free from metallicity bias, one can reliably measure chemical gradients along the Sgr stream from the identified stream members.

In this work we perform such a selection of Sgr stream stars based on their 3D positions and velocities relative to the Sgr orbital plane. We also exploit the fact that APOGEE-2 is now operating in both the Northern and Southern Hemispheres, so that, with the dual hemisphere APOGEE data reported in SDSS DR16 (Ahumada et al. 2020; Jönsson et al. in prep.), we can obtain a more complete coverage of both the leading and trailing arms of the the Sgr stream. With a relatively large sample of Sgr stream members, and the precise multi-element APOGEE abundances, we can also begin probing gradients in chemical abundance ratios along the Sgr stream as well as metallicity gradients.

Section 2 provides an overview of the data and quality restrictions we employ for our study. Section 3 describes the selection criteria applied for identifying Sgr stream stars based on their 3D positions and kinematics within a Galactocentric coordinate system defined by the Sgr orbital plane. Using the high precision bulk metallicities and chemical abundances that APOGEE measures, in Section 4 we discuss the chemical differences found between the Sgr stream and core in Section 4.1, our assessment of metallicity gradients along the Sgr stream in Section 4.2, the first measurements of non-zero α-element abundance gradients along the stream in Section 4.3, and, through the use of an N-body simulation, we collate the data from the two arms to understand the chemical gradients as a function of dynamical age or stripping time in the Sgr stream in Section 4.4. Section 5 discusses the implications that the measured chemical differences and gradients along the stream have for the chemical structure of the progenitor Sgr galaxy. Finally, in Section 6 we present our main conclusions.

5.2 Data

The data in this chapter come primarily from the APOGEE survey (Majewski et al. 2017) and its successor APOGEE-2. We use the APOGEE data in SDSS-IV DR16 (Blanton et al. 2017; Ahumada et al. 2020; Jönsson et al. in prep.) that will be made publicly available in December 2019. This data release includes data taken from both the Northern and Southern Hemispheres using the APOGEE spectrographs (Wilson et al. 2019) on the SDSS 2.5-m (Gunn et al. 2006) and the 2.5-m du Pont (Bowen & Vaughan 1973) telescopes respectively. The targeting procedure for APOGEE is presented in Zasowski et al. (2013, 2017) and Beaton et al. (in prep.), and details of the data reduction pipeline for APOGEE can be found in Nidever et al. (2015). Stellar parameters and chemical abundances are derived from the APOGEE Stellar Parameter and Chemical Abundance Pipeline (ASPCAP; García Pérez et al. 2016), based on the FERRE[1] code, through a similar procedure as in SDSS DR14/15. For SDSS DR16, ASPCAP has now been updated to use a grid of only MARCS stellar atmospheres (Gustafsson et al. 2008), rather than Kurucz (Kurucz 1979; Jönsson et al. in prep.), and using a new H-band line list from Smith et al. (in prep.) that updates the earlier APOGEE line list presented in Shetrone et al. (2015), all of which are used to generate a grid of synthetic spectra (Zamora et al. 2015).

From the full APOGEE sample, we remove stars flagged[2] as having the STARFLAGS: BAD_PIXELS, VERY_BRIGHT_NEIGHBOR, or LOW_SNR set, or any stars with poorly

[1] `https://github.com/callendeprieto/ferre`

[2] A description of these flags can be found in the online SDSS DR15 bitmask documentation (`http://www.sdss.org/dr15/algorithms/bitmasks/`)

determined stellar parameters, as may be indicated by the ASPCAPFLAGS: ROTATION_WARN or STAR_BAD. Since we do not expect to detect dwarf stars in APOGEE at the distance of the Sgr stream, we limit our analysis to giant stars by selecting stars with calibrated $\log g < 4$. In addition we only analyze stars with low velocity uncertainty, $V_{\rm err} \leq 0.2$ km s^{-1}, and, when considering chemical abundances in Sections 4 and further sections, we require stars to have S/N > 70 per pixel spectra to remove stars with lower quality spectra and consequently less reliable ASPCAP-derived stellar parameters and chemical abundances. We also restrict our chemical analysis in Section 4 and beyond to stars with effective temperatures warmer than 3700 K, where APOGEE stellar parameters and chemical abundances are reliably and consistently determined (for more details on the APOGEE DR16 data quality see Jönsson et al. in prep.).

Since we are interested in kinematically identifying distant Sgr Stream stars, we also remove stars that are associated with known globular clusters based on spatial and radial velocity cuts (except the globular cluster M54 that lies in the Sgr dSph), which helps reduce contamination from globular clusters on similar orbits to Sgr. While some globular clusters may be associated with Sgr, and therefore participated in its overall evolution (Da Costa & Armandroff 1995; Ibata et al. 1995; Dinescu et al. 2000; Bellazzini et al. 2003; Law, & Majewski 2010b), we want to understand the chemical evolution of the main Sgr progenitor, and in any case, globular clusters are contaminated with peculiar chemical pollution differentiating the first generation stars from the second generations that appear to exhibit chemistry unique from the rest of the Galaxy. We additionally remove the APOGEE fields centered on or near the Large and Small Magellanic Clouds (MCs), which are (unsurprisingly) dominated by the heavy sampling of MC stars and are unlikely to contain Sgr stream stars anyway, because these fields do not lie along the Sgr stream.

We supplement the APOGEE data with proper motions from *Gaia* DR2 (Gaia Collaboration et al. 2018a) and with spectrophotometric distances calculated with the Bayesian distance calculator `StarHorse` (Santiago et al. 2016; Queiroz et al. 2018) using multiple photometric bands, the APOGEE DR16 stellar parameters, and, when possible, parallax priors from *Gaia* DR2 (Queiroz et al. 2020). We use the APOGEE DR16 `StarHorse` distances (Queiroz et al. 2020) rather than those that are calculated more purely from parallaxes, such as the Bailer-Jones et al. (2018) distances, because, as of Gaia DR2, these astrometric distances are primarily driven by priors for sources beyond heliocentric distances of 5 kpc (where the parallax uncertainties become too large), and therefore have large uncertainties ($> 20\%$).

Such large uncertainties are problematic for identifying Sgr stream stars given that, at the closest point to the sun, the Sgr stream is still beyond 10 kpc away (Majewski et al. 2003; Koposov et al. 2012), and motivate using spectrophotometric distances, such as the APOGEE DR16 `StarHorse` distances, which maintain an internal precision of $\sim$ 10%, even at distances much larger than 10 kpc. While other spectrophotometric distance catalogs are publicly available, we have chosen the APOGEE DR16 `StarHorse` distance catalog presented in Queiroz et al. (2020) because these distances have been calculated using the new, updated APOGEE DR16 stellar parameters and are available for almost all stars in APOGEE DR16, including the $\sim 170,000$ stars added since the last public data release. Thus, the `StarHorse` distance catalog covers our APOGEE sample more completely and self-consistently than other publicly available spectrophotometric distance catalogs that are limited to smaller APOGEE data releases, older versions of the ASPCAP-derived stellar parameters, or stellar parameters derived from other, unassociated data sets (e.g., Wang et al. 2016; Sanders, & Das 2018; Hogg et al. 2019).

A small fraction of the stars in our sample have `StarHorse` distances that are flagged with poor solutions (due to having poor or high infrared extinction, or too few stellar models from which to estimate distances), so we excise these stars from our sample. Out of the 437,485 unique APOGEE targets, 256,275 are giants that satisfy our spectroscopic quality restrictions, and from which we remove: 2,581 giants because they are identified as globular cluster members, 8,977 giants that fall in fields around the MCs, and finally 2,595 remaining stars with flagged `StarHorse` distances. After applying these quality cuts, our cross-matched sample of APOGEE observed stars with *Gaia* measurements and `StarHorse` distances amounts to 242,122 giants having measured stellar parameters, chemical abundances, radial velocities, proper motions, and distances, from which we identify Sgr stream candidates.

5.3 Tracing the Sgr Stream

5.3.1 Selecting Sgr Stream Candidates

We want to identify Sgr stream members from APOGEE based on their location and kinematics, and now, with the high precision proper motions available from *Gaia* DR2 and spectrophotometric distances from `StarHorse` that are relatively precise even out to large distances, we can find members using full 3D spatial velocities. We calculate the Galactocentric coordinates for our cleaned and cross-matched APOGEE sample, using `StarHorse` distances assuming $R_{\mathrm{GC},\odot} = 8.122$ kpc (Gravity Collaboration et al. 2018). We then include the APOGEE radial velocities and the *Gaia* DR2 proper motions to calculate the 3D heliocentric spatial velocities of these stars using the prescription in Johnson & Soderblom (1987), and convert these to Galactocentric space velocities assuming a total solar motion of $(V_r,\ V_\phi\ V_z)_\odot = (14, 253, 7)$ km s^{-1} in the right-handed velocity notation (Schönrich et al. 2010; Schönrich 2012; Hayes et al. 2018c).

Because the Sgr stream arches across the sky in a near great circle, it has been historically possible to define relatively precisely the orbital plane of the Sgr system without kinematics (Majewski et al. 2003). While we can use the Galactocentric positions and velocities of stars within our sample to identify Sgr stream stars by their general net motion, we can make an even more careful selection of these members by considering their motion with respect to the very well-defined Sgr orbital plane. Therefore, we take the Galactocentric positions and velocities that we have calculated and rotate them into the Sgr orbital plane according to the transformations described in Majewski et al. (2003, here we use the definition of the Galactocentric Sgr coordinates where $\Lambda_{\rm GC} = 0$ is set at the Galactic midplane, sometimes referred to as the Λ_4 coordinate system).[3] This produces a set of position and velocity coordinates (which are most usefully expressed in Cartesian or cylindrical forms) relative to the Sgr orbital plane, rather than to the plane of the Galaxy, but still centered on the Galactic center.

Rather than using a model to predict the location and kinematics expected of Sgr stream stars, we want to use a data-driven selection of these stars, and can then compare them to models as further verification of their membership status. To first order, we can expect that Sgr stream stars should have conserved their orbital angular momentum, and to the accuracy of our data, the orbital angular momentum of Sgr stream stars within our sample should be the same as the orbital angular momentum of known members of the Sgr dSph. APOGEE has observed a considerable number

[3]See also the publicly available code that can be used to perform transformations into the Sgr coordinate systems at `http://faculty.virginia.edu/srm4n/Sgr/code.html`.

of stars in the Sgr core (Majewski et al. 2013; Hasselquist et al. 2017), which we can use to establish the range of orbital angular momenta of the core, and use that range to select stream candidates.

Because the Sgr system is relatively well confined to the nominal Sgr orbital plane (modulo possible precession of the orbital plane; Law et al. 2005; LM10), we should expect that stars in the Stream and the dSph to have conserved the same angular momentum (within our uncertainties), and should not have large velocities perpendicular to the orbital plane. This concept serves as the main selection criteria we employ to select stars in the Sgr dSph and Stream system. We therefore compute the specific angular momentum of stars in our sample along the z-direction of our Galactocentric Sgr coordinates, $J_{\rm zs} = R_{\rm GC,s} \times V_{\phi,\rm s}$ (i.e., the angular momentum perpendicular to the Sgr orbital plane), and in Figure 5.1 show the angular momentum of stars in our sample in this direction versus their velocity perpendicular to the Sgr orbital plane ($V_{\rm z,s}$). Because the Sgr orbital plane is nearly perpendicular to the Galactic plane, most of the APOGEE sample (which is dominated by stars in the disk of the MW near the sun) are rotating with the Galactic disk out of the Sgr orbital plane in the direction of $-V_{\rm z,s}$, and typically have low velocities perpendicular to or radially within the disk of the MW, so they have low velocities in the Sgr orbital plane, and thus a low angular momentum along the direction perpendicular to the Sgr orbital plane.

Known Sgr dSph members from Hasselquist et al. (2017), however, show a relatively large $J_{\rm z,s}$, as seen in Figure 5.1, albeit with a wide spread due to distance uncertainties, but a relatively small velocity perpendicular to the Sgr orbital plane, and identify a range in phase space where we would expect Sgr stream stars to lie. The correlation between $J_{\rm z,s}$ and $V_{\rm z,s}$ in the Sgr core is an artifact of distance uncertainties inflating/deflating the velocity and angular momenta of core members, because the

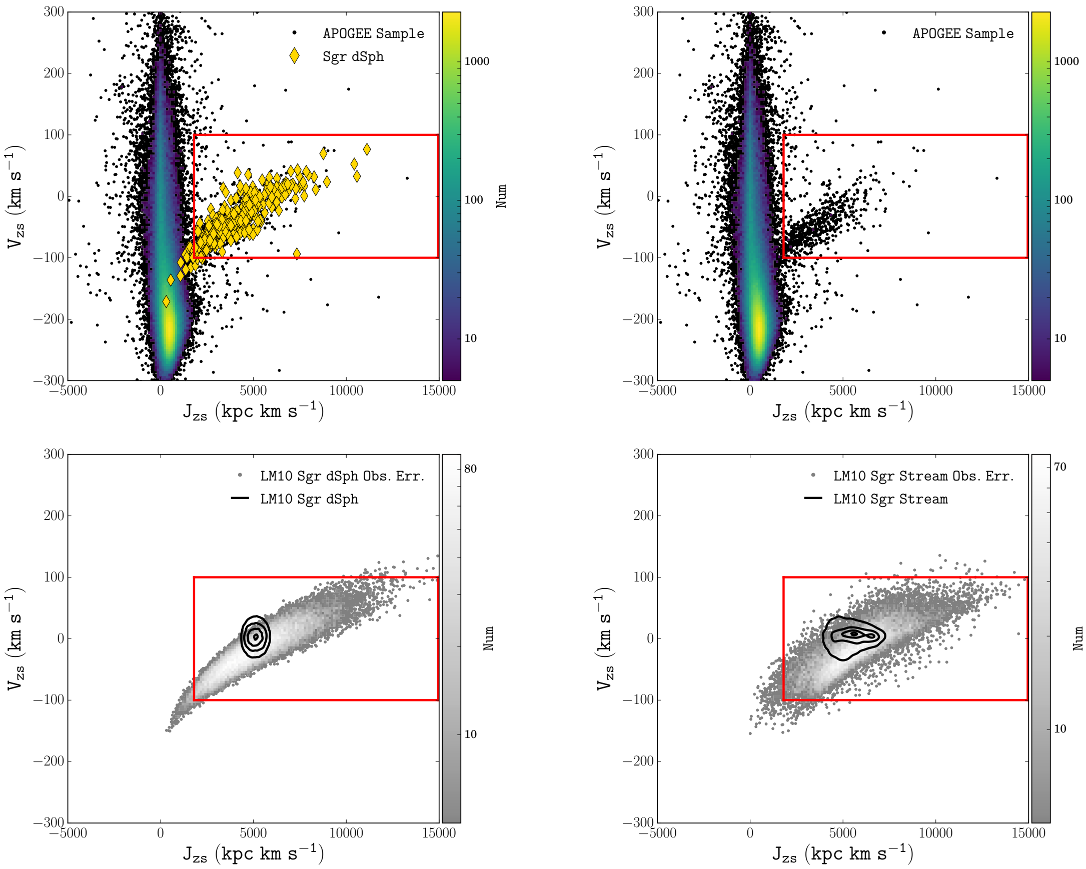

Fig. 5.1.— Velocity of stars (top panels) or LM10 star particles (bottom panels) perpendicular to the Sgr orbital plane, $V_{\rm z,s}$ vs. their angular momentum about the axis perpendicular to the Sgr orbital plane, $J_{\rm z,s}$. (Top panels) APOGEE observed stars with *Gaia* DR2 proper motions and `StarHorse` distances are shown (black points, and 2D histogram for densely populated regions of this space), and the known members of the Sgr core in APOGEE from Majewski et al. (2013) and Hasselquist et al. (2017) are highlighted (gold diamonds in the left panel only). The red box illustrates our initial selection of Sgr stream candidates in this parameter space, and those candidates are shown more clearly in the right panel. (Bottom left panel) The distribution of LM10 Sgr dSph particles (i.e., particles that are still bound in the model) in this projection of phase space (black contours, containing 95%, 68%, 32%, and 5% of the particles, from the outside-in), are shown over top of simulated observations of these particles when they are measured with random 10% distance errors (gray points and 2D grayscale histogram), typical of our `StarHorse` distance uncertainties. (Bottom right panel) Same as the bottom left panel, but now illustrating the effect of 10% distance uncertainties on the distribution of LM10 Sgr stream particles (particles that became unbound within the last three Sgr pericenter passages).

$V_{\rm z,s}$ and $V_{\phi,\rm s}$ in the direction of the Sgr core predominantly come from proper motions, which are nearly constant across the Sgr core, so a spread in distances will produce a correlated spread in $V_{\rm z,s}$ and $V_{\phi,\rm s}$, and thus between the $V_{\rm z,s}$ and $J_{\rm z,s}$ in the core.

The bottom panels of Figure 5.1 show particles from the LM10 model in the $J_{\rm z,s} - V_{\rm z,s}$ plane, and compare their distribution in this projection of phase space when measured perfectly (i.e., with no distance errors) versus how they spread when measured with random 10% distance errors, typical of those in our sample. These simulated observations demonstrate the affects of distance errors alone, yet appear to mimic the observed correlations seen in our distribution of Sgr dSph members. The simulations also illustrate that the stream will, as expected, cover a similar region of this parameter space as the Sgr dSph core, and further justifies that the range of $\rm Z_s$ angular momenta and velocities of known Sgr dSph members can indicate where we may find Sgr stream candidates.

To reduce MW contamination, we use a relatively conservative cut in $J_{\rm z,s}$ to select Sgr system candidates, selecting stars with $J_{\rm z,s} > 1800$ kpc km s^{-1}, and remove stars with velocities perpendicular to the Sgr orbital plane $|V_{\rm z,s}| > 100$ km s^{-1} to isolate only those stars with a low velocity perpendicular to the Sgr orbital plane. To clean out stars that deviate too far from the Sgr orbital plane, we additionally remove any stars that are at Sgr plane latitudes $|B_{\rm GC}| > 20°$. We also remove stars that are within a heliocentric distance of 10 kpc, since the Sgr Stream is known to not come this close to the Sun's position in the MW (Majewski et al. 2003; Belokurov et al. 2014; Hernitschek et al. 2017).

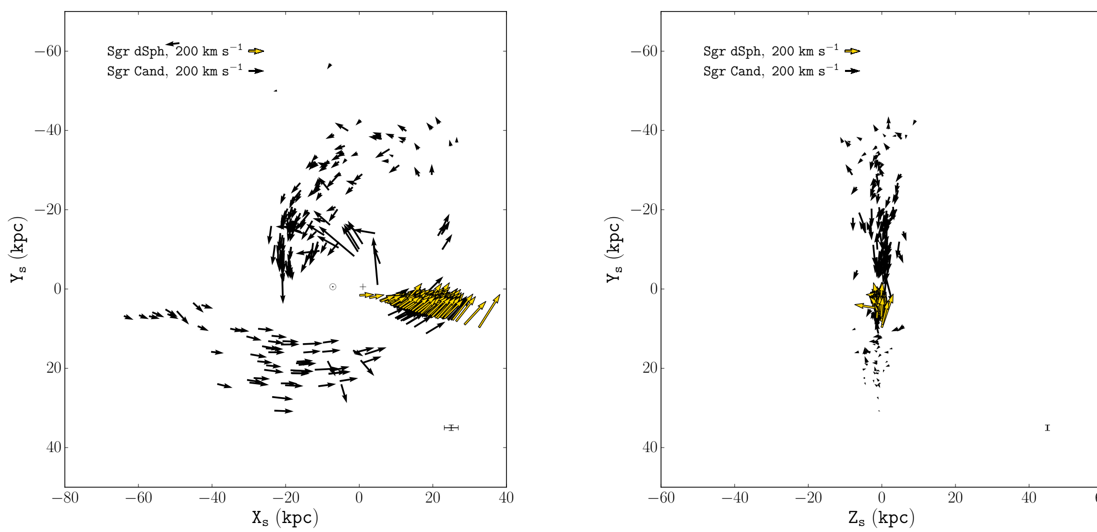

Fig. 5.2.— Velocity plot of the Galactocentric distribution of Sgr stream candidates selected as described in Section 5.3.1 (black arrows), along with known members of the Sgr core (gold arrows; Hasselquist et al. 2017), as projected onto the Sgr orbital plane of $Y_{\rm s}$ vs. $X_{\rm s}$ and the Galactocentric Sgr $Y_{\rm s}$ vs. $Z_{\rm s}$ plane. The median 1σ uncertainty on these positions is shown bottom left-hand corner (the orientation of these uncertainties is dominated by the Sgr dSph core and the typical orientation of uncertainties for a given star will have maximal uncertainty parallel to the sun-star direction). The arrows depict the direction and magnitude of the velocity of these stars in this plane. For reference, the location of the sun and the Galactic center are marked (as an $\odot$ and $+$ symbol respectively). While there appears to be some minor contamination from halo field stars, the bulk of this sample of Sgr stream candidates appear to follow the direction of the Sgr stream with coherent change in the magnitude of velocities along the stream as orbits reach apocenter or pericenter (both in magnitude and direction).

5.3.2 Removing Halo Contamination

This initial selection of Sgr stream candidates is shown in Figure 5.2. The Sgr stream stands out prominently, as the arc of leading arm stars above the disk, $Y_{\rm s} < 0$, and the curve of trailing arm stars below the disk, $Y_{\rm s} > 0$, but is still contaminated by what appear to be remaining halo stars, seen as stars with peculiar velocity vectors, which we want to remove. This potential halo contamination comes in two flavors: (1) stars moving in directions inconsistent with the photometrically implied motion of the Sgr stream (i.e., stars that move nearly perpendicular to the direction of the stream at their location), and (2) stars that are moving in the correct direction, but are still too close to the Sun to be consistent with the location of the stream (despite attempting to remove such contamination by removing stars within 10 kpc of the Sun), even when accounting for distance uncertainties.

Most of the contamination appears to be above the MW disk ($Y_{\rm s} < 0$), and is particularly noticeable at $Y_{\rm s} \sim -10$ kpc, where there is a spread in the $X_{\rm s}$ distribution of our Sgr stream candidates of about 30 kpc, ranging from $X_{\rm s} \sim -30$ kpc to 0 kpc. Because the distance to the stream is known to be $\sim$ 20 kpc or more in this area of the sky (Belokurov et al. 2014; Hernitschek et al. 2017) the spread of stars between $X_{\rm s} \sim -15$ to 5 kpc and $Y_{\rm s} \sim -20$ to -10 kpc are likely to be halo contamination, because they are too close to the Sun.

While some of these stars have motions that are in the correct direction to be consistent with the Sgr stream, even if their StarHorse distances were underestimated, placing them at the distance of the Sgr stream, but keeping their observed proper motions and radial velocities would inflate their space velocities too high for them to be consistent with the rest of the Sgr stream candidates in our sample. We therefore remove the stars that are too close to the Sun, and are only left with potential halo contamination that is not moving in the correct direction of the stream.

The dominant contributors of stream stars above and below the MW disk mid-plane are the leading and trailing arms respectively. Therefore, we would expect stream members to be moving along the direction of the respective arms when we consider stars above and below the disk. Because we imposed an angular momentum requirement to select our Sgr stream candidates, the stars moving in directions that are inconsistent with the stream around them are primarily stars moving perpendicular to the bulk of our candidate sample. However, the arms of the Sgr stream are thought to cross each other, both above and below the disk, and this crossing could yield a smaller set of candidates from the less dense arm in that Galactic hemisphere that move perpendicular to the stars from the more densely populated arm. We want to consider whether we are actually identifying any such stars, or if the stars with peculiar motions are instead contamination from the MW halo.

In the Northern Galactic Hemisphere, above the MW disk ($Y_\mathrm{s} < 0$), the leading arm is the more densely populated arm of the Sgr stream, and in the left panel of Figure 5.2 we do see some stars that are moving perpendicular to the remainder of our stream candidates in this region. The LM10 model predicts that the trailing arm should cross the leading arm above the disk at (X_s, Y_s) $\sim$ (-20, -20) kpc. However, the position of this crossing in the LM10 model is very sensitive to the shape (and possible time-variance) of the MW gravitational potential, and recent studies suggest that the trailing arm instead crosses the leading arm at a point much further above the plane ($\sim$ 50 kpc), or may pass over it entirely (Hernitschek et al. 2017; Sesar et al. 2017). This means that above the MW disk the trailing arm lies in regions where the density of APOGEE targets (and stream candidates) is much lower, and the few stars we see moving perpendicular to the rest of our sample are likely halo contamination.

The crossing of the leading and trailing arms below the MW disk has remained somewhat elusive, with only a few studies suggesting they have observed a few stars in the leading arm below the disk (Majewski et al. 2004; Chou et al. 2007; Carballo-Bello et al. 2017), but there is still no convincing trace of the extent of the leading arm after plunges through the crowded and dust extinguished MW plane. We do find four stream candidates that are moving perpendicular to the bulk of our sample below the disk with roughly the correct position and velocity to be in the leading arm, but given the low number of these stars it is hard to confidently associate them with the Sgr stream. To provide a conservative sample of Sgr stream members, we will not include these candidates in our final sample, but we do note that they may be *bona fide* Sgr Stream members belonging to the leading arm.

To quantitatively remove the aforementioned halo contamination moving in incorrect directions to be members of the Sgr stream, and to remove stars that we cannot confidently associate with the Sgr stream, we assess the candidate stream members' orbital velocity position angle, $\phi_{\mathrm{vel,s}} \equiv \arctan(-V_{\mathrm{x,s}}/-V_{\mathrm{y,s}})$, in the Sgr orbital plane. This orbital velocity position angle is defined to be zero in the $-Y_{\mathrm{s}}$ direction and increasing through the $-X_{\mathrm{s}}$ direction, such that as Sgr moves along its orbit it has an increasing orbital velocity position angle. If the Sgr system were on a perfectly circular orbit, this orbital velocity position angle would be expected to change linearly with Sgr Stream longitude as measured from the Galactic Center, Λ_{GC}; however, because the Sgr orbit is somewhat eccentric, this relation will vary from linearity.

In Figure 5.3 we show the orbital velocity position angle, $\phi_{vel,s}$, of the Sgr core members and Sgr stream candidates as a function of their X_{s} and Y_{s} position in the Sgr orbital plane. Here the leading and trailing arms stand out differently; the leading arm shows a linear distribution in $\phi_{vel,s} - Y_{\mathrm{s}}$ at $Y_{\mathrm{s}} \lesssim 0$ kpc that becomes a

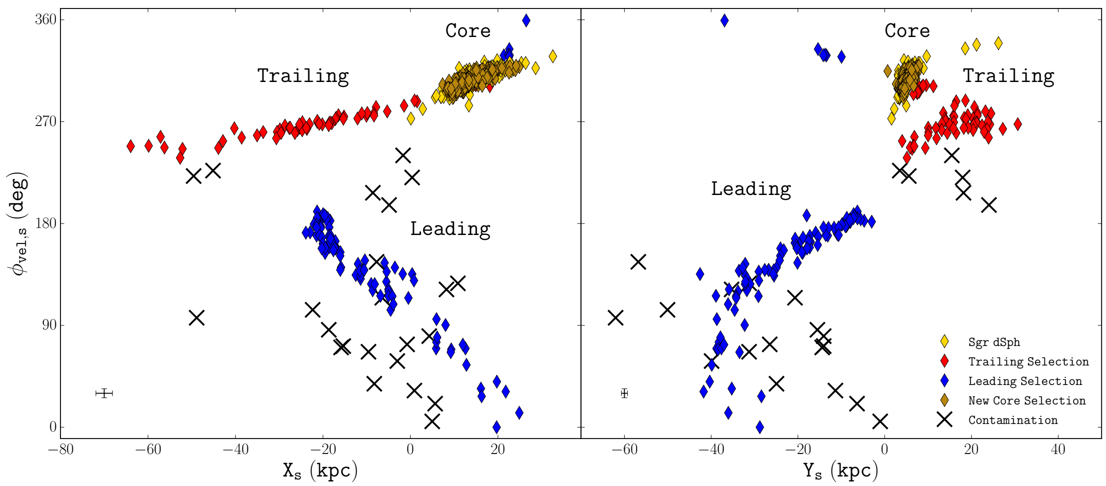

Fig. 5.3.— Orbital velocity position angle, $\phi_{\rm vel,s}$, vs. $X_{\rm s}$ (left panel), and vs. $Y_{\rm s}$ (right panel) of the Sgr stream candidates that have been identified as likely contamination (black crosses), those that are likely real members of the trailing arm and leading arm (red and blue diamonds respectively), new core members (dark yellow diamonds), and known Sgr dSph members (as defined in Figure 5.1). The median 1σ uncertainties on these positions and angles are shown in the bottom left-hand corner, but note that, as in Figure 5.2, the magnitude of the $X_{\rm s}$ and $Y_{\rm s}$ uncertainties change slightly depending on location and these error bars are most representative of stars located in the Sgr core. Stars identified as likely halo contamination move nearly perpendicular to the leading arm at a location where the trailing arm is now established not to cross ($\phi_{\rm vel,s} \sim \pm 90°$ from the overdensity of likely Sgr stream members at a given $X_{\rm s}$ or $Y_{\rm s}$ position) and stand away from the Sgr stream locus in one of these two planes, or lie in regions where the leading arm is thought to pass below the MW disk, but the density of Sgr stream stars is low and has not been clearly traced.

more tenuous distribution around $Y_{\rm s} \sim 40$ kpc, whereas the trailing arm has a very tight and nearly linear distribution in $\phi_{vel,s} - X_{\rm s}$, but is clumped in the $\phi_{vel,s} - Y_{\rm s}$. To remove potential halo contamination, we remove any of the Sgr stream candidates that deviate significantly from the stream loci in one of these two planes, and mark which stars have been removed.

These Sgr stream member selections on orbital velocity position angle have been applied to remove the stars most inconsistent with our simple hypothesis that the stream should be dynamically coherent, but we can also compare this final selection of stars with the LM10 model to further justify our criteria. In Figure 5.4 we compare the $\phi_{vel,s}$ as a function of Sgr longitude as seen from the Galactic Center, $\Lambda_{\rm GC}$, for both our selected sample of Sgr stream stars and the likely MW halo contamination as identified above to predictions from the LM10 model.

This comparison shows that the final Sgr stream sample is not only very tightly coherent in its distribution, but that it closely follows the predictions of the model, which is reassuring given that this requires a precise combination of the observed distances, proper motions, and radial velocities in the data. Additionally we see that the stars labeled as likely contamination, by and large, deviate much more significantly from the model. While there are a few contaminant stars that do line up with the model, they do so along parts of the stream that are poorly modeled/constrained or they physically lie in regions of the halo where the stream (and the rest of our sample) does not pass.

Our final selection identifies 518 new members of the Sgr system in the APOGEE survey, including 133 new Sgr stream stars and 385 new Sgr dSph core stars, and we recover 33 of the 35 metal-rich APOGEE Sgr Stream members found by Hasselquist et al. (2019) through chemical tagging. The advantage here is that our kinematic

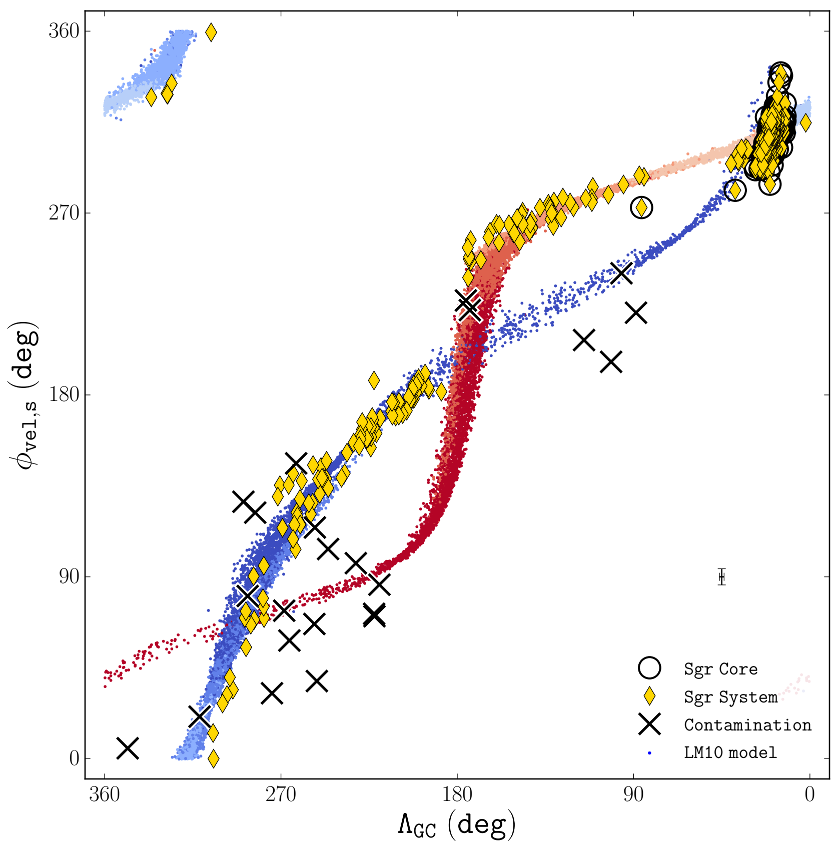

Fig. 5.4.— Orbital velocity position angle, $\phi_{\rm vel,s}$, vs. Galactocentric Sgr longitude, $\Lambda_{\rm GC}$ for the final sample of stars selected to be members of the Sgr system (gold diamonds, with the previously known Sgr dSph core members circled in black), and the Sgr stream candidates that were identified as likely halo contamination (black crosses), compared to particles from the LM10 Sgr model (colored points), with the median uncertainty on these angles shown as the errorbar to the lower right (above the legend). The LM10 model points have been colored to identify the leading (blue) and trailing (red) arms with darker saturation corresponding to dynamically older material, stripped off of the Sgr galaxy during earlier pericenter passages. Even though this was not originally a criterion for selection, the Sgr stream members that have been selected via Figure 5.3 closely follow the expectations from the LM10 model, whereas the stars identified as halo contamination deviate more significantly, or lie in regions where the LM10 model is known to not reproduce observations (namely the dynamically oldest parts of the trailing arm).

selection now allows us to push below the [Fe/H] ~ -1.2 metallicity that was the limit for the chemical tagging, below which the chemical abundance profile of Sgr begins to blend with that of the MW halo (Hasselquist et al. 2019). The two remaining stream stars that Hasselquist et al. (2019) found were not recovered because they lack distances measurements in this APOGEE data release.

To constitute a more complete census of the Sgr system that we analyze throughout the rest of this chapter, we combine this sample of new members with (1) the 325 known Sgr dSph stars from Hasselquist et al. (2017) that pass our spectroscopic and distance requirements (299 of which we recover through our Sgr selection; the remaining 26 are excluded by our $J_{\rm z,s} - V_{\rm z,s}$ cuts to avoid MW contamination, as seen in Figure 5.1), and (2) the 33 Sgr stream stars from Hasselquist et al. (2019) that we recover. This gives a total sample of 876 APOGEE observed stars in the Sgr system, the largest sample of Sgr stars with high-resolution spectra to date. Of the 166 Sgr Stream stars, 103 of them are in the leading arm, and 63 are in the trailing arm.

The distribution of this full Sgr sample throughout the Galactocentric Sgr coordinate system is shown in Figure 5.5 overlying the LM10 model of the Sgr Stream pulled off of the main body within the past three pericenter passages ($P_{col} \leq 3$), with arrows illustrating the magnitude and direction of each star's velocity projected onto these planes. Despite not being selected in accordance with the LM10 model, we can see that on average, our Sgr Stream sample aligns well with the LM10 model in terms of shape and distance for the most part, however, there are two differences: (1) The width of the Sgr stream in our observed sample appears to be slightly inflated in some places due to distance uncertainties that spread stars along the radial direction from the sun (although these distances seem to be precise enough to differentiate the narrower width of the leading arm and against wider trailing arm at their points near-

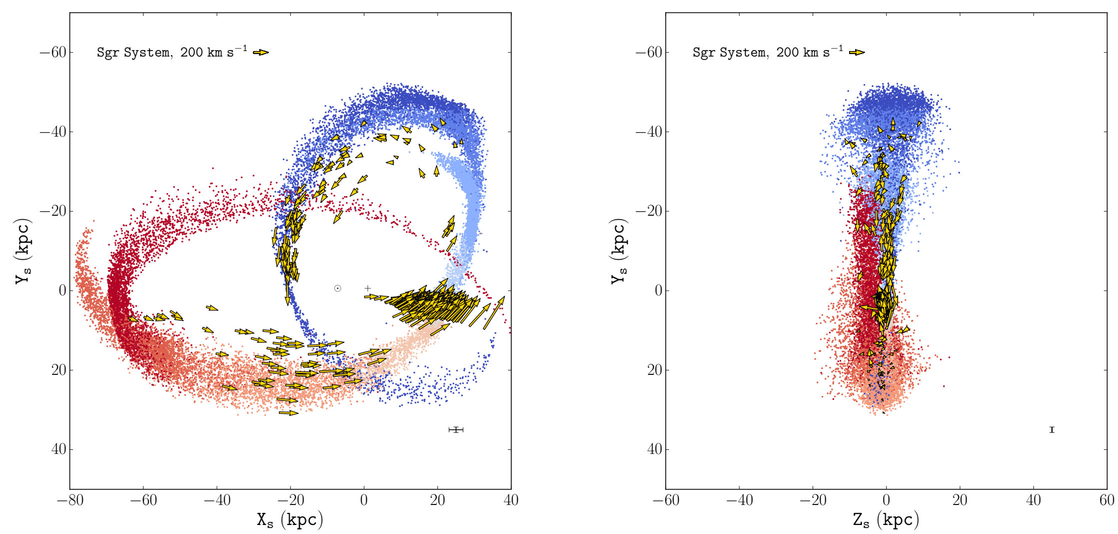

Fig. 5.5.— (Left panel) Y_s vs. X_s and (right panel) Y_s vs. Z_s projections of the Galactocentric Sgr orbital coordinate system with the distribution of our final sample stars in the Sgr system shown with arrows depicting their projected velocities, and overlaid on particles from the LM10 N-body model, colored as in Figure 5.4. For reference, the location of the sun and the Galactic center are marked (as an $\odot$ and $+$ symbol respectively), and the typical positional uncertainties are shown as the errorbar in the bottom right-hand corner as in Figure 5.2. The positions and velocity vectors of the Sgr stream stars in this sample closely follow the distribution from the LM10 model (within the typical $\sim 10\%$ median distance uncertainties), although the Sgr dSph stars appear to be at systematically closer distances than the model and past distance measurements of Sgr dSph.

est the sun), and (2) there appears to be a difference in the distance scale between the observations and the LM10 model, particularly at the Sgr dSph core and at the apocenter of the leading arm, such that the observed distances are measured closer to the Sun on average.

The median distance to the Sgr core in our sample is about 23 kpc, with a dispersion of $\sigma = 4$ kpc, whereas past studies find slightly larger distances, ranging from 24-28 kpc (Monaco et al. 2004; Siegel et al. 2007; McDonald et al. 2013; Hernitschek et al. 2019), although we note that our median distance to the Sgr core is still within about 1σ of these previously measured distances. One possible source of our smaller distances to the Sgr core, may be the bulge priors used in calculating `StarHorse` distances. To account for the higher density of stars in the Galactic bulge when calculating `StarHorse` distances, Queiroz et al. (2018) incorporate a prior for stars in the direction of the Galactic Center to lie at distances that place them in the bulge. Because the Sgr dSph core lies opposite the bulge from the Sun, it lies in a part of the sky where this prior is relevant for MW stars, but it may be skewing the distances of Sgr stars to smaller values.

However, we can see that the distances to other parts of the stream are also skewed to smaller values than in the LM10 model (by $\sim 15-20\%$). This may suggest that the Queiroz et al. (2018) values are systematically underestimated at these large distances, or that the LM10 model overestimates the distances to the Sgr system (for which there is some evidence in comparison with the distribution of Sgr stream RR Lyrae, which find slightly closer distances for the apocenter of the leading arm Hernitschek et al. 2017). Regardless, neither possibility should have serious impact on the results that follow, because we use the distance independent heliocentric Sgr longitudinal coordinate system for the remaining analysis.

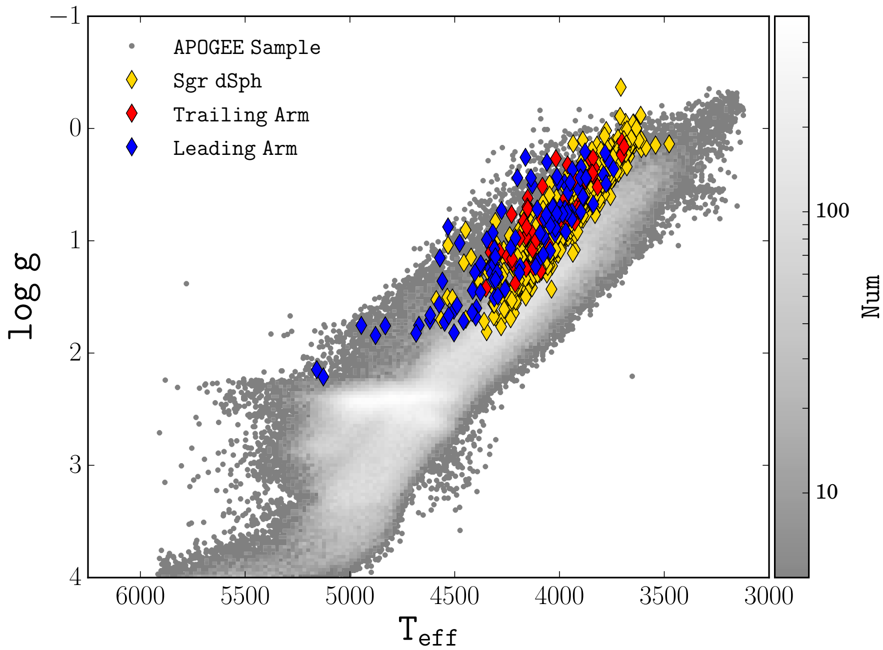

Fig. 5.6.— Spectroscopic Hertzsprung-Russel Diagram, showing calibrated log g vs. $T_{\rm eff}$ for our Sgr dSph core (gold diamonds), trailing arm (red diamonds), and leading arm samples (blue diamonds), compared to the remainder of APOGEE giants that meet the quality criteria described in Section 5.2 (black points and 2D histogram where densely populated).

Our final sample of Sgr stars (core and stream) are given in Table 5.1, along with their positions, kinematics, stellar parameters and chemical abundances (for the elements explored in below in Section 5.4), as well as, the source of their identification as members of the Sgr system, and their classification as core, trailing arm, or leading arm members. The stellar parameters for our sample of Sgr stars are shown in the spectroscopic Hertzsprung-Russel diagram in Figure 5.6, in comparison to the rest of the APOGEE giants that satisfy the quality requirements described in Section 5.2. While we have not applied any temperature cuts prior to this point, as mentioned in Section 5.2, for the following analysis in Section 5.4, we restrict this sample to calibrated temperatures warmer than 3700 K, where APOGEE's stellar parameters and chemical abundances are most reliably and consistently determined for giants. This only minimally reduces our sample of Sgr stream and core stars, and additionally does not seem to significantly affect our results as discussed in Section 5.4.1.

5.4 Chemistry Along the Sgr Stream

5.4.1 Metallicity Differences between Sgr dSph and Sgr Stream

The combination of the identified Sgr stream members and dSph core sample allows us to explore the chemistry of the complete Sgr system, to the extent that the extant stream so far identified represents all stripped populations. It is immediately evident in Figure 5.7 that the metallicity in each arm of the Sgr stream is lower than that of the Sgr dSph core. The median metallicity of the dSph sample is measured to be $[\mathrm{Fe/H}]_{\mathrm{dSph}} = -0.57$, whereas the median metallicity of our trailing and leading arm samples are $[\mathrm{Fe/H}]_{\mathrm{trailing}} = -0.84$ and $[\mathrm{Fe/H}]_{\mathrm{leading}} = -1.13$ respectively. Performing a Kolmogorov-Smirnov (KS) test to compare the metallicity distributions of the

Table 5.1. Properties of Sgr Stars

Column	Column Label	Column Description
1	APOGEE	APOGEE Star ID
2	RAdeg	Right Ascension (decimal degrees)
3	DEdeg	Declination (decimal degrees)
4	GLON	Galactic Longitude (decimal degrees)
5	GLAT	Galactic Latitude (decimal degrees)
6	LAMBDA_sun	Heliocentric Sagittarius Longitude, $\Lambda_{\odot}$ (decimal degrees)
7	BETA_sun	Heliocentric Sagittarius Latitude, $B_{\odot}$ (decimal degrees)
8	LAMBDA_GC	Galactocentric Sagittarius Longitude, $\Lambda_{\rm GC}$ (decimal degrees)
9	BETA_GC	Galactocentric Sagittarius Latitude, $B_{\rm GC}$ (decimal degrees)
10	Jmag	2MASS J magnitude
11	Hmag	2MASS H magnitude
12	Kmag	2MASS Ks magnitude
13	Dist	Heliocentric distance (kpc)^a
14	e_Dist	Uncertainty in distance^a(kpc)
15	HRV	Heliocentric radial velocity (km s^{-1})
16	e_HRV	Radial velocity uncertainty (km s^{-1})
17	pmRA	Proper motion in RA (mas yr^{-1})
18	e_pmRA	Uncertainty on pmRA (mas yr^{-1})
19	pmDE	Proper motion in Dec (mas yr^{-1})
20	e_pmDE	Uncertainty on pmDE (mas yr^{-1})
21	X_s	Sgr Galactocentric Cartesian $X_{\rm s}$ position (kpc)
22	Y_s	Sgr Galactocentric Cartesian $Y_{\rm s}$ position (kpc)
23	Z_s	Sgr Galactocentric Cartesian $Z_{\rm s}$ position (kpc)
24	R_cys	Sgr Galactocentric Cylindrical radius, $R_{GC,s}$ (kpc)
25	V_xs	Sgr Galactocentric Cartesian $X_{\rm s}$ velocity, $V_{\rm x,s}$ (km s^{-1})
26	V_ys	Sgr Galactocentric Cartesian $Y_{\rm s}$ velocity, $V_{\rm y,s}$ (km s^{-1})
27	V_zs	Sgr Galactocentric Cartesian $Z_{\rm s}$ velocity, $V_{\rm z,s}$ (km s^{-1})
28	V_rs	Sgr Galactocentric Cylindrical radial velocity, $V_{\rm r,s}$ (km s^{-1})
29	V_phis	Sgr Galactocentric Cylindrical rotational velocity, $V_{\phi,\rm s}$ (km s^{-1})
30	SNR	Signal-to-noise ratio of spectrum per pixel in APOGEE DR16^a
31	Teff	DR16 effective surface temperature (K)^a
32	e_Teff	DR16 uncertainty in $T_{\rm eff}$ (K)^a
33	logg	DR16 surface gravity^a
34	e_logg	DR16 uncertainty in $\log g^a$
35	Vturb	DR16 microturbulent velocity (km s^{-1})^a
36	Vmacro	DR16 macroturbulent velocity (km s^{-1})^a
37	[Fe/H]	DR16 log abundance, [Fe/H]^a
38	e_[Fe/H]	DR16 uncertainty in [Fe/H]^a
39	[Mg/Fe]	DR16 log abundance, [Mg/Fe]^a
40	e_[Mg/Fe]	DR16 uncertainty on [Mg/Fe]^a
41	[Si/Fe]	DR16 log abundance, [Si/Fe]^a
42	e_[Si/Fe]	DR16 uncertainty on [Si/Fe]^a
43	t_un	Dynamical age estimated from the LM10 model, $t_{\rm unbound}$ (Gyr)^b
44	MEMBERSHIP	Identifies stream or core membership^c
45	STUDY	Identifies the source of membership with the Sgr system^d

Note. — Table 1 is published online in Hayes et al. (2020). The columns are shown here for guidance regarding its form and content.

Note. — Null entries are given values of -9999.

[a]Publicly released in SDSS-IV DR16 (Ahumada et al. 2020; Jönsson et al. in prep.)

[b]Dynamical ages of -1 refer to stars that are still bound to the Sgr dSph core.

[c]Stars are listed with a membership of “core,” “trailing,” or “leading,” depending on if they are members of the Sgr dSph core, trailing arm, or leading arm, respectively.

[d]Stars are listed with an associated study of “Has17,” “Has19,” or “Hay19,” to denote that they were identified as members of the Sgr system in Hasselquist et al. (2017), Hasselquist et al. (2019), or this work, respectively

Sgr core, trailing arm, and leading arm samples indicates a 1% probability that the metallicity distributions of the trailing and leading arm samples are drawn from the same distribution, and a much lower probability ($\ll 1\%$) that either the trailing arm or leading arm samples are drawn from the same metallicity distribution as the Sgr dSph core.

Figure 5.5 and Section 5.4.4 illustrate that, by comparison with the LM10 model, our trailing arm sample falls along ranges of the stream predicted to be stripped off of Sgr during the past pericenter passage or two, and is therefore dynamically younger than the leading arm sample that primarily traces material, which was stripped off three pericenter passages ago (i.e., the trailing arm sample traces lighter portions of the model than the deeper saturated parts where the leading arm sample lies). Comparing the median metallicities of the three samples shown in Figure 5.7 to their relative dynamical ages makes it clear that there is a correlation between dynamical age and metallicity, such that dynamically older material is, on average, more metal poor. Figure 5.7 also shows the α-element distributions of these samples, which is discussed more in Section 5.4.3.

Assuming that tidal stripping works predominantly outside-in, these dynamical ages roughly trace back to different depths within the Sgr progenitor. Thus, our leading arm sample would represent the outermost/least bound stars in the progenitor, whereas our trailing arm sample comes from more intermediate radii. In the presence of an initial metallicity gradient within the Sgr progenitor, we would expect that our leading arm sample would have a lower metallicity population than the stars from our trailing arm, consistent with our findings.

We first note that our [Fe/H] ~ -0.57 dex value for the median metallicity in the Sgr dSph is somewhat more metal poor than past measurements around [Fe/H]

~ -0.4 (e.g., Monaco et al. 2005; Chou et al. 2007), and we also find similar differences for the metallicities of the trailing and leading arms. They are again somewhat more metal-poor than reported by earlier studies of the metallicity in the Sgr stream (particularly in the leading arm), which found the trailing arm to have a metallicity of [Fe/H] ~ -0.6 and the leading arm to be in the range of [Fe/H] ~ -0.7 to -0.8 in the regions of the stream that we observe (Chou et al. 2007; Monaco et al. 2007). While the new APOGEE results are closer to the metallicities of the trailing ($[\mathrm{Fe/H}]_{\mathrm{trailing}} = -0.68$) and leading ($[\mathrm{Fe/H}]_{\mathrm{leading}} = -0.89$) arms found by Carlin et al. (2018), the latter are still slightly more metal rich than we find.

While we apply a temperature cut (which would tend to bias our sample to slighly lower metallicities) to our Sgr sample at 3700 K to measure these median metallicities, this has less than 0.01 dex affect on the median metallicity of our core sample (compared to when we include core stars cooler than 3700 K), and only removes one star from our trailing arm stream sample that has a negligible effect on the median metallicity of this sample. In neither the stream nor the core samples, does this temperature restriction produce a significant enough bias to low metallicities to account for the differences between the values we measure and those reported in past studies.

Instead, the higher metallicities may be because these past studies targeted M giants, which are very effective tracers of the Sgr stream in the MW halo (Majewski et al. 2003), however, M giants are also more metal rich than warmer, bluer K giants (which are more affected by halo contamination and so have received less attention). Thus, the measurements from these earlier M giant studies were biased to higher metallicities, although the presence of more metal-poor Sgr stream populations was evident through the blue horizontal branch (BHB) and RR Lyrae stars identified in the stream (Bellazzini et al. 2006; Yanny et al. 2009; Sesar et al. 2010).

In Figure 5.8 we show the M_H versus $J-K$ CMD for 3 Gyr and 12 Gyr PARSEC isochrones (Bressan et al. 2012), a range of ages that might be expected in the Sgr stream based on population synthesis of the core (Siegel et al. 2007), and assuming there are no stars in the stream that were born after Sgr began to be stripped, and a range of metallicities is shown for each age. The $J-K$ color limits utilized by different studies to select M giants are also shown in Figure 5.8. Most studies that targeted M giants employed a $(J-K)_0 \geq 0.85$ color cut, either using the Sgr Stream M giant selection from Majewski et al. (2003) or reproducing a similar selection (Monaco et al. 2007; Keller et al. 2010; Carlin et al. 2018), although Chou et al. (2007) targeted even redder stars using a $(J-K)_0 \geq 1.0$ selection. Comparing these color selections with the PARSEC isochrones, we can see that RGB stars with metallicities [Fe/H] $\lesssim -1.5$ would be excluded almost entirely, regardless of their age, and even at a metallicity of -1, only stars at the tip of the RGB would be included in such targeting. At higher metallicities, a larger span of the RGB is included within the color selection, so, not only do these color selections exclude the lowest metallicity stars, they also bias the sample to higher metallicities, because metal-rich giants can be selected over a larger range of absolute magnitude or stellar parameters.

In this work, we have a serendipitous targeting of Sgr stream giants throughout the APOGEE survey, rather than a targeting of M giants specifically. Most of the Sgr stream candidates are in halo fields that have a color selection criterion of $(J-K)_0 \geq 0.3$, although even in designated disk fields the blue edge of target selection is only $(J-K)_0 \geq 0.5$. Given the much more liberal selection, our sample should be far less affected by metallicity bias than M giant samples, which likely explains our lower metallicities for the Sgr stream.

The Sgr core was targeted more intentionally by APOGEE, and represents a combination of target selections. The original selection of Sgr core stars in APOGEE-1 is a mix of M giants satisfying the Majewski et al. (2003) selection criteria and known Sgr core members identified by Frinchaboy et al. (2012) with a slightly less conservative color selection (Zasowski et al. 2013). These have been supplemented in APOGEE-2 by newly observed Sgr core stars that have a more liberal color selection, $(J-K)_0 \geq 0.5$, and are less biased to high metallicities. This combination of different selection criteria allows us to probe a similar range of metallicities in the Sgr core to that of our stream sample, however the mix of selection criteria make it difficult to determine what metallicity bias may be present in our Sgr core sample. We therefore note that there may be some bias in our core sample, although it should be less extreme than a strict M giant color selection, such as that utilized in Majewski et al. (2003).

As a demonstration of this bias, if we impose a $(J-K)_0 \geq 0.85$ selection to our Sgr stream sample, we increase the median metallicity of our core, trailing, and leading arm samples by around 0.1 dex, to [Fe/H] = −0.52, −0.73, and −0.97 respectively, values that are in better agreement with these M giant studies, especially the recent study from Carlin et al. (2018). Any remaining differences in the Sgr stream are likely due to stochastic variations or possibly the result of spatial biases that favor particular parts of the stream from which they have been drawn.

5.4.2 Metallicity Gradients Along the Sgr Stream

Metallicity Gradients in the APOGEE Sample

The metallicity differences between the Sgr dSph and the trailing and leading arms suggest that there may be metallicity *gradients* along the Sgr stream. In the top panel of Figure 5.9, we show the metallicity of stars in our sample as a function of

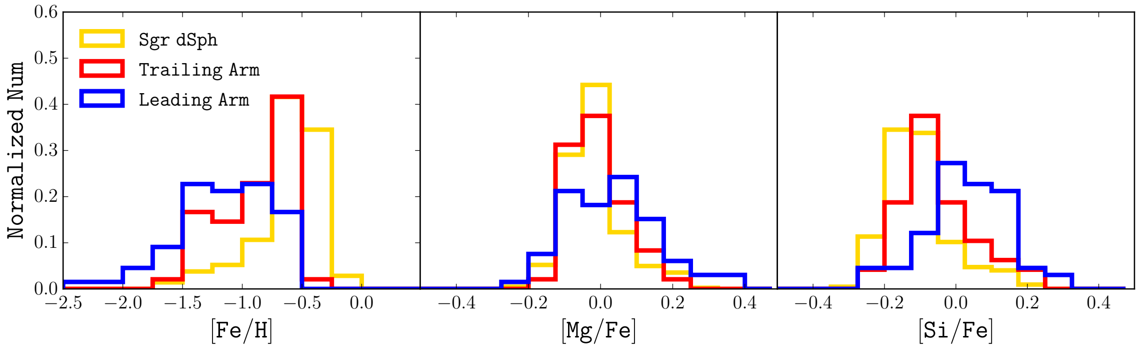

Fig. 5.7.— Metallicity, [Fe/H] (left), [Mg/Fe] (middle), and [Si/Fe] (right) distributions of stars in the Sgr dSph core (gold), trailing arm (red), and leading arm (blue), normalized by the number of stars within each sample. While the metallicity and [α/Fe] distributions are generally non-Gaussian, with tails toward lower metallicties and higher [α/Fe], the metallicity decreases and the [α/Fe] ratio increases when moving from the still bound Sgr dSph stars, through the dynamically younger trailing arm sample, to the dynamically older leading arm sample.

Table 5.2. Chemical Gradients Along the Sgr Stream

Element	Method / Units	Anchored[a] dex deg^{-1} Trailing Arm	Anchored[a] dex deg^{-1} Leading Arm	Internal[b] dex deg^{-1} Trailing Arm	Internal[b] dex deg^{-1} Leading Arm	Dynamical Age[c] dex Gyr^{-1} Full Stream
[Fe/H]		$(2.6 \pm 0.4) \times 10^{-3}$	$(4.0 \pm 0.3) \times 10^{-3}$	$(1.2 \pm 0.9) \times 10^{-3}$	$(1.4 \pm 1.4) \times 10^{-3}$	0.12 ± 0.03
[Mg/Fe]		$(0.2 \pm 0.1) \times 10^{-3}$	$(0.5 \pm 0.1) \times 10^{-3}$	$(0.3 \pm 0.2) \times 10^{-3}$	$(0.8 \pm 0.5) \times 10^{-3}$	0.02 ± 0.01
[Si/Fe]		$(0.5 \pm 0.1) \times 10^{-3}$	$(1.1 \pm 0.1) \times 10^{-3}$	$(0.2 \pm 0.3) \times 10^{-3}$	$(0.9 \pm 0.4) \times 10^{-3}$	0.04 ± 0.01

[a]The gradient measured along each arm of the stream when anchoring the gradient by the chemistry of the Sgr dSph core.

[b]The gradient measured internally within each arm of the stream excluding the chemistry of the Sgr dSph core.

[c]The gradient measured within the Sgr stream as a function of the estimated dynamical ages (i.e., stripping times) of Sgr stream stars and combining both arm samples. See Section 5.4.4 for details.

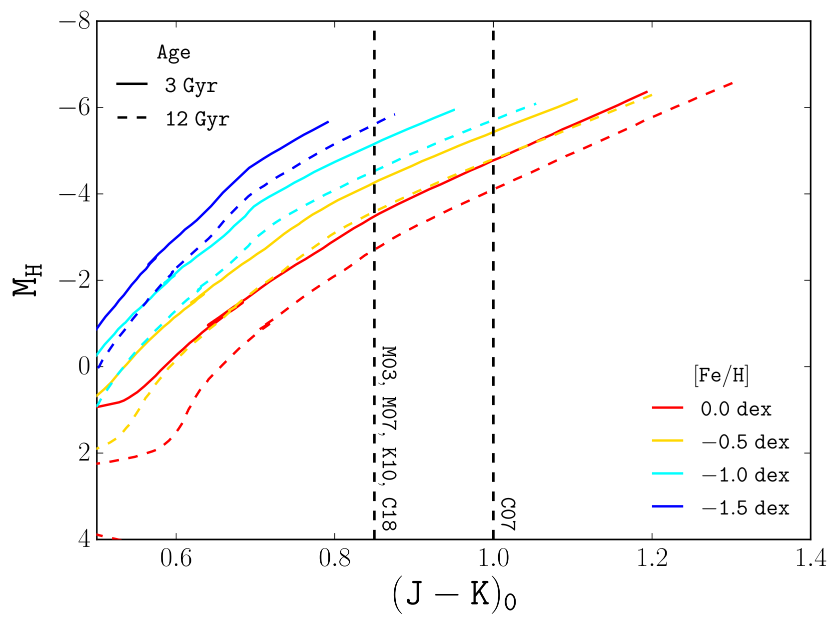

Fig. 5.8.— M_H vs. J-K CMD of PARSEC isochrones (Bressan et al. 2012) at ages of 3 Gyr (solid lines) and 12 Gyr (dashed lines), which cover the range of ages expected in the Sgr stream, and for metallicities of [Fe/H] = 0.0, −0.5, −1.0, and −1.5 dex (red, gold, cyan, and blue respectively). The black dashed lines show the blue edge of color cuts used in past Sgr stream studies to select M giants, at $(J-K)_0 \geq 0.85$ (Majewski et al. 2003; Monaco et al. 2007; Keller et al. 2010; Carlin et al. 2018, labeled M03, M07, K10, and C18 respectively), and at $(J-K)_0 \geq 1.0$ (Chou et al. 2007, labeled as C07). These color selections bias Sgr stream samples to higher metallicities, because low metallicities, [Fe/H] $\lesssim -1.5$, are almost entirely excluded, and higher metallicity RGBs have a larger stellar parameter coverage with these color limits.

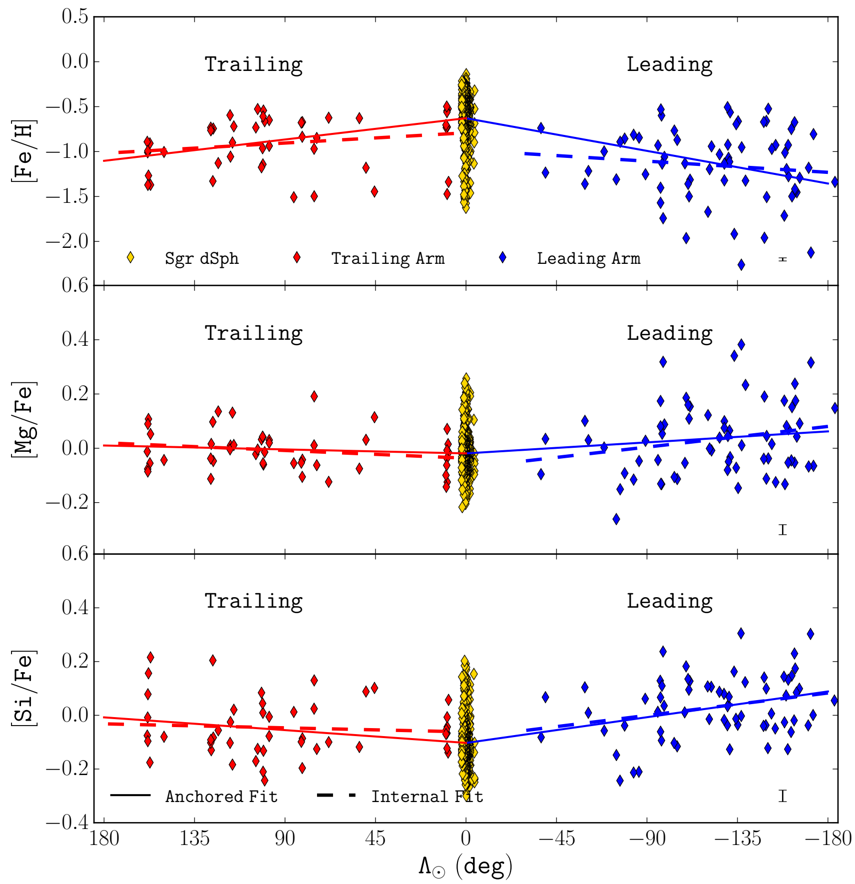

Fig. 5.9.— Metallicity, [Fe/H] (top), [Mg/Fe] (middle), and [Si/Fe] (bottom) vs. solar-centered Sgr longitude, $\Lambda_{\odot}$, of Sgr dSph (gold), trailing arm (red), and leading arm (blue) stars. These distributions have been fit assuming a linear metallicity and abundance gradient with $\Lambda_{\odot}$ through the trailing (red line) and leading (blue line) arms, when anchored by the chemistry of the Sgr dSph core (solid line) and when only measured internally along the stream (dashed line). The median uncertainty on each elemental abundance in our sample is shown as the errorbar in the bottom right-hand corner to illustrate the typical uncertainties. The gradients anchored by the chemistry of the Sgr dSph core are flatter along the dynamically younger trailing arm, qualitatively consistent with expectations of tidally stripping a Sgr progenitor galaxy having initial radial metallicity and α-element abundance gradients. The internal gradients within each of the arms are both flatter than the gradients that are measured when anchoring them to the chemistry of the Sgr dSph core, consistent with the limited dynamical age range within the samples of each arm.

their Sgr longitude ($\Lambda_\odot$). Despite the relatively large (astrophysical) scatter in the samples of each arm, there do appear to be gradients in the metallicity along each arm, depending on how the gradients are measured. Considering each separately, we fit the metallicity of the Sgr member stars with a linear trend as a function of Sgr longitude anchored at the Sgr dSph core (by including Sgr stream and core members in the fits) to measure metallicity gradients and their uncertainties (i.e., the formal error from linear regression, not including the uncertainties on each abundance, since these smaller than the intrinsic dispersion, and therefore do not accurately capture said dispersion), which are reported in the first row of Table 5.2 under the “Anchored” gradient measurement method, for the trailing and leading arms respectively.

If the original Sgr progenitor galaxy had a spatial metallicity gradient (with a larger fraction of higher metallicity stars more interior/tightly bound), then on average, with stripping assumed to proceed from the outermost part of the progenitor galaxy to smaller radii, lower metallicity stars would tend to be stripped off of the Sgr progenitor at earlier times and higher metallicity stars would be stripped during successive pericenter passages, and this process would naturally produce gradients along the stream. Because there is a better energy sorting along the trailing arm, such that debris of different dynamical ages are more spread out along the extent of the trailing arm (Chou et al. 2007; Keller et al. 2010; Niederste-Ostholt et al. 2012), the stars pulled off during successive pericenter passages are more clearly delineated in the trailing arm than the leading arm. Therefore, the distribution of dynamical age along the trailing arm is more extended on the sky, so that observationally the metallicity gradient along the trailing arm should be shallower than along the leading arm, as seen here.

The Sgr core is known to have undergone star formation and enrichment after the tidal stripping of the Sgr progenitor began (Siegel et al. 2007), therefore, internal gradients within the tidal debris of the Sgr stream may be more indicative of radial metallicity gradients within the Sgr progenitor than measuring gradients anchored by the present-day Sgr dSph core. Fitting a linear trend to the metallicity of our trailing and leading arm samples again as a function of Sgr longitude, but now excluding the Sgr dSph core, we find that these internal gradients are much flatter and typically more uncertain than what we find when requiring the stream gradients to be anchored by the Sgr dSph core (see Table 5.2 under "Internal" gradient measurement method column). In the leading arm, in particular, our sample is consistent (to within 1σ) with no internal metallicity gradient.

As mentioned above, our leading arm sample (as well as most literature samples of the leading arm) is dominated by dynamically older material that was likely stripped off approximately three pericenter passages ago. Because the majority of our leading arm sample was stripped around the same time, these stars should be a fairly homogeneous population likely tracing the outermost regions of the Sgr progenitor, even though they are spread out over a large region of the sky. While this leading arm sample is more metal poor than our trailing arm sample, it covers less breadth in its dynamical age, and therefore has a shallower (or negligible) internal metallicity gradient. By reference to the LM10 model in Figure 5.5, our trailing arm sample covers a couple pericenter passages in dynamical age, and may therefore have a non-negligible internal metallicity gradient.

Comparison with the Literature

Studies measuring metallicity gradients along the Sgr stream in the Literature report a mix of what we have called "anchored" and "internal" gradients along the Sgr stream. Considering first the studies that report metallicity gradients anchored by the metallicity of the Sgr core, our metallicity gradients are in good agreement with the results from Keller et al. (2010) and Hyde et al. (2015), who find gradients of $(2.4 \pm 0.3) \times 10^{-3}$ dex deg^{-1} (Keller et al. 2010) and 2.7×10^{-3} dex deg^{-1} (Hyde et al. 2015)[4], respectively. While Keller et al. (2010) exclusively studied the trailing arm, Hyde et al. (2015) also measure metallicities for a sample of leading arm stars, however, due to the large metallicity dispersion they found and the metallicity differences between their sample and the leading arm sample from Chou et al. (2007), they do not report any metallicity gradient along the leading arm.

Carlin et al. (2012) and Shi et al. (2012) both report internal metallicity gradients that they measure, excluding the core, using samples that cover a similar angular extent to that which is covered by our sample. From low-resolution spectroscopy of stars in six fields along the Sgr trailing arm ranging from $\Lambda_{\odot} = 70^{\circ} - 130^{\circ}$, Carlin et al. (2012) find metallicities slightly more metal poor than we find in this range of the stream, but that exhibit a metallicity gradient of 1.4×10^{-3} dex deg^{-1} like we find in our sample. Again, like we find with our trailing arm sample, they suggest that this internal gradient is relatively uncertain, and their sample also seems to be relatively consistent with no internal gradient.

Using a sample of stars selected from the Sgr stream observed with SDSS DR7 spectroscopy, Shi et al. (2012) measured a metallicity gradient $(1.8 \pm 0.3) \times 10^{-3}$ dex deg^{-1} along the trailing arm, similar to ours and Carlin et al. (2012) along the trailing arm. Within uncertainties, the gradient Shi et al. (2012) measure along the trailing arm is the same or steeper than the metallicity gradient of $(1.5 \pm 0.4) \times 10^{-3}$ they found along their leading arm sample. Given the large uncertainty that we have on the

[4] This is an estimated gradient based on their measurement of a mean core metallicity of [Fe/H] = -0.59, which drops to an average metallicity of [Fe/H] = -0.97 in a trailing arm sample 142° away from the core

internal gradient along the leading arm, this too is consistent with our measurement.

5.4.3 α-element Abundance Gradients along the Sgr Stream

In addition to exploring metallicity gradients, Keller et al. (2010) also measured [O/Fe] and [Ti/Fe] abundances for their sample of stream stars, but report little-to-no measureable α-element abundance gradients along the trailing arm. This may be a result of their small sample sizes and relatively large abundance ratio dispersion along the trailing arm (which was larger than their measurement uncertainties).

One advantage of the APOGEE database is that it enables the measurement of gradients along the stream homogeneously, accurately (with R $\sim$ 22,500 spectroscopy), and over a relatively continuous and even sampling of both the leading and trailing arms of the Sgr stream, primarily due to the serendipitous targeting of Sgr stream stars throughout the dual-hemisphere APOGEE survey. Thus, statistically significant abundance gradients along the Sgr stream can be measured for the first time.

In addition to measured metallicity differences between the Sgr dSph core and stream, we find differences in the α-element abundance ratios between the Sgr dSph and the streams, and between the trailing and leading arms. This is illustrated with the examples of Mg and Si (the α-elements measured most precisely by APOGEE, which are also reliably measured across the full parameter range of Sgr stars studied here; Jönsson et al. 2018) and the [Mg/Fe] and [Si/Fe] ratio distributions in the right panel of Figure 5.7. The median [Mg/Fe] ratios of the dSph core, trailing arm, and leading arm are $[\mathrm{Mg/Fe}]_{\mathrm{dSph}} = -0.03$, $[\mathrm{Mg/Fe}]_{\mathrm{trailing}} = -0.01$, and $[\mathrm{Mg/Fe}]_{\mathrm{leading}} = +0.03$, respectively and the median [Si/Fe] ratios of the dSph core, trailing arm, and leading arm are $[\mathrm{Si/Fe}]_{\mathrm{dSph}} = -0.12$, $[\mathrm{Si/Fe}]_{\mathrm{trailing}} = -0.07$, and $[\mathrm{Si/Fe}]_{\mathrm{leading}} = +0.03$, respectively.

Additionally we perform a KS tests on each pair of samples, and for Mg we find that there is a 36% probability that the [Mg/Fe] distribution of the trailing arm is drawn from the same distribution as the Sgr core, a 4% probability that the [Mg/Fe] distributions of the trailing and leading arm are dran from the same population, and finally a much lower probability ($\ll 1\%$) that the [Mg/Fe] distributions core and leading arm are drawn from the same parent population. In the case of Si, KS tests find a very low, $\ll 1\%$, probability that any of these three samples are drawn from each other's [Si/Fe] distributions, suggesting that these samples are more differentiated in their [Si/Fe] abundance ratios than in [Mg/Fe].

While the ~ 0.06 dex difference in [Mg/Fe] is smaller than the ~ 0.15 dex difference in [Si/Fe] between the Sgr dSph core and leading arm, these differences may suggest a gradient in the detailed chemical abundance patters along the Sgr stream. The [Mg/Fe] and [Si/Fe] of core and stream stars are shown in the middle and bottom panels of Figure 5.9 respectively, and we measure a gradient from the Sgr dSph core through each arm of the stream to find statistically significant gradients in Mg and Si abundances when anchoring the gradient to the Sgr dSph core, the magnitudes of which are reported along with their uncertainties in Table 5.2.

These gradients in α-element abundances appear to be associated with the anti-correlation between α-element abundance and metallicity along the α-shin of the α-Fe abundance pattern in the Sgr system (Hasselquist et al. 2017; Mucciarelli et al. 2017; Carlin et al. 2018; Hayes et al. in preparation). This anti-correlation is typical of the chemical abundance patterns of dwarf galaxies and chemical evolution models of such systems, and arises due to a change in the relative contribution of core collapse and Type Ia supernovae (SNe). Therefore, this observed α-element abundance gradient along the stream primarily reflects the overall metallicity gradient, but also demonstrates that the material in the streams is also less chemically evolved than the majority of the present-day Sgr dSph core.

As with the internal metallicity gradients within either arm of the stream, we typically find that the internal [Mg/Fe] and [Si/Fe] gradients in Table 5.2 are flatter or more uncertain, particularly within the trailing arm. However, unlike the internal metallicity gradients, we find that there is still evidence for an internal α-element abundance gradient along the leading arm in both Mg and Si. This suggests that, despite the shallow internal metallicity gradient along the leading arm, there appears to be some age or population gradient, perhaps even in a single Sgr stripping episode.

5.4.4 Gradients with Dynamical Age

While we can study the trailing and leading arms of the Sgr stream separately, in order to build a more complete picture of the Sgr stream we would ideally want to understand how the metallicity and chemistry of the Sgr stream changes with dynamical age (i.e., stripping). One way that we can combine the information learned from each of the arms to begin to study the full Sgr progenitor galaxy is by using the LM10 model in concert with our observations.

The LM10 model records when particles were stripped off of the Sgr galaxy and tracks this information to the present-day location of those particles. We can, therefore use the model particles at their present-day location in the sky to obtain a rough understanding of the dynamical age of observed Sgr stream stars in the same area of the sky, although we do note that this will, therefore, mean that the below results are model dependent on the LM10 model, and may vary if another model were used.

To do so, for each observed Sgr star, we find all of the model particles within 5°

of that star on the sky that have been stripped off within the past three pericenter passages (the portion of the model that is best matched to observations; LM10), i.e., $P_{col} \leq 3$ in the LM10 notation, and paint the median dynamical age of these model particles onto the observed Sgr stream stars. To match stars with nearby model particles, we only include those particles that cover parts of the stream for which we have observed stars. This is particularly important for regions of the sky where the arms of the Sgr stream overlap. For example, we do not include particles from the trailing arm that lie at $Y_s < 0$ kpc, since we do not have any stars in this part of the stream. Because they lie in the same part of the sky as the more densely populated leading arm, the former particles could erroneously push up the median dynamical age of particles in that region of the sky and bias our ages.

The estimated dynamical ages for our Sgr sample are shown in Figure 5.10 as a function of their solar Sgr longitude, superposed over the LM10 model from which these ages were drawn. This Figure highlights that our trailing arm sample is dynamically younger than our leading arm sample. Figure 5.10 also illustrates that, despite our trailing and leading arm samples each covering a large range of Sgr stream longitudes, the sample of stars within each arm were predominantly stripped off from the Sgr galaxy around the same time, and typically around the time of a Sgr pericenter passage. By considering either arm separately, we are not probing large ranges of the dynamical history of the Sgr stream, and, therefore any either particular arm biases our view of the chemical evolution history of Sgr itself.

Painting dynamical ages onto our observed sample of Sgr stream stars allows us to fold the information from each of the arms of the Sgr stream into one dimension and consider both arms together. While our total Sgr stream sample does still cluster around the dynamical ages of $\sim$ 800 Myr and $\sim$ 2.7 Gyr (corresponding to the

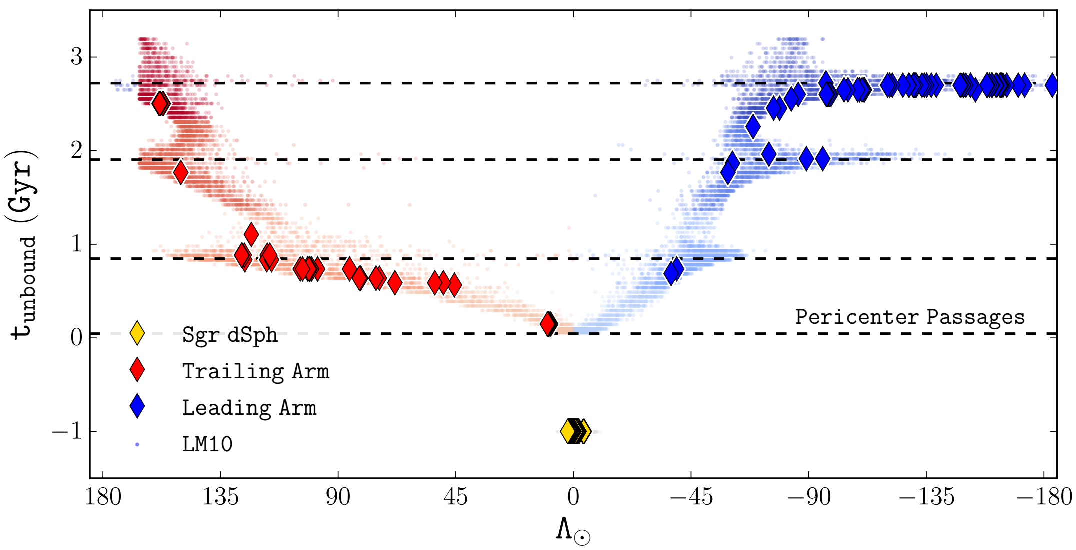

Fig. 5.10.— Dynamical age, $t_{\rm unbound}$, vs. solar Sgr longitude, $\Lambda_\odot$, for our Sgr sample colored as in Figure 5.9, and adopting the median dynamical age of Sgr stream particles from the LM10 model (small colored points) within 5° of each star (stars still bound to the Sgr dSph are assigned a dynamical age of −1 Gyr). The model particles are colored as in Figure 5.4, with a slight transparency to illustrate the more densely populated regions. Pericenter passages in the model are marked (black dashed lines) and highlight how much of the material in the Sgr stream is pulled off during these episodes and became spread over a large part of the sky.

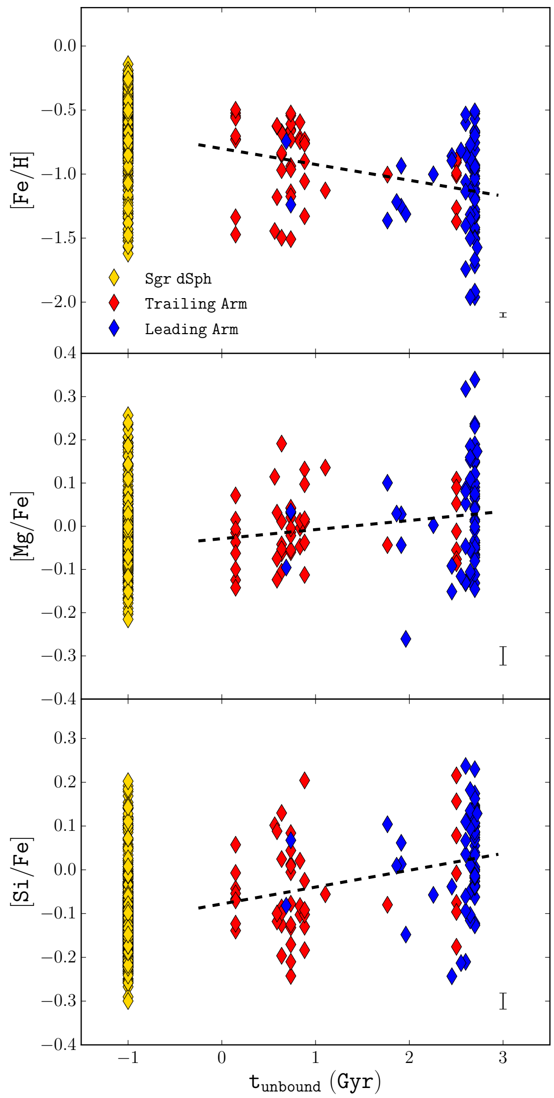

Fig. 5.11.— Metallicity, [Fe/H] (top), [Mg/Fe] (middle), and [Si/Fe] (bottom) of stars in the Sgr system observed by APOGEE vs. t_{unbound}, the estimated dynamical age each star as described in the text. The median uncertainty on each elemental abundance in our sample is shown as the errorbar in the bottom right-hand corner to illustrate the typical uncertainties. Stars from the Sgr dSph, trailing arm, and leading arm are colored as in Figure 5.9. Collapsing information from both arms into one dimension, we can see a coherent gradient in metallicity, [Mg/Fe], and [Si/Fe] with the expected dynamical age of stars in the Sgr stream, fit by a linear function (black dashed line).

pericenter passages on Sgr's last orbit and three times ago), we still build a more complete picture of the chemical history of Sgr than we would by focusing on the core or either particular arm alone. The metallicity, [Mg/Fe], and [Si/Fe] ratios of observed Sgr stars are shown as a function of their estimated dynamical age in Figure 5.11, and reveal coherent gradients of decreasing metallicity and increasing α-element abundance with increasing dynamical age as given in the final column of Table 5.2.

These gradients with dynamical age are still only a coarse proxy for gradients within the original Sgr galaxy, but do provide evidence that such gradients existed. The fact that there is also a gradient in α-element abundances using [Mg/Fe] and [Si/Fe] as an example in Figure 5.11, tells us that the material stripped earlier from the Sgr progenitor was also less chemically evolved, born from material that experienced fewer Type Ia SNe relative to core collapse SNe, and was therefore either formed earlier in Sgr's history or formed in regions with slower chemical enrichment. The slight differences between the Mg and Si gradients may then inform us about the detailed nucleosynthetic production of these elements, and how they differ over the star formation history of Sgr.

5.5 Discussion

In this work, we report not only the existence of chemical abundance differences between the Sgr core and the Sgr stream, but along the stream itself. These abundance variations imply a significant population gradient within the Sgr stream, with the lower metallicity and higher α-element abundance populations that were, on average, born from less enriched material than the dominant populations still found in the Sgr dSph core today.

As has been previously suggested (Chou et al. 2007; Keller et al. 2010; Law &

Majewski 2010; Carlin et al. 2012; Shi et al. 2012; Hyde et al. 2015), the abundance gradients along the stream are thought to be produced by the typically outside-in nature of tidal stripping acting on radial abundance gradients within the Sgr progenitor that are established through its secular chemical evolution. The particular chemical gradient imprinted on each arm is also dictated by the dynamics of tidal stripping and the differential angular spreading that occurs between the leading and trailing arms and at different phases along each arm itself. These dynamical variations complicate the direct comparison and interpretation of the two arms' chemical patterns.

In principle, a more holistic approach to assessing these gradients is possible by estimating the dynamical ages of individual stream stars using the LM10 model of the Sgr stream. With each stream star timestamped to a specific dynamical stripping age, we can more accurately combine the data from the two tidal arms to reveal and map the significant change in the chemistry of different populations that were pulled from the Sgr progenitor over time (Fig. 5.11). To the degree that tidal stripping preserves the relative radial distribution of stars in the Sgr progenitor, the abundance gradients we measure with dynamical age should correlate with the initial radial abundance gradients in the Sgr progenitor. Therefore, we should expect that the Sgr progenitor had an increasing fraction of more metal-poor and α-enhanced stars with increasing radius. This can give us an idea of the magnitude of the chemical differences that might have existed within the progenitor, but, unfortunately, to ultimately reconstruct the actual radial chemical profile of the Sgr progenitor requires knowledge of the original density (stellar *and* dark matter) profile of that system.

To simplify this problem, LM10 approached it from the other direction – i.e., by assuming a density profile for the progenitor, painting the constituent particles with abundances according to a prescription based on the energies of the particles, and then dynamically evolving the system to produce tidal stream abundance gradients. By varying the chemical abundance prescription with a fixed progenitor density profile (which could also be made a free parameter, but was not), the model stream gradients were constrained to match those observed, but were also traced back to report the requisite radial metallicity profile. More specifically, to approximately reproduce the metallicity distributions observed in the Sgr stream (Chou et al. 2007; Monaco et al. 2007), LM10 applied a metallicity distribution to the starting satellite configuration in their N-body simulation, which used a Plummer model (Plummer 1911), prescribing systematically lower metallicities to the higher energy particles, which would typically populate larger radii and be stripped earlier from the Sgr progenitor.

With this approach, LM10 found that to produce a 0.6 dex metallicity difference between the present-day Sgr stream and core in their model – i.e., similar to the largest differences we find between the core and tidal arms here – required an initial average metallicity variation of ~ 2.0 dex from the center to the edge of the Sgr progenitor. The inferred mean metallicity variation with radius within the original galaxy exceeds that observed along the stream because the tidal stripping of Sgr occurs primarily when the core is at pericenter. Due to the tidal impulse during pericenter passage, it is not just the outermost stars that are stripped away; instead, these episodes can dredge up stars from deeper in the galaxy's potential well, mixing stars from different orbital radii, blending populations, and producing a shallower gradient in the stream (LM10).

Thus, any observed mean metallicity and α-element abundance differences observed along the Sgr streams define the minimum radial variation that existed in the Sgr progenitor. According to the modeling by LM10, these variations may have been much larger, such that they far exceed those seen in any dwarf satellite of the MW today (e.g., the ~ 1 dex metallicity gradient in Sculptor; Tolstoy et al. 2004), making Sgr anomalous in this regard.

However, to place the original Sgr mean radial abundance variation properly in the context of those of other present-day dwarf galaxies, we may need to account for several potentially complicating factors, such as: (1) The progenitor Sgr system may have been different from other dSphs in the MW halo today in some way. (2) Other dwarf galaxies may also have had larger radial abundance variations in the past, but, like Sgr, these have also been reduced by tidal stripping, although perhaps to a lesser degree. (3) Current models of the Sgr tidal disruption (Law et al. 2005; Law & Majewski 2010; Łokas et al. 2010; Peñarrubia et al. 2010; Tepper-García, & Bland-Hawthorn 2018) are incomplete (e.g., they cannot yet account for the stream bifurcation), rudimentary (particularly concerning the details of the star formation and gaseous evolution of the Sgr core), and, in some regards, are even at odds with observations, such as improperly matching the northern portion of the trailing arm (Hernitschek et al. 2017; Sesar et al. 2017); thus, inferences drawn from such models must be considered tentative.

Regarding scenario (1), it is clear that the present Sgr system *looks* different than most other MW satellites in several ways. First, the present Sgr core is among the most massive dSphs, ranking second only to Fornax. But even Fornax only exhibits a ~ 0.7 dex drop in mean metallcity from center to edge (Battaglia et al. 2006; Leaman et al. 2013). However, also clearly setting Sgr apart is that it is the one classical (i.e., more massive) satellite that is obviously undergoing major tidal disruption, which is leading to a substantial loss of stars from the core. If one accounts for the lost stars *and* dark matter, the mass of the original Sgr may have far exceeded that of Fornax, perhaps placing the Sgr progenitor in the mass range between that of the SMC and

LMC (Chou et al. 2010; Mucciarelli et al. 2017; Gibbons et al. 2017; Carlin et al. 2018).

It has been suggested that the Sgr progenitor may have been a disk galaxy that is in the process of being "tidally stirred" into a highly stretched dSph morphology (Łokas et al. 2010; Peñarrubia et al. 2010), although the Sgr core does not exhibit evidence of significant rotation (Peñarrubia et al. 2011; Frinchaboy et al. 2012) that may be expected of such a system. Nonetheless, if Sgr was initially a disk galaxy, given estimates of its former mass, the Sgr progenitor may well have resembled the disky LMC, which could have further differentiated the Sgr progenitor from present-day classical dSphs.

On the other hand, even if the Sgr progenitor was a galaxy like the LMC before being tidally stripped and stirred, this may not yet explain the large inferred mean metallicity variation implied across Sgr by modeling. Even the LMC today does not seem to exhibit as large a radial mean metallicity drop, with only a ~ 0.5 dex difference from the LMC center to the $r \sim 10$ kpc extent that has been studied to date (Cioni 2009; Choudhury et al. 2016). Thus, even compared with the Magellanic satellites, the inferred 2.0 dex mean metallicity variation across the Sgr progenitor seems extreme.

Alternatively (scenario 2), perhaps the tidal processes affecting Sgr are not quite so unique. Like Sgr, the other dwarf satellites may have experienced tidal stripping that removed their least bound, most metal-poor populations, and produced the smaller metallicity variations seen in them today. Indeed, as an example of this phenomenon we can look at the present Sgr core itself, a system where we know that there has been significant stripping of metal-poor stars, and today exhibits only a $\sim$ 0.2-0.3 dex metallicity range with radius (Majewski et al. 2013; Mucciarelli et al. 2017) –

significantly smaller than the ~ 0.6 dex difference observed between the Sgr core and the dynamically old parts of the stream, and not even close to the 2 dex initial radial difference in the progenitor inferred from modeling (LM10).

While some of the most massive MW dSphs, such as Fornax and Sculptor, seem to have too large of orbits to be significantly affected by tidal stripping (Battaglia et al. 2015; Iorio et al. 2019), there is some support for the notion that other MW dSphs have been affected by tidal stripping (Majewski et al. 2002; Muñoz et al. 2006; Sohn et al. 2007; Battaglia et al. 2012; Roderick et al. 2015, 2016), and with that stripping preferentially removing older, more metal-poor populations to shape the overall present-day metallicity distribution functions (Majewski et al. 2002; Muñoz et al. 2006; Chou et al. 2007; Law & Majewski 2010; Sales et al. 2010; Battaglia et al. 2012). If this is true, then present-day dwarfs may have smaller radial metallicity variations than in the past, because they have also experienced some tidal evolution, albeit not as strongly as Sgr. Indeed, the relatively *small* metallicity variation in the Sgr core today may simply reflect that the Sgr orbit is smaller, yielding closer and more frequent pericenter passages that create stronger tidal evolution. In this scenario, Sgr may well have started out as a more typical dwarf galaxy prior to its currently strong tidal interaction with the MW.

As for scenario (3), we have already identified above several deficiencies in the current Sgr disruption models. More sophisticated and self-consistent models would better account for the observed gradients in the Sgr stream and enable a more appropriate comparison of the Sgr progenitor with other MW dwarf satellite galaxies. For example, as noted by LM10, one of the most obvious inconsistencies in their model (and other models of the Sgr stream; Peñarrubia et al. 2010; Tepper-García, & Bland-Hawthorn 2018), is that standard N-body models do not self-consistently account for the continuing star formation that the Sgr core experienced over the several billion years that the system tidally evolved within the MW's own changing external potential.

In the LM10 model, particles are assigned ages and metallicities *ab initio*, including star particles that should be born after the beginning of the simulation. While no particles are stripped before they would nominally be born, there are particles that are assigned ages that would require them to be born during the tidal stripping of Sgr. Not only will the gas in the Sgr progenitor evolve differently than stars (Tepper-García, & Bland-Hawthorn 2018) as Sgr orbits the MW, but the populations born during the tidal stripping of Sgr are some of the most bound, metal-rich particles populating the inner radii of the initial model. Therefore, these young stars (model particles) raise the initial metallicity of the Sgr progenitor core and contribute to a steepening of the metallicity gradient in the initial Sgr model when, in reality, stars of those metallicities would not have been born until several billion years after the tidal stripping of Sgr began.

A more sophisticated and self-consistent modeling of Sgr as an evolving system of stars *and* gas would lend considerable insights into the interaction between the star formation, chemical, and dynamical evolution of the system as a whole. For example, it is known that the Sgr core has experienced a relatively bursty star formation history (Siegel et al. 2007), but it is not clear how much of this was induced or modulated by Sgr's interaction with the MW (e.g., compressional shocking of gas at pericenter sparking star formation or the complex effects of ram pressure stripping that facilitate some gas loss, but can compress the remaining gas to produce more star formation), and whether this bursty star formation only occurred in the central-most regions of the Sgr core, or if this bursty star formation was more widespread. Star formation induced by interaction with the MW that rapidly accelerated the enrichment of the Sgr core could have produced the young, metal-rich populations seen in the Sgr dSph core today, but not contributed to the populations seen in the Sgr stream, which were relatively "frozen" for the past several billion years.

As mentioned above, more than one of these various complicating factors may have contributed to explaining the larger inferred radial abundance variation in the Sgr progenitor compared to those observed in more standard dSph satellites of the MW.

5.6 Conclusion

We present an abundance analysis of the Sgr system using data from the largest sample of Sgr stream stars having high-resolution spectra to date. This stream sample, mostly obtained serendipitously in the course of the APOGEE survey, totals 166 stream members, 63 of which are in the trailing arm and 103 in the leading arm. We identified these stars as belonging to the Sgr stream by their kinematics, derived via a combination of *Gaia* DR2 proper motions, `StarHorse` spectrophotometric distances (Santiago et al. 2016; Queiroz et al. 2018), and APOGEE radial velocities.

In particular, we have selected these stream members based on the consistency of their angular momentum with the Sgr core and their kinematical alignment with respect to the Sgr orbital plane. This kinematical selection quite cleanly identifies Sgr stream members free of most other MW contamination. We use this sample of Sgr stream stars, together with the 325 Sgr dSph core members from Hasselquist et al. (2017) plus 385 additional core members identified here to measure the metallicity and α-element abundance differences between and variations along the Sgr stream and core system.

We find a considerable metallicity difference of Δ[Fe/H] ~ 0.6 dex and α-element abundance differences of Δ[Mg/Fe] ~ 0.06 dex and Δ[Si/Fe] ~ 0.15 dex between the Sgr dSph core and the dynamically older, leading arm Sgr stream subsample. Our trailing arm subsample, which is dynamically younger, falls in between the core and leading arm in both metallicity and α-element abundances. These differences indicate that there are metallicity and α-element gradients from the Sgr core through each arm of the Sgr stream. However, we typically find much flatter gradients – consistent with zero – when we measure gradients internally, along each of the sampled parts of each tidal arm separately (not including the higher metallicity Sgr dSph core), except for some evidence that there is still a significant α-element gradient internally along the leading arm.

Past modeling has shown that most of the tidal stripping of Sgr occurs in episodes during pericenter passages, and consulting such models, we find that our leading and trailing arm samples each primarily trace material stripped during different pericenter passages, but likely do not individually contain many stars that come from multiple stripping episodes. Therefore neither arm sample explored here *would be expected* to exhibit strong internal gradients with Sgr longitude.

By prescribing dynamical (i.e., stripping) ages from the LM10 model onto our stream sample, we can combine our samples from both arms into a more integrated view, which demonstrates that there are metallicity and α-element abundance gradients as a function of dynamical age *across* the stream as a whole. This provides better evidence that there were radial abundance gradients within the Sgr progenitor, because it is expected that the dynamical age of stars map more directly onto their initial orbital radius or total energy within the former Sgr galaxy.

Previous modeling of the tidal evolution of Sgr has found that episodic tidal impulses during pericenter passages will dredge up and mix multiple stellar populations from different radii as they are stripped away, reducing the abundance variations seen when stars are pulled into the tidal stream (LM10). Conversely, any abundance variations seen in the tidal stream today should betray stronger radial variations in the initial system.

Modeling suggests that the initial radial metallicity variations in the Sgr progenitor might have been very large indeed (as much as 2 dex in overall metallicity; LM10), far exceeding those observed in any present-day MW satellites. However, we argue that such a large inferred abundance variation compared to other present-day dSphs might be partially explained if the Sgr progenitor had been structurally different than the other systems, e.g., more massive or perhaps morphologically different (e.g., a dwarf spiral, like the LMC). Moreover, the abundance variations in other dwarfs may have also been reduced (though to a lesser extent) by tidal stripping.

Further interpretation of the gradients now confirmed to exist along the Sgr stream, would, however, benefit from more sophisticated modeling of the Sgr system, to determine how steep the initial abundance gradients within the Sgr progenitor must have been. The greatest improvement in current models would be self-consistent treatment of star formation and chemical enrichment as Sgr evolves under the tidal influence of the MW. This modeling could reveal how much the core of Sgr has evolved since it fell into the MW's potential, and how much mixing occurred during it's episodic stripping.

The presence of primarily more metal-poor Sgr stars in the Sgr stream demonstrates how studies of the present Sgr core will yield skewed metallicity and α-element distribution functions compared to those that were actually produced over time in the original Sgr system. Only by combining the growing data set of high-resolution spectroscopy of Sgr stream stars with samples of the Sgr dSph core that are consistently analyzed can we accurately reconstruct the chemical abundance profile of the Sgr progenitor. We will present such an analysis in Hayes et al. (in preparation), using multiple elements produced via different nucleosynthetic pathways, to better understand the chemical evolution of the Sgr system.

Chapter 6

Summary

In this dissertation we have used state-of-the-art Galactic surveys to probe the accretion history of the Milky Way (MW), explore the active accretion of the Sgr dSph through its tidal stream, and observe the effects of dwarf galaxies gravitationally torquing the MW disk by identifying the TriAnd overdensity as a feature of the MW disk. These findings are among many other developments in the literature, which, together, have improved our understanding of the MW's halo and outer disk, and now have brought us to new questions that we as a discipline are trying to answer. These include the following topics extending from the research described in this dissertation.

6.1 Gaia-Enceladus-Sausage: The Milky Way's Massive Accretion Event

In Chapter 2 we found that the MW halo is bifurcated in its [Mg/Fe] abundances, and that this chemical bifurcation is also present in several other chemical planes, indicating that the MW halo is dominated by two distinct populations. One of these is an *in situ* population that seems to be a kinematically hotter and more metal-poor extension of the thick disk, whereas the other population, composing a significant fraction of the halo (particularly at metallicities, [Fe/H] $\gtrsim -1.5$), was accreted from one or a few relatively massive dwarf galaxies.

With the release of *Gaia* DR2 (Gaia Collaboration et al. 2018a), the study of this accreted population has grown rapidly, due to the abundance of information available for halo stars through the combination of data from photometric, astrometric, and spectroscopic surveys. It has been argued that a large fraction of the accreted population may have come predominantly from a single accretion event, referred to as the Gaia-Sausage (Belokurov et al. 2018) or Gaia-Enceladus (Helmi et al. 2018), which may or may not also be related with the retrograde Sequoia accretion event (Myeong et al. 2019) that has also been identified kinematically. The key result that seems to unambiguously associate most of this accreted population to a single event has been the finding that the stars with accreted chemistry mostly exhibit highly eccentric orbits, found either indirectly from their kinematics, or directly from orbital integration. The predominance of stars with such radial orbits imply that they were accreted from a dwarf galaxy, the "Gaia-Enceladus-Sausage" (GES) progenitor, that upon infall into the MW was, itself, on a highly eccentric orbit ($e \sim 0.85$) (Belokurov et al. 2018; Helmi et al. 2018; Myeong et al. 2018; Fattahi et al. 2019; Mackereth et al. 2019a).

When age dating the stars in the GES debris, either spectroscopically, photometrically, or through chemical evolution modeling (Schuster et al. 2012; Haywood et al. 2018; Gallart et al. 2019; Vincenzo et al. 2019), studies find that the typical age of GES stars is around 12 Gyr, but a comparison of this system with cosmological simulations indicates that high-eccentricity accretion events typically happen later in a galaxy's life, a result that supports that GES may have been accreted more recently, around 8-10 Gyr ago (Mackereth et al. 2019a), i.e., several Gyr after it had formed the bulk of its stars. These comparisons with cosmological simulations and chemical evolution modeling are also consistent with the assertion made in Chapter 2, i.e., that the MW's accreted population came predominantly from one or more relatively massive dwarf galaxies, because they find that the GES system should have had a stellar mass of around $10^{8.5} - 10^{9}$ $M_{\odot}$ (Mackereth et al. 2019a; Vincenzo et al. 2019), which lies in between the masses of the SMC and LMC (Besla et al. 2012).

Given the relative coincidence of the accretion time reported for GES with age of the MW thick disk, and the fact that the GES dwarf seems to have been a relatively massive dwarf galaxy, several studies of the GES system have speculated that its accretion could have instigated a break in star formation in the thick disk, allowing for gas settling into the thin disk we see today before forming stars again, and possibly even contributed some pristine gas in the process (Belokurov et al. 2018; Haywood et al. 2018; Helmi et al. 2018; Myeong et al. 2018; Fattahi et al. 2019; Mackereth et al. 2019a,b; Vincenzo et al. 2019). The recent discovery of the GES and Sequoia systems means that our understanding of these events is just beginning, and will likely develop greatly in the coming years as more sophisticated analysis techniques are used to assess these systems.

6.2 Ripples in the Milky Way Disk

In Chapter 3 we show that the outer disk overdensity TriAnd has the chemistry that would be predicted when the chemical gradients of the disk are extrapolated out to the Galactocentric radius of TriAnd. This similarity to the MW disk and chemical distinction from dwarf galaxy chemical abundance patterns indicates that TriAnd is indeed a feature of the MW disk. This in turn implies that the MW disk is $\gtrsim 25$ kpc *in radius*, almost twice the canonical radius of 15 kpc typically quoted, and that the disk is significantly perturbed, with material extending as far as 5-10 kpc away from the nominal disk midplane.

Other studies, concurrent with the work here, have concluded that TriAnd, along with two other outer disk overdensities, A13 and the Monoceros Ring, are all related features of the MW's disk instead of distinct tidal streams as originally postulated (Bergemann et al. 2018; Sheffield et al. 2018; Sales Silva et al. 2019). These overdensities appear to alternate above and below the MW disk with increasingly larger Galactocentric radii, offering a tantalizing picture that the MW disk has ripples or corrugations, and that these overdensities are simply the peaks or troughs of these oscillations where stars pile up along our line of sight through the Galactic Anticenter (Price-Whelan et al. 2015; Xu et al. 2015; Li et al. 2017; Sheffield et al. 2018). This notion is supported by recent N-body simulations showing that perturbations in the outer disk could have been produced by the gravitational torquing from Sgr in its near polar orbit about the MW (Laporte et al. 2018).

Perturbations to the MW disk have also been seen more locally in the phase space distribution of stars around the sun, now that *Gaia* DR2 provides the ability to measure these precisely. In particularl, studies have found that MW disk stars follow a "zV_z phase spiral" (Antoja et al. 2018; Bland-Hawthorn et al. 2019) and show wave-like patterns in their $V_r - L_z$ distribution (Friske & Schönrich 2019), which simulations and models indicate could also be produced by Sgr's dynamical effects on the MW disk (Carrillo et al. 2019; Laporte et al. 2019). These all point to evidence that Sgr's orbit has produced complex, interfering density waves in the MW, perturbing both the inner regions, where densities are high, so the perturbations show up in the velocity and phase space distribution of stars, as well as the outer regions of the disk, where densities are low enough that Sgr's dynamical influence may be strong enough to actually perturb the density distribution of the disk and alter its shape.

6.3 Probing the Milky Way with Stellar Streams

Focusing on the most vivid known example of active MW accretion, we have examined the Sgr dSph system and its tidal stream in a few different ways. In Chapter 4, we found and traced the Sgr stream via its proper motions in *Gaia* DR2. This allowed us to identify Sgr stream members with a low degree of contamination, and measure the proper motion of the Sgr stream as a whole. Because of the advantageous orientation of the Sgr stream on the sky, this observed motion contains the imprint of the solar reflex motion, and by comparing this motion to N-body simulations of the Sgr system, we extracted the Sun's rotational velocity around the MW. We measure this to be $\Theta_\odot = 253 \pm 6$ km s^{-1}, the most precise measure of the Sun's motion that is independent of its assumed Galactocentric radius, but which is also consistent with the $\Theta_\odot = 245.6 \pm 1.4$ km s^{-1} calculated from the combination of the precise R_0 measured by Gravity Collaboration et al. (2018) and the reflex motion of the Sun measured from the proper motion of Sgr A* (Reid & Brunthaler 2004). This agreement is expected, but nonetheless reassuring that these independent measurements are giving us consistent results.

This detection of the Sgr stream is one of several recent examples that illustrates that *Gaia*'s precise astrometry can distinguish dwarf galaxies, globular clusters, and their tidal streams from halo contamination quite clearly (e.g., Price-Whelan & Bonaca 2018; Price-Whelan et al. 2019; Bonaca et al. 2019; Ibata et al. 2019a,b; Koposov et al. 2019; Malhan et al. 2019). By characterizing the motion of these halo objects, we can then probe the mass distribution of the MW (here we have essentially inferred the depth of the MW's potential by measuring the solar reflex motion as seen in the Sgr stream). Extending this method to more systems provides a promising method to understand the 3-D dark matter distribution in the MW halo (Malhan & Ibata 2019) in the future.

6.4 High Precision Characterization of the Sagittarius Stream

Finally, in Chapter 5 we combined the power of APOGEE and *Gaia* DR2 to further study the Sgr stream and better understand its own star formation and chemical enrichment history. Our finding of metallicity and α-element abundance gradients along the Sgr stream indicates that the Sgr progenitor had considerable *radial* chemical and population gradients before it fell into the MW and began its tidal disruption. Additionally, our findings imply that the core of Sgr has undergone subsequent star formation and chemical enrichment since its tidal stripping began.

Now that surveys such as APOGEE (Majewski et al. 2017), Gaia (Gaia Collaboration et al. 2016), and LAMOST (Zhao et al. 2012) are observing fainter stars over large areas of the sky, it is now feasible to begin identifying considerable samples of Sgr core and stream stars throughout the MW halo. Observations of the Sgr core are now precisely measuring its proper motion (Gaia Collaboration et al. 2018b), and providing the most detailed picture of its chemical abundance profile (Hasselquist et al. 2017; Mucciarelli et al. 2017). These chemical studies show that Sgr may have been a fairly massive dwarf galaxy, and find that Sgr is deficient in almost all elements relative to Fe at [Fe/H] ~ -0.8, which could be explained if Sgr formed stars with a top-light initial mass function (IMF; Hasselquist et al. 2017; Mucciarelli et al. 2017).

The study of the Sgr stream has benefited even more than the Sgr core from the presence of these large sky surveys, which greatly improve the prospects for detecting and identifying Sgr stream stars via overdensities (Hernitschek et al. 2017; Sesar et al. 2017), kinematics (Carlin et al. 2018; Yang et al. 2019; Antoja et al. 2020), and chemical tagging (Hasselquist et al. 2019). Such efforts have revealed that the previously untraced, dynamically old portion of the Sgr trailing arm extends higher above the MW disk than models constrained by closer debris suggested (e.g. Law & Majewski 2010), and instead it crosses or intersects the apex of leading arm (Hernitschek et al. 2017; Sesar et al. 2017; Yang et al. 2019).

The chemical abundances of these newly identified Sgr stream stars also support the conclusions from Hasselquist et al. (2017)'s chemical evolution modeling of the Sgr core, that a top-light IMF may be needed to describe Sgr's chemical abundance profile (Carlin et al. 2018). However, as argued in Chapter 5, these chemical studies are biased toward higher metallcities, and, therefore require lower metallicity Sgr members to confirm the need for a top-light IMF. Nonetheless, despite being biased toward higher metallicities, the chemistry of these Sgr stream stars is consistent our findings in Chapter 5 that the Sgr stream is more metal-poor and α-enhanced than the Sgr core (Carlin et al. 2018; Hasselquist et al. 2019).

With the many increasingly recent large studies of the Sgr core and stream we are better characterizing the chemistry and kinematics of Sgr system and reconstructing the nature of the Sgr progenitor. This wealth of available information has outpaced the modeling of the Sgr system, which is now too incomplete, rudimentary, or at odds with the latest observations in various ways, and so motivating the need for more sophisticated simulations of the Sgr system, so that we can understand its history before and throughout its accretion.

6.5 Looking Ahead

The progress made in this dissertation and other recent studies have greatly developed our understanding of the accretion history of the MW and the current status of accretion in the MW today. However, answering questions such as those posed in Chapter 1, or even beginning to answer them, has only raised new questions about the hierarchical formation of the MW. Some of the biggest outstanding questions now, raised by the work here or elsewhere, are the following:

- Are the Gaia-Enceladus-Sausage and Sequoia accretion events related, possibly representing two stages of the same event, or were they distinct systems?
- Aside from the Gaia-Enceladus-Sausage and Sequoia systems, were there other significant accretion events in the MW's past that has helped populate it's halo?
- Did Gaia-Enceladus-Sausage provide a "second infall" of gas that has been previously theorized as the event that instigated the formation of the thin disk/low-α sequence, and that separates it from the thick disk/high-α sequence in chemical space (i.e., Chiappini et al. 1997; Grisoni et al. 2017; Spitoni et al. 2019; Vincenzo et al. 2019, and references therein)?
- Does the MW have any classical halo (e.g., coming from an initial monolithic collapse), or does it only have an accreted halo, and its *in situ* "halo" population is merely the thick disk, which gets kinematically hotter at lower metallcities?
- Are the perturbations in the MW disk (seen locally as phase space density patterns, and as ripples in the outer disk) primarily due the gravitational influence

of Sgr as it orbits the MW, or are other systems needed to explain these features? How much of an effect do the Magellanic Clouds, which appear to be on their first infall into the MW (Kallivayalil et al. 2013), have on the disk?

- How long has Sgr been tidally disrupting and what is the extent of its tidal arms? Does the leading arm extend below the MW disk near the sun, or does it terminate around the point that it passes through the disk?

- How massive was the Sgr progenitor?

- How strong were Sgr's initial radial metallicity and α-element abundance gradients?

- What role has Sgr's proximity to the MW played in its chemical evolution, and more broadly how does a dwarf galaxy's environment effect its chemical evolution (e.g., how has the Magellanic Clouds' relative isolation differentiated them from chemical evolution of Sgr or the Gaia-Enceladus-Sausage system)?

- It now appears that the Magellanic Clouds may have fallen into the MW halo with their own system of satellites (Kallivayalil et al. 2018), but does this include some of the relatively massive classical dwarf galaxies, such as Carina and Fornax, which might be expected from ΛCDM cosmological simulations (Pardy et al. 2020) and has been long postulated by the apparent alignement of these galaxies (e.g., Kunkel & Demers 1976; Kunkel 1979; Lynden-Bell 1982; Majewski 1993a, 1994a)?

As illustrated throughout this dissertation, surveys are powerful tools that can probe the accretion of dwarf galaxies in the MW and reconstruct its accretion history. With the next generation of survey telescopes, this process will only accelerate, because these telescopes will be able to push limiting magnitudes a few magnitudes fainter, and can scan the sky up to $3-10\times$ faster than the most efficient surveys operating today (surveys like Pan-STARRS, the Panoramic Survey Telescope and Rapid Response System, APOGEE, GALAH, or LAMOST), all to ultimately observe over $10\times$ more stars than the current generation of surveys. Such feats are made possible by mating large diameter telescopes ($4-11$ meter primaries) with large field of view detectors (up to ~ 10 deg^2), as at the Vera Rubin Observatory (formerly known as the Large Synoptic Survey Telescope, LSST; Ivezić et al. 2019), and/or highly multiplexed, fiber-fed spectrographs (with $\sim 1000-4000$ fibers) for the next generation of spectroscopic survey telescopes, e.g., the William Herschel Telescope (WHT) Enhanced Area Velocity Explorer (WEAVE), the 4-metre Multi-Object Spectroscopic Telescope (4MOST; de Jong et al. 2019), and the Maunakea Spectroscopic Explorer (MSE; Bergemann et al. 2019).

These future surveys promise a bright and productive future for the field of Galactic astronomy and for our ever-improving understanding of the MW, its halo, and its accretion history, which provide a vital, detailed template of how galaxies can grow through evolve via low-mass ratio mergers.

References

Abolfathi, B., Aguado, D. S., Aguilar, G., et al. 2018, ApJS, 235, 42

Aguado, D. S., Ahumada, R., Almeida, A., et al. 2018, ApJS, 240, 23

Adibekyan, V. Z., Figueira, P., Santos, N. C., et al. 2013, A&A, 554, A44

Ahumada et al., 2020, submitted

Alam, S., Albareti, F. D., Allende Prieto, C., et al. 2015, ApJS, 219, 12

Albareti, F. D., Allende Prieto, C., Almeida, A., et al. 2017, ApJS, 233, 25

Allen, C., Poveda, A., & Schuster, W. J. 1991, A&A, 244, 280

Allende Prieto, C., Kawata, D., & Cropper, M. 2016, A&A, 596, A98

Anders, F., Chiappini, C., Santiago, B. X., et al. 2014, A&A, 564, A115

Anders, F., Khalatyan, A., Chiappini, C., et al. 2019, A&A, 628, A94

Andrews, B. H., Weinberg, D. H., Schönrich, R., et al. 2017, ApJ, 835, 224

Antoja, T., Helmi, A., Romero-Gómez, M., et al. 2018, Nature, 561, 360

Antoja, T., Ramos, P., Mateu, C., et al. 2020, arXiv e-prints, arXiv:2001.10012

Arnould, M., Goriely, S., & Jorissen, A. 1999, A&A, 347, 572

Bailer-Jones, C. A. L., Rybizki, J., Fouesneau, M., Mantelet, G., & Andrae, R. 2018, AJ, 156, 58

Battaglia, G., Irwin, M., Tolstoy, E., et al. 2012, ApJ, 761, L31

Battaglia, G., Sollima, A., & Nipoti, C. 2015, MNRAS, 454, 2401

Battaglia, G., Tolstoy, E., Helmi, A., et al. 2006, A&A, 459, 423

Beaton, R. L., et al., in preparation

Beers, T. C., Drilling, J. S., Rossi, S., et al. 2002, AJ, 124, 931

Beers, T. C. & Christlieb, N. 2005, ARA&A, 43, 531

Beers, T. C., Carollo, D., Ivezić, Ž., et al. 2012, ApJ, 746, 34

Bellazzini, M., Ferraro, F. R., & Ibata, R. 2003, AJ, 125, 188

Bellazzini, M., Newberg, H. J., Correnti, M., Ferraro, F. R., & Monaco, L. 2006, A&A, 457, L21

Belokurov, V., Evans, N. W., Irwin, M. J., et al. 2006, ApJ, 637, L29

Belokurov, V., Koposov, S. E., Evans, N. W., et al. 2014, MNRAS, 437, 116

Belokurov, V., Erkal, D., Evans, N. W., et al. 2018, MNRAS, 478, 611

Bensby, T., Feltzing, S., Lundström, I., et al. 2005, A&A, 433, 185

Bensby, T., Feltzing, S., & Oey, M. S. 2014, A&A, 562, 71

Bergemann, M., Sesar, B., Cohen, J. G., et al. 2018, Nature, 555, 334

Bergemann, M., Huber, D., Adibekyan, V., et al. 2019, arXiv e-prints, arXiv:1903.03157

Besla, G., Kallivayalil, N., Hernquist, L., et al. 2012, MNRAS, 421, 2109

Bland-Hawthorn, J., Sharma, S., Tepper-Garcia, T., et al. 2019, MNRAS, 486, 1167

Blanton, M. R., Bershady, M. A., Abolfathi, B., et al. 2017, AJ, 154, 28

Bonaca, A., Conroy, C., Price-Whelan, A. M., et al. 2019, ApJ, 881, L37

Bovy, J., Hogg, D. W., & Rix, H.-W. 2009, ApJ, 704, 1704

Bovy, J., Allende Prieto, C., Beers, T. C., et al. 2012, ApJ, 759, 131

Bovy, J., Rix, H.-W., Schlafly, E. F., et al. 2016, ApJ, 823, 30

Bowen, I. S., & Vaughan, A. H., Jr. 1973, Appl. Opt., 12, 1430

Bressan, A., Marigo, P., Girardi, L., et al. 2012, MNRAS, 427, 127

Bullock, J. S., & Johnston, K. V. 2005, ApJ, 635, 931

Carballo-Bello, J. A., Corral-Santana, J. M., Martínez-Delgado, D., et al. 2017, MNRAS, 467, L91.

Carlin, J. L., Majewski, S. R., Casetti-Dinescu, D. I., et al. 2012, ApJ, 744, 25

Carlin, J. L., Sheffield, A. A., Cunha, K., et al. 2018, ApJ, 859, L10.

Carollo, D., Beers, T. C., Lee, Y. S., et al. 2007, Nature, 450, 1020

Carollo, D., Beers, T. C., Chiba, T. C., et al. 2010, ApJ, 712, 692

Carretta, E., Bragaglia, A., Gratton, R. G., et al. 2010, A&A, 520, A95

Carrillo, I., Minchev, I., Steinmetz, M., et al. 2019, MNRAS, 490, 797

Cassisi, S., & Salaris, M. 2013, Old Stellar Populations: how to study the fossil record of galaxy formation (Wiley-VCH)

Chiappini, C., Matteucci, F., & Gratton, R. 1997, ApJ, 477, 765

Chiba, M. & Beers, T. C. 2000, AJ, 119, 2843

Chou, M.-Y., Majewski, S. R., Cunha, K., et al. 2007, ApJ, 670, 346

Chou, M.-Y., Cunha, K., Majewski, S. R., et al. 2010, ApJ, 708, 1290

Chou, M.-Y., Majewski, S. R., Cunha, K., et al. 2011, ApJ, 731, L30

Choudhury, S., Subramaniam, A., & Cole, A. A. 2016, MNRAS, 455, 1855.

Cioni, M.-R. L. 2009, A&A, 506, 1137.

Cox, A. N. 2000, Allen's Astrophysical Quantities,

Crane, J. D., Majewski, S. R., Rocha-Pinto, H. J., et al. 2003, ApJ, 594, L119

Da Costa, G. S., & Armandroff, T. E. 1995, AJ, 109, 2533

de Jong, R. S., Agertz, O., Berbel, A. A., et al. 2019, The Messenger, 175, 3

De Silva, G. M., Freeman, K. C., Bland-Hawthorn, J., et al. 2015, MNRAS, 449, 2604

Deason, A. J., Belokurov, V., Hamren, K. M., et al. 2014, MNRAS, 444, 3975

Deg, N., & Widrow, L. 2013, MNRAS, 428, 912

Dinescu, D. I., Majewski, S. R., Girard, T. M., & Cudworth, K. M. 2000, AJ, 120, 1892

Dinescu, D. I., Majewski, S. R., Girard, T. M., et al. 2002, ApJ, 575, L67

Eggen, O. J., Lynden-Bell, D., & Sandage, A. R. 1962, ApJ, 136, 748

Eisenstein, D. J., Weinberg, D. H., Agol, E., et al. 2011, AJ, 142, 72

Ester, M., Kriegal, H. P., & Sander, J. 1996, in Proc. 2nd Int. Conf. on Knowledge Discovery and Data Mining (KDD96) (Menlo Park, CA: AAAI Press), 226

Fattahi, A., Belokurov, V., Deason, A. J., et al. 2019, MNRAS, 484, 4471

Fermani, F., & Schönrich, R. 2013, MNRAS, 432, 2402

Fernández-Alvar, E., Carigi, L., Allende Prieto, C., et al. 2017, MNRAS, 465, 1586

Fernández-Alvar, E., Carigi, L., Schuster, W. J., et al. 2018, ApJ, 852, 50

Fishlock, C. K., Yong, D., Karakas, A. I., et al. 2017, MNRAS, 466, 4672

Frebel, A., & Norris, J. E. 2015, ARA&A, 53, 631

Frinchaboy, P. M., Majewski, S. R., Muñoz, R. R., et al. 2012, ApJ, 756, 74

Friske, J. K. S., & Schönrich, R. 2019, MNRAS, 490, 5414

Fritz, T. K., Battaglia, G., Pawlowski, M. S., et al. 2018, A&A, 619, A103

Font, A. S., Johnston, K. V., Bullock, J. S., & Robertson, B. E. 2006, ApJ, 638, 585

García Pérez, A. E., Allende Prieto, C., Holtzman, J. A., et al. 2016, AJ, 151, 144

Geisler, D., Smith, V. V., Wallerstein, G., Gonzalez, G., Charbonnel, C. 2005, AJ, 129, 1428

Gaia Collaboration, Prusti, T., de Bruijne, J. H. J., et al. 2016, A&A, 595, A1

Gaia Collaboration, Brown, A. G. A., Vallenari, A., et al. 2018, A&A, 616, A1

Gaia Collaboration, Helmi, A., van Leeuwen, F., et al. 2018, A&A, 616, A12

Gallart, C., Bernard, E. J., Brook, C. B., et al. 2019, Nature Astronomy, 3, 932

García Pérez, A. E., Allende Prieto, C., Holtzman, J. A., et al. 2016, AJ, 151, 144

Gibbons, S. L. J., Belokurov, V., & Evans, N. W. 2017, MNRAS, 464, 794.

Gilmore, G. & Reid, N. 1983, MNRAS, 202, 1025

Gilmore, G., Wyse, R. F. G., & Kuijken, K. 1989, ARA&A, 27, 555

Gilmore, G., Wyse, R. F. G., & Norris, J. E. 2002, ApJ, 574, L39

Gilmore, G., Randich, S., Asplund, M., et al. 2012, The Messenger, 147, 25

Gómez, F. A., Minchev, I., O'Shea, B. W., et al. 2013, MNRAS, 429, 159

Gómez, F. A., White, S. D. M., Marinacci, F., et al. 2016, MNRAS, 456, 2779

Gratton, R. G., Sneden, C., Carretta, E., & Bragaglia, A. 2000, A&A, 354, 169

Gratton, R., Sneden, C., & Carretta, E. 2004, ARA&A, 42, 385

Gratton, R. G., Carretta, E., Bragaglia, A., Lucatello, S., & D'Orazi, V. 2010, A&A, 517, A81

Graur, O., Poznanski, D., Maoz, D., et al. 2011, MNRAS, 417, 916

Gravity Collaboration, Abuter, R., Amorim, A., et al. 2018, A&A, 615, L15

Grillmair, C. J. 2006, ApJ, 645, L37

Grillmair, C. J. 2006, ApJ, 651, L29

Grillmair, C. J., & Dionatos, O. 2006, ApJ, 643, L17

Grillmair, C. J. 2009, ApJ, 693, 1118

Grillmair, C. J., & Carlin, J. L. 2016, Tidal Streams in the Local Group and Beyond, 87

Grisoni, V., Spitoni, E., Matteucci, F., et al. 2017, MNRAS, 472, 3637

Grisoni, V., Spitoni, E., & Matteucci, F. 2018, MNRAS, 481, 2570

Gunn, J. E., Siegmund, W. A., Mannery, E. J., et al. 2006, AJ, 131, 2332

Gustafsson, B., Edvardsson, B., Eriksson, K., et al. 2008, A&A, 486, 951

Hartwick, F. D. A. 1987, NATO Advanced Science Institutes (ASI) Series C, 207, 281

Hasselquist, S., Shetrone, M., Smith, V., et al. 2017, ApJ, 845, 162

Hasselquist, S., Carlin, J. L., Holtzman, J. A., et al. 2019, ApJ, 872, 58

Hawkins, K., Jofré, P., Masseron, T., & Gilmore, G. 2015, MNRAS, 453, 758

Hawkins, K., Masseron, T., Jofré, P., et al. 2016, A&A, 594, A43

Hayden, M. R., Bovy, J., Holtzman, J. A., et al. 2015, ApJ, 808, 132

Hayes, C. R., Majewski, S. R., Shetrone, M., et al. 2018, ApJ, 852, 49

Hayes, C. R., Majewski, S. R., Hasselquist, S., et al. 2018, ApJ, 859, 8

Hayes, C. R., Law, D. R., & Majewski, S. R. 2018, ApJ, 867, L20

Hayes, C. R., Majewski, S. R., Hasselquist, S., et al. 2020, ApJ, 889, 63

Hayes, C. R., et al., in preparation

Haywood, M., Di Matteo, P., Lehnert, M. D., et al. 2018, ApJ, 863, 113

Helmi, A. 2004, ApJ, 610, L97

Helmi, A., Babusiaux, C., Koppelman, H. H., et al. 2018, Nature, 563, 85

Heringer, E., Pritchet, C., & van Kerkwijk, M. H. 2019, ApJ, 882, 52

Hernitschek, N., Sesar, B., Rix, H.-W., et al. 2017, ApJ, 850, 96

Hernitschek, N., Cohen, J. G., Rix, H.-W., et al. 2019, ApJ, 871, 49.

Hogg, D. W., Eilers, A.-C., & Rix, H.-W. 2019, AJ, 158, 147

Holtzman, J. A., Hasselquist, S., Shetrone, M., et al. 2018, AJ, 156, 125

Holtzman, J. A., Shetrone, M., Johnson, J. A., et al. 2015, AJ, 150, 148

Howell, D. A. 2011, Nature Communications, 2, 350

Hyde, E. A., Keller, S., Zucker, D. B., et al. 2015, ApJ, 805, 189

Ibata, R. A., Gilmore, G., & Irwin, M. J. 1994, Nature, 370, 194

Ibata, R. A., Gilmore, G., & Irwin, M. J. 1995, MNRAS, 277, 781

Ibata, R. A., & Razoumov, A. O. 1998, A&A, 336, 130

Ibata, R., Irwin, M., Bienaymé, O., et al. 2000, ApJ, 532, L41

Ibata, R. A., Irwin, M. J., Lewis, G. F., et al. 2003, MNRAS, 340, L21

Ibata, R., Lewis, G. F., Martin, N. F., et al. 2013, ApJ, 765, L15

Ibata, R. A., Malhan, K., & Martin, N. F. 2019, ApJ, 872, 152

Ibata, R. A., Bellazzini, M., Malhan, K., et al. 2019, Nature Astronomy, 3, 667

Innanen, K. A., & House, F. C. 1970, AJ, 75, 680

Iorio, G., Nipoti, C., Battaglia, G., et al. 2019, MNRAS, 487, 5692

Ishigaki, M. N., Chiba, M., & Aoki, W. 2012, ApJ, 753, 64

Ishigaki, M. N., Aoki, W., & Chiba, M. 2013, ApJ, 771, 67

Ivezić, Ž., Goldston, J., Finlator, K., et al. 2000, AJ, 120, 963

Ivezić, Ž., Kahn, S. M., Tyson, J. A., et al. 2019, ApJ, 873, 111

Jackson-Jones, R., Jofré, P., Hawkins, K., et al. 2014, A&A, 571L, 5

Johnson, D. R. H., & Soderblom, D. R. 1987, AJ, 93, 864

Johnston, K. V. 1998, ApJ, 495, 297

Johnston, K. V., Zhao, H. S., Spergel, D. N., et al. 1999, Working on the Fringe: Optical and IR Interferometry from Ground and Space, 15

Johnston, K. V., Majewski, S. R., Siegel, M. H., et al. 1999, AJ, 118, 1719

Johnston, K. V., Law, D. R., & Majewski, S. R. 2005, ApJ, 619, 800

Johnston, K. V. 2016, The General Assembly of Galaxy Halos: Structure, Origin and Evolution, 317, 1

Jönsson, H., Allende Prieto, C., Holtzman, J. A., et al. 2018, AJ, 156, 126

Jönsson, H., et al., in preparation

Kallivayalil, N., van der Marel, R. P., Besla, G., et al. 2013, ApJ, 764, 161

Kallivayalil, N., Sales, L. V., Zivick, P., et al. 2018, ApJ, 867, 19

Karakas, A. I., & Lattanzio, J. C. 2014, PASA, 31, e030

Kawata, D., Bovy, J., Matsunaga, N., & Baba, J. 2019, MNRAS, 482, 40

Kazantzidis, S., Bullock, J. S., Zentner, A. R., et al. 2008, ApJ, 688, 254

Keller, S. C., Yong, D., & Da Costa, G. S. 2010, ApJ, 720, 940

Kinman, T. D., Suntzeff, N. B., & Kraft, R. P. 1994, AJ, 108, 1722

Koposov, S. E., Rix, H.-W., & Hogg, D. W. 2010, ApJ, 712, 260

Koposov, S. E., Belokurov, V., Evans, N. W., et al. 2012, ApJ, 750, 80

Koposov, S. E., Belokurov, V., & Evans, N. W. 2013, ApJ, 766, 79

Koposov, S. E., Belokurov, V., Li, T. S., et al. 2019, MNRAS, 485, 4726

Kruijssen, J. M. D., Pfeffer, J. L., Reina-Campos, M., et al. 2019, MNRAS, 486, 3180

Kunkel, W. E., & Demers, S. 1976, The Galaxy and the Local Group, 241

Kunkel, W. E. 1979, ApJ, 228, 718

Kurucz, R. L. 1979, ApJS, 40, 1

Laporte, C. F. P., Johnston, K. V., Gómez, F. A., et al. 2018, MNRAS, 481, 286

Laporte, C. F. P., Minchev, I., Johnston, K. V., et al. 2019, MNRAS, 485, 3134

Law, D. R., Johnston, K. V., & Majewski, S. R. 2005, ApJ, 619, 807

Law, D. R., Majewski, S. R., & Johnston, K. V. 2009, ApJ, 703, L67

Law, D. R., & Majewski, S. R. 2010, ApJ, 714, 229

Law, D. R., & Majewski, S. R. 2010, ApJ, 718, 1128.

Law, D. R., & Majewski, S. R. 2016, Tidal Streams in the Local Group and Beyond, 420, 31

Leaman, R., VandenBerg, D. A., & Mendel, J. T. 2013, MNRAS, 436, 122

Lee, Y. S., Beers, T. C., An, D., et al. 2011, ApJ, 738, 187

Lee, D. M., Johnston, K. V., Sen, B., & Jessop, W. 2015, ApJ, 802, 48

Lemasle, B., de Boer, T. J. L., Hill, V., et al. 2014, A&A, 572, 82

Letarte, B., Hill, V., Tolstoy, E., et al. 2010, A&A, 523, A17

Li, T. S., Sheffield, A. A., Johnston, K. V., et al. 2017, ApJ, 844, 74

Lindegren, L., & Feltzing, S. 2013, A&A, 553, A94

Liu, Z.-W., & Stancliffe, R. J. 2018, MNRAS, 475, 5257

Łokas, E. L., Kazantzidis, S., Majewski, S. R., et al. 2010, ApJ, 725, 1516

Łokas, E. L., Kazantzidis, S., Majewski, S. R., et al. 2012, Astrophysics and Space Science Proceedings, 28, 113

Lopez-Corredoira, M., Allende Prieto, C., Garzon, F., et al. 2018, A&A, 612, L8

Luri, X., Brown, A. G. A., Sarro, L. M., et al. 2018, A&A, 616, A9

Lutz, T. E., & Kelker, D. H. 1973, PASP, 85, 573

Lynden-Bell, D. 1982, The Observatory, 102, 202

Mackereth, J. T., Crain, R. A., Schiavon, R. P., et al. 2018, MNRAS, 477, 5072

Mackereth, J. T., Bovy, J., Leung, H. W., et al. 2019, MNRAS, 489, 176

Mackereth, J. T., Schiavon, R. P., Pfeffer, J., et al. 2019, MNRAS, 482, 3426

MacQueen, J. 1967, in Proc. Fifth Berkeley Symp. on Math. Statist. and Prob., Volume 1: Statistics (Berkeley, CA: Univ. of Calif. Press), 281

Majewski, S. R. 1992, ApJS, 78, 87

Majewski, S. R. 1993, ARA&A, 31, 575

Majewski, S. R. 1993, Galaxy Evolution. The Milky Way Perspective, 5

Majewski, S. R. 1994, ApJ, 431, L17

Majewski, S. R., Munn, J. A., & Hawley, S. L. 1994, ApJ, 427, L37

Majewski, S. R., Munn, J. A., & Hawley, S. L. 1996, ApJ, 459, L73

Majewski, S. R., Patterson, R. J., Palma, C., et al. 2002, Modes of Star Formation and the Origin of Field Populations, 199

Majewski, S. R., Skrutskie, M. F., Weinberg, M. D., & Ostheimer, J. C. 2003, ApJ, 599, 1082

Majewski, S. R., Ostheimer, J. C., Rocha-Pinto, H. J., et al. 2004, ApJ, 615, 738

Majewski, S. R., Kunkel, W. E., Law, D. R., et al. 2004, AJ, 128, 245

Majewski, S. R., Law, D. R., Polak, A. A., & Patterson, R. J. 2006, ApJ, 637, L25

Majewski, S. R., Nidever, D. L., Smith, V. V., et al. 2012, ApJL, 747, L37

Majewski, S. R., Hasselquist, S., Łokas, E. L., et al. 2013, ApJ, 777, L13

Majewski, S. R., Schiavon, R. P., Frinchaboy, P. M., et al. 2017, AJ, 154, 94

Malhan, K., & Ibata, R. A. 2017, MNRAS, 471, 1005

Malhan, K., & Ibata, R. A. 2019, MNRAS, 486, 2995

Malhan, K., Ibata, R. A., Carlberg, R. G., et al. 2019, ApJ, 886, L7

Maoz, D. 2010, American Institute of Physics Conference Series, 223

Maoz, D., Mannucci, F., & Brandt, T. D. 2012, MNRAS, 426, 3282

Martig, M., Fouesneau, M., Rix, H.-W., et al. 2016, MNRAS, 456, 3655

Martin, N. F., Ibata, R. A., & Irwin, M. 2007, ApJ, 668, L123

Martínez-Delgado, D., Aparicio, A., Gómez-Flechoso, M. Á., et al. 2001, ApJ, 549, L199

Martínez-Delgado, D., Gómez-Flechoso, M. Á., Aparicio, A., et al. 2004, ApJ, 601, 242.

Mateo, M., Olszewski, E. W., & Morrison, H. L. 1998, ApJ, 508, L55

McDonald, I., Zijlstra, A. A., Sloan, G. C., et al. 2013, MNRAS, 436, 413.

Meng, X., & Yang, W. 2012, A&A, 543, A137

Minchev, I., Famaey, B., Quillen, A. C., et al. 2012, A&A, 548, A127

Monaco, L., Bellazzini, M., Ferraro, F. R., et al. 2004, MNRAS, 353, 874.

Monaco, L., Bellazzini, M., Bonifacio, P., et al. 2005, A&A, 441, 141.

Monaco, L., Bellazzini, M., Bonifacio, P., et al. 2007, A&A, 464, 201

Morrison, H. L. 1993, AJ, 105, 539

Mucciarelli, A., Bellazzini, M., Ibata, R., et al. 2017, A&A, 605, A46

Muñoz, R. R., Majewski, S. R., Zaggia, S., et al. 2006, ApJ, 649, 201.

Myeong, G. C., Evans, N. W., Belokurov, V., et al. 2018, MNRAS, 478, 5449

Myeong, G. C., Vasiliev, E., Iorio, G., et al. 2019, MNRAS, 488, 1235

Navarro, J. F., Abadi, M. G., Venn, K. A., et al. 2011, MNRAS, 412, 1203

Newberg, H. J., Yanny, B., Rockosi, C., et al. 2002, ApJ, 569, 245

Newberg, H. J., & Xu, Y. 2017, Formation and Evolution of Galaxy Outskirts, 13

Nidever, D. L., Bovy, J., Bird, J. C., et al. 2014, ApJ, 796, 38

Nidever, D. L., Holtzman, J. A., Allende Prieto, C., et al. 2015, AJ, 150, 173

Niederste-Ostholt, M., Belokurov, V., & Evans, N. W. 2012, MNRAS, 422, 207

Nissen, P. E. & Schuster, W. J. 1997, A&A, 326, 751

Nissen, P. E. & Schuster, W. J. 2010, A&A, 511L, 10

Nissen, P. E. & Schuster, W. J. 2011, A&A, 530A, 15

Nomoto, K., Kobayashi, C., & Tominaga, N. 2013, ARA&A, 51, 457

Norris, J. E. 1994, ApJ, 431, 645

Odenkirchen, M., Grebel, E. K., Rockosi, C. M., et al. 2001, ApJ, 548, L165

Pardy, S. A., D'Onghia, E., Navarro, J. F., et al. 2020, MNRAS, 492, 1543

Peñarrubia, J., Martínez-Delgado, D., Rix, H. W., et al. 2005, ApJ, 626, 128

Peñarrubia, J., Belokurov, V., Evans, N. W., et al. 2010, MNRAS, 408, L26

Peñarrubia, J., Zucker, D. B., Irwin, M. J., et al. 2011, ApJ, 727, L2

Plummer, H. C. 1911, MNRAS, 71, 460

Price-Whelan, A. M., Johnston, K. V., Sheffield, A. A., Laporte, C. F. P., & Sesar, B. 2015, MNRAS, 452, 676

Price-Whelan, A. M., & Bonaca, A. 2018, ApJ, 863, L20

Price-Whelan, A. M., Mateu, C., Iorio, G., et al. 2019, AJ, 158, 223

Purcell, C. W., Bullock, J. S., Tollerud, E. J., et al. 2011, Nature, 477, 301

Queiroz, A. B. A., Anders, F., Santiago, B. X., et al. 2018, MNRAS, 476, 2556

Queiroz, A. B. A., Anders, F., Chiappini, C., et al. 2019, MNRAS, submitted, arXiv:1912.09778

Quinn, P. J., Hernquist, L., & Fullagar, D. P. 1993, ApJ, 403, 74

Ramírez, I., Meléndez, J., & Chanamé, J., 2012, ApJ, 757, 164

Recio-Blanco, A., Rojas-Arriagada, A., de Laverny, P., et al. 2017, A&A, 602, L14

Reddy, B. E., Tomkin, J., Lambert, D. L., et al. 2003, MNRAS, 340, 304

Reddy, B. E., Lambert, D. L., & Allende Prieto, C. 2006, MNRAS, 367, 1329

Reid, M. J., & Brunthaler, A. 2004, ApJ, 616, 872

Reid, M. J., Menten, K. M., Zheng, X. W., et al. 2009, ApJ, 700, 137

Rocha-Pinto, H. J., Majewski, S. R., Skrutskie, M. F., et al. 2003, ApJ, 594, L115

Rocha-Pinto, H. J., Majewski, S. R., Skrutskie, M. F., Crane, J. D., & Patterson, R. J. 2004, ApJ, 615, 732

Roderick, T. A., Jerjen, H., Mackey, A. D., et al. 2015, ApJ, 804, 134

Roderick, T. A., Mackey, A. D., Jerjen, H., et al. 2016, MNRAS, 461, 3702

Rousseeuw, P. J. 1987, Journal of Computational and Applied Mathematics, 20, 53

Ruchti, G. R., Fulbright, J. P., Wyse, R. F. G., et al. 2011, ApJ, 737, 9

Sales, L. V., Helmi, A., & Battaglia, G. 2010, Advances in Astronomy, 2010, 194345

Sales Silva, J. V., Perottoni, H. D., Cunha, K., et al. 2019, ApJ, 886, 113

Sanders, J. L., & Das, P. 2018, MNRAS, 481, 4093

Santana, F. A., et al. in preparation

Santiago, B. X., Brauer, D. E., Anders, F., et al. 2016, A&A, 585, A42

Sbordone, L., Bonifacio, P., Buonanno, R., et al. 2007, A&A, 465, 815

Schönrich, R., Binney, J., & Dehnen, W. 2010, MNRAS, 403, 1829

Schönrich, R., Asplund, M., & Casagrande, L. 2011, MNRAS, 415, 3807

Schönrich, R. 2012, MNRAS, 427, 274

Schönrich, R., Asplund, M., & Casagrande, L. 2014, ApJ, 786, 7

Schuster, W. J. & Nissen, P. E. 1988, A&AS, 73, 225

Schuster, W. J., Parrao, L., & Contreras Martínez, M. E. 1993, A&AS, 97, 951

Schuster, W. J., Moreno, E., Nissen, P. E., Pichardo, B. 2012, A&A, 538, 21

Searle, L., & Zinn, R. 1978, ApJ, 225, 357

Sellwood, J. A., & Binney, J. J. 2002, MNRAS, 336, 785

Sesar, B., Hernitschek, N., Dierickx, M. I. P., et al. 2017, ApJ, 844, L4.

Sesar, B., Ivezić, Ž., Grammer, S. H., et al. 2010, ApJ, 708, 717

Sharma, S., Johnston, K. V., Majewski, S. R., et al. 2010, ApJ, 722, 750

Sheffield, A. A., Majewski, S. R., Johnston, K. V., et al. 2012, ApJ, 761, 161

Sheffield, A. A., Johnston, K. V., Majewski, S. R., et al. 2014, ApJ, 793, 62

Sheffield, A. A., Price-Whelan, A. M., Tzanidakis, A., et al. 2018, ApJ, 854, 47

Shetrone, M. D., Côté, P., & Sargent, W. L. W. 2001, ApJ, 548, 592

Shetrone, M. D., Venn, K. A., Tolstoy, E., et al. 2003, AJ, 125, 684

Shetrone, M., Bizyaev, D., Lawler, J. E., et al. 2015, ApJS, 221, 24

Shi, W. B., Chen, Y. Q., Carrell, K., & Zhao, G. 2012, ApJ, 751, 130

Shipp, N., Drlica-Wagner, A., Balbinot, E., et al. 2018, ApJ, 862, 114

Siegel, M. H., Dotter, A., Majewski, S. R., et al. 2007, ApJ, 667, L57

Skrutskie, M. F., Cutri, R. M., Stiening, R., et al. 2006, AJ, 131, 1163

Smith, V. V., et al., in preparation

Sohn, S. T., Majewski, S. R., Muñoz, R. R., et al. 2007, ApJ, 663, 960

Sollima, A., Valls-Gabaud, D., Martinez-Delgado, D., et al. 2011, ApJ, 730, L6

Sommer-Larsen, J., & Zhen, C. 1990, MNRAS, 242, 10

Souto, D., Cunha, K., Smith, V., et al. 2016, ApJ, 830, 35

Spitoni, E., Silva Aguirre, V., Matteucci, F., et al. 2019, A&A, 623, A60

Taylor, M. B. 2005, Astronomical Data Analysis Software and Systems XIV, 347, 29

Tepper-García, T., & Bland-Hawthorn, J. 2018, MNRAS, 478, 5263

Tissera, P. B., White, S. D. M., & Scannapieco, C. 2012, MNRAS, 420, 255

Tissera, P. B., Scannapieco, C., Beers, T. C., & Carollo, D. 2013, MNRAS, 432, 3391

Tolstoy, E., Irwin, M. J., Helmi, A., et al. 2004, ApJ, 617, L119.

Tolstoy, E., Hill, V., & Tosi, M. 2009, ARA&A, 47, 371

Toth, G., & Ostriker, J. P. 1992, ApJ, 389, 5

Tsujimoto, T., Nomoto, K., Yoshii, Y., et al. 1995, MNRAS, 277, 945

Unavane, M., Wyse, R. F. G., & Gilmore, G. 1996, MNRAS, 278, 727

van der Marel, R. P., Fardal, M. A., Sohn, S. T., et al. 2019, ApJ, 872, 24

Van der Swaelmen, M., Hill, V., Primas, F., Cole, A. A. 2013, A&A, 560, 44

VandenBerg, D. A., Brogaard, K., Leaman, R., & Casagrande, L. 2013, ApJ, 775, 134

Venn, K. A., Irwin, M., Shetrone, M. D., et al. 2004, AJ, 128, 1177

Vera-Ciro, C., D'Onghia, E., Navarro, J., & Abadi, M. 2014, ApJ, 794, 173

Vera-Ciro, C., & Helmi, A. 2013, ApJ, 773, L4

Vincenzo, F., Spitoni, E., Calura, F., et al. 2019, MNRAS, 487, L47

Vivas, A. K., Zinn, R., Andrews, P., et al. 2001, ApJ, 554, L33

Wagner-Kaiser, R., Sarajedini, A., von Hippel, T., et al. 2017, MNRAS, 468, 1038

Walcher, C. J., Yates, R. M., Minchev, I., et al. 2016, A&A, 594, A61

Walker, I. R., Mihos, J. C., & Hernquist, L. 1996, ApJ, 460, 121

Wang, J., Shi, J., Pan, K., et al. 2016, MNRAS, 460, 3179

Weinberg, D. H., Holtzman, J. A., Hasselquist, S., et al. 2019, ApJ, 874, 102

Wilson, J. C., Hearty, F. R., Skrutskie, M. F., et al. 2019, PASP, 131, 055001

Wyse, R. F. G., & Gilmore, G. 1993, The Globular Cluster-galaxy Connection, 727

Wyse, R. F. G. 2016, Multi-object Spectroscopy in the Next Decade: Big Questions, Large Surveys, and Wide Fields, 13

Xu, Y., Newberg, H. J., Carlin, J. L., et al. 2015, ApJ, 801, 105

Yang, C., Xue, X.-X., Li, J., et al. 2019, ApJ, 886, 154

Yanny, B., Newberg, H. J., Grebel, E. K., et al. 2003, ApJ, 588, 824

Yanny, B., Newberg, H. J., Johnson, J. A., et al. 2009, ApJ, 700, 1282

Yoshii, Y. 1982, PASJ, 34, 365

Zamora, O., García-Hernández, D. A., Allende Prieto, C. et al. 2015, AJ, 149, 181

Zasowski, G., Johnson, J. A., Frinchaboy, P. M., et al. 2013, AJ, 146, 81

Zasowski, G., Cohen, R. E., Chojnowski, S. D., et al. 2017, AJ, 154, 198

Zhao, G., Zhao, Y.-H., Chu, Y.-Q., et al. 2012, Research in Astronomy and Astrophysics, 12, 723

Zinn, R. 1993, The Globular Cluster-Galaxy Connection, 48, 38

Zinn, R. 1996, Formation of the Galactic Halo...Inside and Out, 92, 211

Zivick, P., Kallivayalil, N., Besla, G., et al. 2019, ApJ, 874, 78